

LIGHTNING IN PROTOPLANETARY DISKS

*Takayuki Muranushi*¹

The Hakubi Center, Kyoto University, Japan;
Yukawa Institute for Theoretical Physics, Kyoto University,
Sakyo-ku, Kyoto, 606-8502, Japan

*A Dissertation
Submitted to The Department of Physics, Kyoto University
in Partial Fulfillment of the Requirements
for the Degree of
Doctor of Phylosophy*

¹E-mail address: nushio@yukawa.kyoto-u.ac.jp, muranushi@gmail.com

Dedication

To The Concept of Hope

Abstract

The electromagnetic processes play critical roles in the protoplanetary disks and planetary systems formation. This thesis aims to model lightning in protoplanetary disks to utilize it as a probe for such electromagnetic processes.

Protoplanetary disks are hosts of varieties of non-equilibrium dynamic processes. Their ultimate source of the power is their gravitational potential energy. Magnetorotational instability (MRI) is considered to be the dominant mechanism of angular momentum transport. MRI also converts gravitational potential energy to magnetohydrodynamic turbulent energy. The turbulence governs, apart from many other processes, dust collision, leading both to growth and destruction of dust aggregates. The dust is the host of chemical reactions and plasma recombination. Both the number density and the shape of each aggregate must be taken into account to determine the plasma ionization degree, which in turn, switches the MRI. Being weakly ionized, the dust-rich plasma of protoplanetary disk is susceptible to various forms of electric insulation breakdown phenomena. In particular, lightning in the protoplanetary disks has been focused on for decades, as a candidate for the chondrule heating mechanism.

In this thesis, I first calculate the charge distribution within the dust-plasma system located in the protoplanetary disk, with collisional charging taken into account. Two previously unknown phases of dust-plasma emerge as the number density of the dust increases. Under such phases the dust-dust collision is the dominant source of charge separation, and electric breakdown condition can be met at dust number density much smaller than previously assumed. I calculate the breakdown condition for millions of different dust parameters, and also derive an approximation formula for the breakdown condition.

Second, I introduce the effect of electrostatic discharge into magnetohydrodynamic equations as a nonlinear form of Ohmic resistivity. I perform three-dimensional simulations of protoplanetary disk segments, and confirm the existence of magnetorotational instability(MRI) under the conditions previously thought to be MRI inactive. Under such circumstances the ionization required to support the MRI is provided by the electrostatic discharge caused by MRI itself. Major portion of the accretion energy can be converted to Joule heat through the nonlinear part of the Ohmic resistivity in such regions.

Finally, I perform two-dimensional simulations of dust sedimentation in differentially rotating protoplanetary disk which is unstable against Kelvin-Helmholtz instability. The simulations successfully reproduced the morphological feature of lightning.

No observation of lightning in extrasolar systems has been reported to date. However, ever since the discovery of 51 Peg b the first extrasolar planet and the first hot Jupiter, the observations of of extrasolar planets and protoplanetary disks are in progress, and the theory of protoplanetary disks and planet system formations are under progress. Observational verifications of lightning models proposed in this thesis will be a unique progress in understanding the planetary formation theory.

Contents

1	Introduction	4
1.1	Introduction	4
1.2	Standard Models of Protoplanetary Disks	4
1.3	Problems of Planet Formation Theory	8
1.4	Electromagnetic Processes in Protoplanetary Disks	9
2	Collisional Charging and Lightning	12
2.1	Dust Charging Processes	12
2.1.1	Earlier Studies on Disk Lightning	12
2.1.2	Dust Charging By Plasma Absorption	16
2.1.3	Dust Charge due to Collision of Ice Dust	17
2.2	Dust Changing Model	18
2.2.1	The Disk Model	18
2.2.2	Charge Exchange Equations	20
2.2.3	Fluffy Dust Model	22
2.2.4	Collisional Cross Section and Contact Surface of Charged Fluffy Dust	23
2.2.5	Charge Separation Processes	25
2.2.6	Relative Velocity	27
2.2.7	The Charge Equilibrium Equations	27
2.2.8	Four Phases of Charge Separation	29
2.3	Lightning due to Dust Charge	35
2.3.1	Critical Dust Number Density for Lightning	35
2.3.2	Numerical Simulations for Uniform-box Lightning Estimation	36
2.3.3	Analytic Formulae for Lightning Conditions	37
3	Self Sustained MRI	48
3.1	Magnetorotational Instability with nonlinear Ohm's law	48
3.1.1	Physical Motivation	48
3.1.2	Numerical Setup	49
3.1.3	Simulations Procedure	53
3.1.4	The Result of Shearing-Box Simulations	54
3.1.5	Interpretation of The Simulation Results	56
3.2	Distribution of The Three MRI Zones within The Protoplanetary Disks	63
3.2.1	Protoplanetary Disk Model	63
3.2.2	Ionization Processes	64

3.2.3	The Self-Sustained MRI in Global Disk Models	66
3.3	Conclusions and Discussions	70
4	Lightning Morphology and Observations	74
4.1	Multi-dimensional Simulations of Disk Lightning Propagation	74
4.1.1	The Two-dimensional Model for Disk Lightning	74
4.1.2	The Simulation Result	77
4.2	Implication for Observations	77
4.2.1	Energetics and Direct Observations	77
4.2.2	Implication on Chondrule Formations	82
5	Summary and Future Prospect	84
5.1	Summary	84
5.2	Future Prospect	85

Chapter 1

Introduction

1.1 Introduction

Blinding flashes and deafening thunders — lightning is one of the most outstanding natural phenomena. Human beings recognized the phenomena from the ancient ages, and in many cultures it has been considered as manifestation of God's power or will. The perspective has been handed down to the contemporary culture of the age of science (Figure 1.1), based on the people's interest and awe in the phenomena.

Lightning has been observed on solar system planets. Venus (Russell et al., 2007; Svedhem et al., 2007), Earth, Mars (Ruf et al., 2009), Jupiter (Borucki & Magalhaes, 1992; Little et al., 1999) and Saturn (Gurnett et al., 2005; Fischer et al., 2006) have been confirmed as sites of lightning. Lightning models are also proposed for Saturn's satellite Titan (Desch & Kaiser, 1990; Tokano et al., 2001) and for extrasolar planets (Helling, 2011; Helling et al., 2011). This thesis deals with another possible host of astronomical lightning — protoplanetary disks.

Because the current understanding of the planet formation theory has several problems, microscopic features of dust component in protoplanetary disks have been attracting more scientific interests. Features such as dust fluffiness and compositions are receiving more attention than before as part of the crucial factors in protoplanetary disk models. The effect of electric charge of the dust aggregates is one of such factors. Such global motion of charged dust aggregates taken into account, I predict that the generated electrostatic field is large enough to cause lightning. The critical amplitude of the electrostatic field can also be reached as a consequence of resistive magnetohydrodynamic turbulence.

I will first introduce a standard theory of planet formation, which takes place in a protoplanetary disks. Then I will present arguments on current understandings and problems of planet formation theory.

1.2 Standard Models of Protoplanetary Disks

Our galaxy consists of astronomical bodies such as stars and planets and compact objects, and the space between them are filled with the interstellar medium. It has been recognized that the interstellar medium is where the star and planet formation process initiates. The



Figure 1.1. “*A sign from God? Lightning strikes the basilica of St.Peter’s dome earlier this evening during a storm that struck Rome on the same day Pope Benedict XVI announced his resignation.*” Article by Simon Tomlinson and Richard Hartley-parkinson, photo by Filippo Monteforte, ©Associated Newspapers Ltd. <http://www.dailymail.co.uk/news/article-2276884>

most popular element of the gas is hydrogen. Their averaged number density is smaller than 1 cm^{-3} . Less than 1% in volume, but about half the mass of the interstellar gas, are contained in clouds of molecular hydrogen H₂. Protoplanetary disks form from such molecular clouds.

Various molecules and minerals in form of tiny solid particles are also observed in the interstellar medium. The typical radius of the solid particles is $0.1 \mu\text{m}$. They are termed “dust” in astrophysical context. The term applies to any *small* solid particle in astronomical sense; thus even asteroids of km-sizes are referred to as “km-sized dust.” In the early literatures of planetary formation theory it had been common to assume that all the dust particles are spherical bodies of the material density. However, such dense dust models do not fit in with the reality. When two pieces of elemental dust collide, they silently stick together, and form a fluffy, very low-density structure, because the self gravitational interaction for such bodies are negligibly small. The fluffy dust structure resembles that of a house dust, or a piece of powder snow. A typical dust aggregate with 1 m radius is lighter than the same volume of 1 atmosphere pressure air. In a protoplanetary disk, such dust, starting from $0.1 \mu\text{m}$ in radius stick together, and takes millions of years to finally become

thousands of kilometers in radii — those, are called planets, on one of which we dwell.

The study on the origin of the solar system started in the 1960's, independently by Japanese, U.S. and Russian group, respectively led by Hayashi, Cameron, and Safronov. Hayashi et al. (1985)'s work is still remembered today as "the standard scenario of planet formation." cf. Figure 1.2. Since then, theoretical problems have been found for some parts of the scenario, and observational results are incoming that are beyond the imagination of the scenario. I introduce such problems in §1.3. Such updates have been patchy and no astrophysicist has succeeded in combining those new results into new, self-consistent scenario. Hence I introduce the standard scenario, whose significance as a theoretical backbone stays adamant.

- **Stage 1.** Protostar and protoplanetary disk formation.

The densest part ($\sim 10^6 \text{ cm}^{-3}$) of a molecular cloud further cools and contract by its self-gravity, and becomes a protostar which initially is of the order of one Jupiter mass. The remainder of the gas ($1 \sim 100 M_\odot$; M_\odot is a solar mass) cannot fall immediately to the star because of its initial angular momentum. Thus it forms a rotating disk-shaped object around the protostar. This is the progenitor of a protoplanetary disk.

- **Stage 2.** Protostar growth.

The disk generates density waves due to its self-gravity. The waves transport the angular momentum outside, and then the disk material accretes towards the protostar. The star shines due to the released gravitational potential energy, and spews out stellar wind. The wind limits the accretion at some point and fixes the stellar mass. The disk mass decreases gradually, and when it is about $0.01 M_\odot$, planet formation starts.

- **Stage 3.** Dust sedimentation and formation of the protoplanets.

As the disk loses its mass by accretion, it becomes less turbulent. Consequently, dust particles can stick together and form aggregates. The grown dust sediments to disk equatorial plane. When enough dust is gathered on the equatorial plane, the dust swarm collapses by its self-gravity to form km-sized protoplanets.

- **Stage 4.** Protoplanet growth through collision

Protoplanets collide and merge together. The growth is oligarchic (Kokubo & Ida, 1998): larger planetesimals can gather more material and grow faster. Thus in the end dozens of grown-up planetesimals are formed. Their mass was $0.1 M_\oplus$ around the earth orbit and $2 M_\oplus$ around the Jupiter orbit (M_\oplus : an Earth mass.)

- **Stage 5.** Gas giant formation and the end of the disk

Heavy planets formed among the Jupiter and Saturn orbit accrete protoplanetary disk gas until they deplete the gas around their orbit and open gaps in the disk. Thus they become gas giant planets. Lighter planets which are formed around the inner orbits are not large enough to cause gas capture. After a few final giant impacts they become rocky planets like Mercury, Venus, Earth, Mars. Eventually the disk gas disappears and a planetary system is formed. At outer orbits where the material

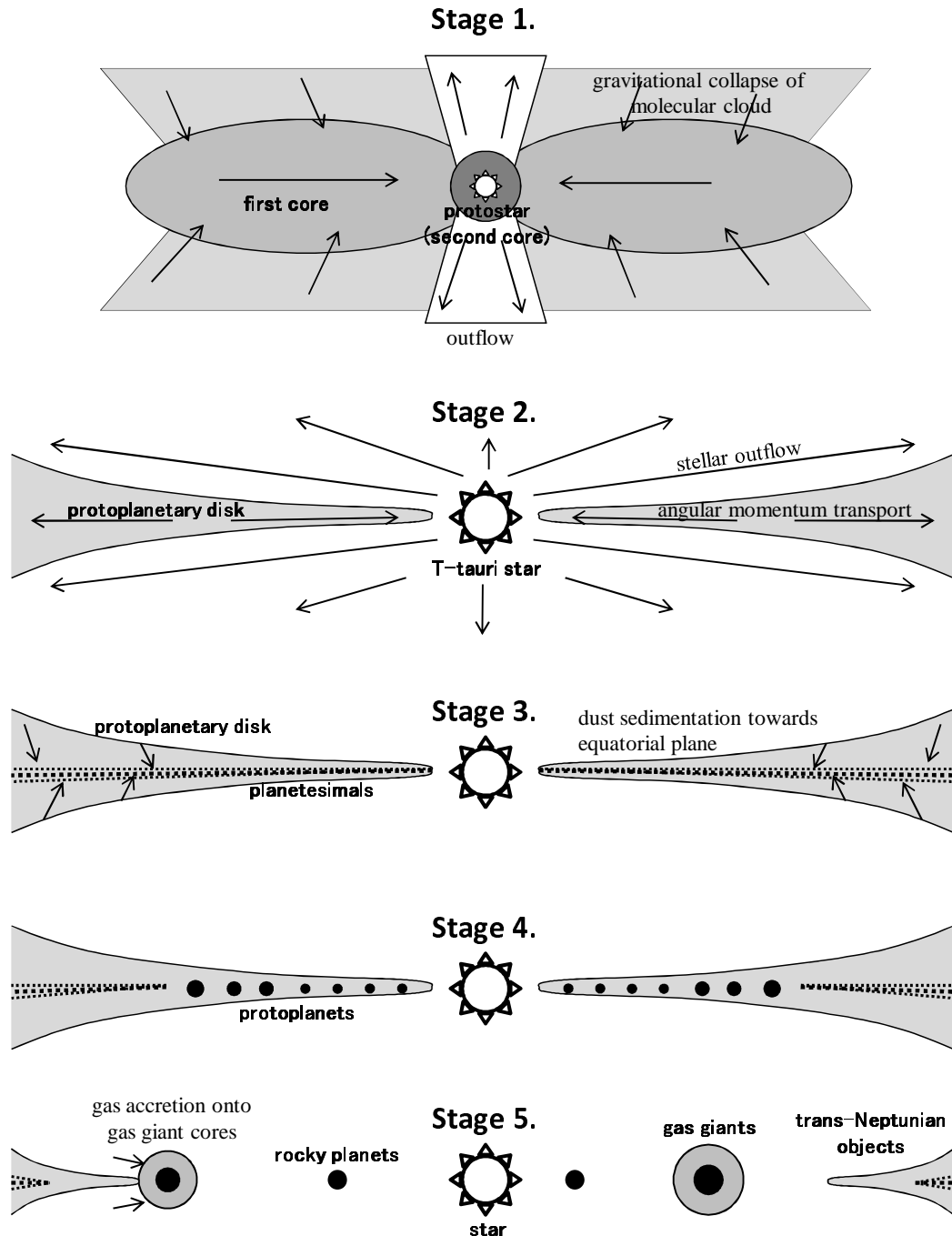


Figure 1.2. The standard scenario of planet formation.

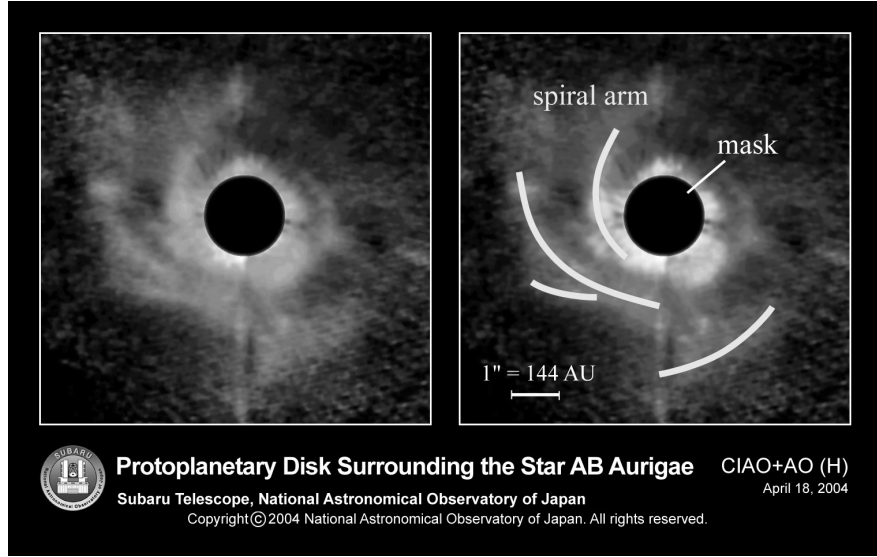


Figure 1.3. Picture of a protoplanetary disk, taken by Subaru telescope. Original images can be obtained from <http://subarutelescope.org/Pressrelease/2004/04/18/index.html>.

dispersion timescale is shorter than the core-growth timescale, rocky cores are not possible to fully accrete gas, leading to gas giants like Uranus and Neptune which are smaller than Jupiter and Saturn. At even outer orbits, unused planetesimals remain for billions of years, as Kuiper belt and Oort cloud bodies.

1.3 Problems of Planet Formation Theory

This standard scenario has been developed as a result of elaborate work, and used as a foundation of today's planet formation theory. However, later on, several problems are found on the standard scenario.

To understand the mechanisms, it helps to be noted that dust(solid) and gas component has different orbital velocity. The orbital velocity of a point mass around a star is determined by the balance between the gravitational force from the central star and the centrifugal force from the orbital rotation. The velocity is called Kepler velocity. The gas component has the sub-Keplarian orbital velocity because the pressure gradient (the closer to the central star, the higher is the pressure) assists the centrifugal force. The solid components are not affected by the pressure gradient and tend to orbit in Keplerian velocity. The heaviest bodies ($r > 1 \text{ km}$) do maintain their Keplerian velocity and due to their inertia their orbit is unaffected by the gas. By contrast, the lighter planetesimals ($1 \text{ cm} < r < 1 \text{ m}$) give their angular momentum to the slowly-rotating gas via gas friction, and tend to fall into the star. The even lighter, or lower density dust aggregates, are coupled to the gas motion via friction and do not fall.

When one take such gas-dust interaction into account and try to predict the fate of planetesimals, the following problems in planet formation theory arise.

- Prohibition of protoplanet formation by Kelvin-Helmholtz instability.

As the dust sediment at the disk equatorial plane (Stage 3), the relative velocity between the equatorial dust layer and high-altitude gas layer becomes greater. The difference in the velocity causes a Kelvin-Helmholtz instability which will disturb the dust-sedimented layer. Thus dust layer cannot reach the dust density enough to cause self-gravity-driven planetesimal formation.

- Loss of cm-sized dust by migration.

There is an alternative scenario for planetesimal growth (Stage 3): planetesimals can gradually grow by mutual sticking. In this case, when the size of the planetesimals reaches ~ 1 cm, the planetesimals start to migrate towards the central star more rapidly than their growth timescale, which prevents the further growth.

- Loss of earth-sized protoplanet by type-I migration.

Even if the planetesimals manage to grow to be larger than 1 km in size, when they reach the earth radius (Stage 4), they will raise spiral-arm structures in the protoplanetary disk. The arms transfer the angular momentum from the planets to the disk; this cause the young planets to fall into the star before the protoplanetary disk disappears.

- Suggestion from observations.

Direct images of extra-solar planets have been observed (Kalas et al., 2008; Marois et al., 2008; Lagrange et al., 2009; Thalmann et al., 2009) in the latest few years. However, those directly-imaged gas-giant planets are located at orbital radii of hundreds of astronomical units (au), while the standard model predicts such planets to be in orbit $2 \sim 20$ au. Also, direct images of protoplanetary disks that extend to hundreds of au are available now (e.g. Figure 1.3.) These images, enabled by progresses in observation techniques, are indispensable information on planet formation theories. Since some of them are totally unexpected and intriguing, astrophysicists are now forced to reconstruct, or, enrich their theory on planet formation.

One of the assumptions of the standard scenario is that planets are formed at the orbital radii they are found today; in this sense it is a stationary model. Observations mentioned above cast questions to this assumption. Planets may have formed in wider area, compared to today's solar system, and dynamism in protoplanetary disk brought them to where they are today. Dynamism of the disk is exciting topic of study today, to which electromagnetic processes, along with hydrodynamic and gravitational processes contribute.

1.4 Electromagnetic Processes in Protoplanetary Disks

Figure 1.4 depicts several elemental processes related to electricity or magnetism proposed to be working in protoplanetary disk.

thi

One of the well-known role of the dust in protoplanetary disk is to absorb charged plasma particles. The ionized degree of the disk is determined as equilibrium between the dust absorption and ionization processes. The main ionization sources are cosmic rays and

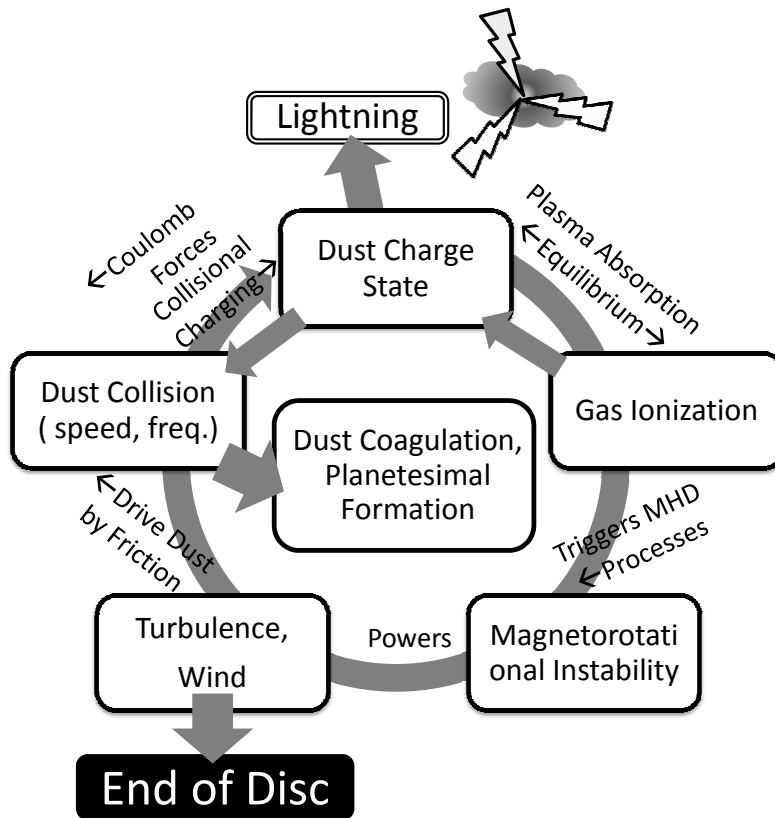


Figure 1.4. The cycle of electric and magnetic processes that affect each other. They are responsible for the fate of both the planets and the protoplanetary disk. Lightning (or, absence of it) is one of observational channels unique to electromagnetic processes.

the radioactive elements (Umebayashi & Nakano, 2009). Gas ionization is the factor that determines whether the gas motion is coupled or de-coupled to the magnetic field. This is most important because magnetorotational instability (MRI), a magnetohydrodynamic process gives the most promising explanation for disk turbulence (Balbus & Hawley, 1991, 1998). Predicted ionization degree in protoplanetary disk is too low to activate MRI for major part of the protoplanetary disk. (Gammie, 1996). When active, MRI drives the disk turbulence and wind. Turbulence causes relative motion among the dust aggregates because each aggregate responds differently according to its inertial mass or aerodynamic shape. Such relative motion causes dust aggregates to collide each other. Collisions can both contribute to the growth or the destruction of the dust. And collision also affects to dust charge state, through triboelectric charging or collisional charge separation.

The curved arrow at the top-left corner in Figure 1.4 represents the fact that the dust charge can actually affect the dust motion or even the global dynamics of the disk. This fact has not been taken into serious consideration until recently. The fact that dust-dust collisional charging is non-negligible closes the circle, and suggests that a comprehensive treatments are necessary for successful planet formation theory. It also suggests a unique means of observation: lightning. Although these electromagnetic processes surely will leave signals on well-established observational channels such as dust mass-distributions or disk spectrum-energy diagrams, it is difficult to distinguish electromagnetic processes from non-electromagnetic processes such as disk turbulence, radiative transport etc in such channels. If disk lightning does exist and is observable, we will have a separate channel that carries the information on undoubtedly electromagnetic processes.

The understanding of the electromagnetic nature of the protoplanetary disk is fundamental to update the “Standard Scenario,” and to answer the two most basic questions of planet formation theory: How did planets form? How and when did protoplanetary disk disappear? We know that there was a processes that put an end to protoplanetary disk, because it is not present at our solar system today. It could have accreted onto the sun, or lifted above the disk by disk-wind and then evaporated. We do not know how efficient the two processes were, but we are almost sure that both are driven by the magnetorotational instability. Also recently I have found that electrostatic charge of the dust aggregates will alter the initial stages of planet formation scenario. The next chapter will deal with this point.

Chapter 2

One-Zone Model of Collisional Charging and Lightning

2.1 Dust Charging Processes

2.1.1 Earlier Studies on Disk Lightning

Application of Earth lightning model in protoplanetary disk has been studied, especially as a candidate of chondrule heating mechanism. The other candidates include near-solar heating and nebular shock heating. Although the shock heating model is better understood and considered to be most likely, none of the model has acquired widespread acceptance (Desch & Connolly Jr, 2002).

Chondrules are spherical, silicate (silicon oxides) grains of mm size, found today in wide area of our solar system (Figure 2.1, right.) They are usually found included in chondrule-rich meteorites, called chondrites. Their round shape and their chemical composition suggest that they are formed from fluffy silicate dust aggregates when they are subject to 600–1200K heat, melted, become spherical by surface tension, then solidified again. The melting temperature of silicate is $10^1 \sim 10^2$ times higher than mean temperature of the disk regions considered. Also we know from the fraction of volatile materials in chondrules that the cooling timescale $5 - 3000 \text{ Kh}^{-1}$. Some transient heating source of such specific property must have existed universally in the protoplanetary phase of our solar system.

Lightning has been a candidate mechanisms for such transient heating, although compared to other models e.g. heating by shock wave (e.g. Miura et al., 2008), difficulties have been pointed out. Such difficulties can be summarized as three problems:

- **Neutralization Problem** (Gibbard et al., 1997).

Lightning due to ice-ice dust collision is not likely to take place. In protoplanetary disk because of plasma conductivity and few dust number density, the generated electric field E is too weak. You can improve E by increasing the dust number density

This chapter is based on the refereed journal article “*Dust–dust collisional charging and lightning in protoplanetary discs*” (Muranushi, 2010). Reproduced under the copyright assignment of the MNRAS.

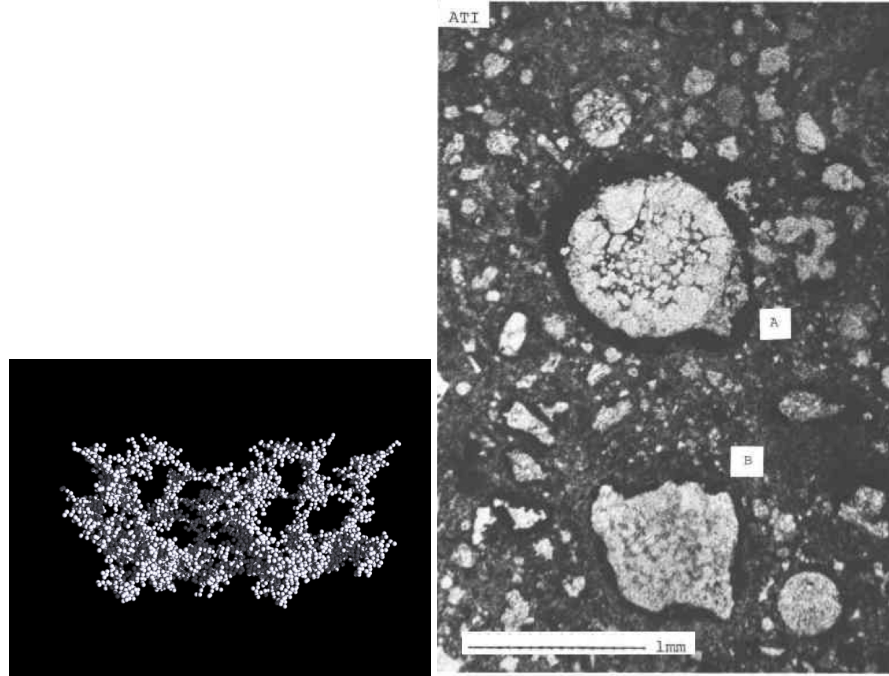


Figure 2.1. The dust aggregates, made of silicate or ice, in a protoplanetary disk has very low-density, fluffy structure when $r < 1$ m. This is because any compacting force (e.g. self-gravity) is too weak. (Left) A dust aggregate image from structural evolution simulation, by Wada et al. (2008). The monomer, the smallest unitary sphere in the image, is supposed to be $0.1 \mu\text{m}$ in diameter. (Right) An alpha-track image of a sliced chondrite by Shaw et al. (1988). A large chondrule is marked by [A], a mm-sized, dense, spherical structure. Such chondrules are evidences for transient heating and cooling events, where fluffy dust aggregates are melted, become droplets, and frozen again to form chondrules.

n . However $E \propto n^2$ so you need unnaturally high dust number density, according to the authors' estimate.

- **Energetics Problem** (e.g. Weidenschilling, 1997).

Even if lightning does take place, it is not energetic enough to melt the amount of chondrules observed today, because its energy budget is limited upto turbulent energy — a little portion of total kinetic energy.

- **Destruction Problem**(Güttler et al., 2008).

Even if lightning does take place, experiments show that it destroys the dust aggregates rather than melts them. Güttler et. al. synthesized the fluffy dust sample imitating the protoplanetary dust, placed the sample between two electrodes in a vacuum chamber, and exposed it to an electrical discharge. The dust samples generally fragmented leaving the major fraction thermally unprocessed.

particle					
gas			dust		
neutral gas	plasma				
neutral	ion	electron	smaller dust	larger dust	
			cationic	×	anionic

Table 2.1. The classification of particles I use in this chapter. ‘Particle’ is generic term for all components in the protoplanetary disks. Solid components are ‘dust,’ and the others are ‘gas.’ ‘Gas’ components are further subdivided into ‘neutral gas,’ and charged components, or ‘plasma.’ Finally, ‘plasma’ consists of ‘electron,’ the negative charge carrier, and various molecular ‘ion,’ the positive charge carrier. On the right side of the table, ‘dust’ is classified by their size as ‘smaller dust’ and ‘larger dust.’ Either can be ‘anionic’ or ‘cationic’ dust, depending on the material they consist of. I also use the one-letter symbols ‘g’, ‘e’, ‘i’, ‘S’, and ‘L’ for neutral gas, electron, ion, Smaller and Larger dust. The symbols for ‘Cationic’ and ‘Anionic’ dust are ‘C’ and ‘A’. I use variable \mathbf{I} to represent any of these symbols.

Despite of these oppositional theories, considerable number of studies conducted on protoplanetary disk over the past few decades motivate us to reconsider the possibility of the protoplanetary disk lightning. First, dust aggregates are not in material density — they take much lower-density, fluffy form as in Figure 2.1 (left), due to coagulation growth. This helps a lot in increasing dust-dust collision cross section in favor of lightning. Regions with dust number density higher than “standard scenario” are possible, due to snowline (e.g. Cuzzi & Zahnle, 2004), instability boundaries (e.g. Kato et al., 2010), or turbulence (e.g. Johansen et al., 2007). Both the increase in the cross section and the increase in the local number density of the dust affects positively to the dust-dust collision induced charge-up and lightning. The purpose of this chapter is to take these effects into consideration and re-estimate the equilibrium charge density in the dust-plasma system.

Before moving on to the next section, I will introduce two contrasting viewpoints on the chondrule formation mechanism based on the analysis of the meteorite samples. Firstly, if we are to explain *all* the chondrule formation by lightning, there is another problem:

• Redox Problem

Water vapor creates oxidizing environment (Clayton et al., 1981; Rubin, 2005) whereas major population of chondrules is considered to have formed in reducing environment (Lofgren, 1989; Connolly et al., 1994; Jones & Danielson, 1997).

Secondly, there are evidences that *some* of the chondrules were formed by lightning. Wasilewski & Dickinson (2000) reports the analysis of the meteorite samples that include chondrules whose remnant magnetization distribution show both the large average value and the large variance. The large value of remnant magnetization is difficult to explain but for magnetic pulse fields like those associated with the lightning, and the large variance indicates that the thermally processed under largely variable magnetic field had taken place before the meteorite was formed.

The two contrasting observations suggest the multiple origin of the chondrules.

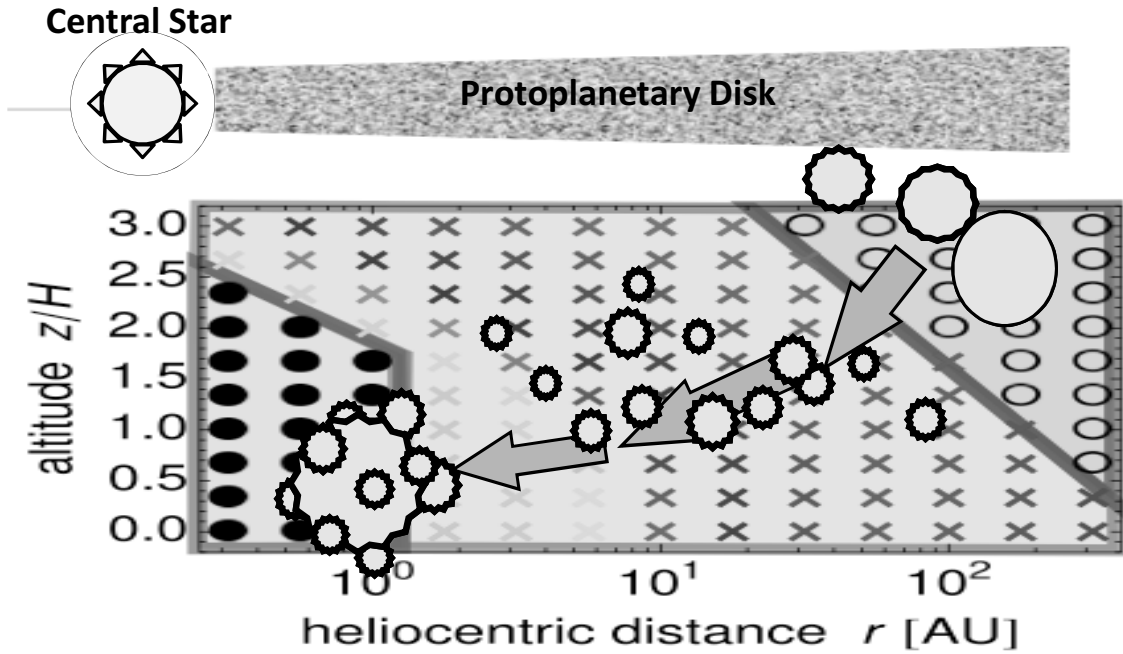


Figure 2.2. Okuzumi (2009) 's estimate on possibilities of planetesimal formations. \times : dust aggregate growth is prohibited by electrostatic repulsion at the very early stage; \circ : dust growth is permitted; \bullet : spontaneous bimodal dust growth. The regions ($1 \sim 100$ au) assumed in the standard scenario as the main sites of planet formation are almost entirely marked by \times ; i.e. planet formation is impossible, unless “seeds” are provided from elsewhere.

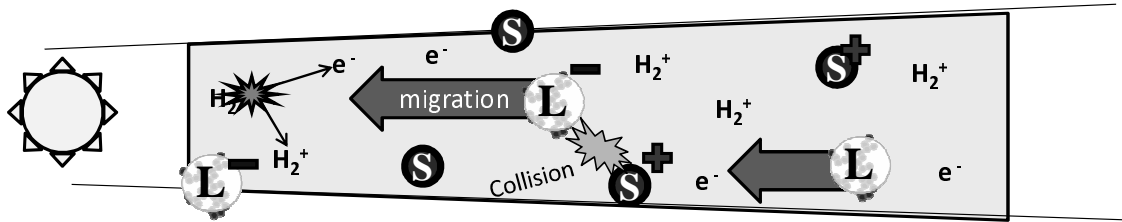


Figure 2.3. The uniform-box model, and the participating particles: Large dust (L); Small dust (S); ionized molecules (H_2^+); electrons (e^-); and neutral molecular gas(H_2). Neutral molecule is ionized by cosmic rays. Charged gas particles are absorbed to dust particles. Dust particles, made of ice, separate charge when they collide. The large dust species has mean velocity compared to other species.

2.1.2 Dust Charging By Plasma Absorption

The ionization degree of a protoplanetary disk is in equilibrium: The main ionization source of the plasma is cosmic ray impacts, creating free electrons and positively charged molecular ions from disk gas medium. A natural question to pose is; what is the main recombination source? The gas phase recombination, where a free electron is captured by an ion and results in a neutral molecule, is inefficient due to low density of the medium. The majority of the recombination takes place on the surface of dust aggregates. Dust surface in protoplanetary disk absorbs charged and neutral gas particles, and act as a catalyst in the chemistry.

Dust aggregates in plasma are negatively charged due to electron absorption. One can formulate the time evolution of the charge q of one dust aggregate as follows:

$$\frac{dq}{dt} = en_i\sigma_i v_i - en_e\sigma_e v_e, \quad (2.1)$$

where e is the elemental charge, subscripts i and e denote the ion and electron respectively, n is the number density of ion or electron, σ is the absorption cross section, v is the relative collision velocity. The ion species whose charge is not +1 are omitted because their amounts are negligible.

The relative collision velocity is dominated by the thermal velocity of the plasma particles. Since the electron mass is lighter than molecular ion species by the factor of several thousands, v_e is of the order of $100v_i$. This causes the dust aggregate to absorb more electron than ions, which makes the dust to charge negatively. The electric repulsive force from the negatively charged dust makes it harder for electrons to hit the dust, and easier for ions. i.e. σ_e becomes smaller while σ_i becomes larger. The equilibrium is reached when $\sigma_i v_i = \sigma_e v_e$. At this point, about 99% of thermal electrons heading to the dust are repulsed away.

The role of dust as plasma absorber and recombination catalyst has been well studied. However, the effect of this negative dust charge on dust coagulation has strangely been ignored until recently. Okuzumi (2009) studied this effect in detail. The result seemed discouraging (Figure 2.2). At the very initial stage of the dust growth, the repulsive force between the negatively charged dust particles is so large that the dust collision is severely hindered and dust growth is frozen in most of the dust-rich regions of the protoplanetary disk. This is explained as follows. At the very beginning of planet formation when the dust is very small, its main velocity is Brownian motion, with the same temperature (kinetic energy) as the plasma. Now each dust is so charged that about 99% of thermal electrons heading to the dust are repulsed away and the charge flux to the dust is in equilibrium. Therefore, another dust, when it has the few times negative charge and the same kinetic energy compared to an electron, almost cannot touch the dust. Thus dust growth by coagulation is frozen.

The dust growth is permitted only at the regions with high altitude and very long distance from the star, where the dust charge is low due to low temperature, and sedimentation speed is large (and is much faster than Brownian motion) due to low disk gas density.

The solution of Okuzumi (2009) is to relax the assumption that all dust aggregates are of equal size. The planetesimal seeds grown at the outer region of the disk eventually begin to migrate inward. Due to the large migration velocity brought by their size, the outsider seeds

can overcome the electrostatic barrier and capture the dust at the growth prohibited region. Crucial point of the model is to take the size distribution of the dust into consideration. The smaller dust, major in their number, absorbs the plasma. Although they themselves cannot grow, they contributes in not making the electrostatic barrier too high, assisting the growth of the larger dust. The larger dust from outside, gathers such smaller dust and become large planetesimals. While the motion of smaller dust is coupled to the fluid, larger dust migrate at its terminal velocity towards the center of gravity.

This situation quite resembles what happens in the rain cloud on Earth. In the cloud, small ice particles are coupled to the ascending air current. At the top of the cloud, larger ice grains are formed. They eventually decouple from the fluid and fall towards the central star (the Earth). The larger ice particles collide with smaller ice particles and grow even larger to become snow or rain. Earth clouds and protoplanetary disks have such phenomena in common; phenomena as the bimodal size distribution, their different response to the gas and the fluid resulting in mean motion between them, and their growth process.

An interesting aspect of ice particles is that they also exchange electric charge when they collide, resulting in lightning under certain conditions. The application of this collisional charge separation mechanism to protoplanetary disks is the main topic of this chapter.

2.1.3 Dust Charge due to Collision of Ice Dust

In this chapter I focus on a local, uniform box at certain orbital radius r near the equatorial plane of the protoplanetary disk (Figure 2.3). I model the protoplanetary disk based on the minimum-mass solar nebula (MMSN) model (Hayashi, 1981), which is accepted as the “standard scenario of planet formation.”

There are five species of particle in the model (cf. Table 2.1): Large and small dust made of ice; ionized molecule(i); electrons(e); and neutral gas molecule(g). For each species I the goal is to calculate the charge per particle q_I , number density n_I , and charge density carried by the species $Q_I = q_I n_I$. The dust distribution is not necessary bimodal: various dust species are classed into two groups, and the two dust (L) and (S) are representatives, or averages. Depending on which phase of the disk or which kind of the disk you consider, the parameters (e.g. radii, material density, surface condition ...) of the dust species may vary. The most focused parameter is \mathcal{N} , the number density of the dust in units of MMSN value. Dependencies on \mathcal{N} can either be interpreted as time dependency (as dust sedimentation or condensation proceed, \mathcal{N} increase with time) or simply as different types of disk (some disk has more dust than other.)

The question is twofold:

1. For a certain combinations of dust parameters, how does the dust charge Q_I and the generated electric field in the fluid comoving frame E' depend on \mathcal{N} ? This question is the theme of this section, and is detailed along with introducing the components of the models in §2.2.
2. On answering the first question, I define $\mathcal{N}_{\text{crit}}$ so that $E(\mathcal{N}_{\text{crit}}) = E_{\text{crit}}$; when the dust number density \mathcal{N} increase while other dust parameters are fixed, the generated electric field E' gradually rises, and $\mathcal{N} = \mathcal{N}_{\text{crit}}$ is the point lightning strikes. My

second task is to determine N_{crit} as functions of dust parameters. This is the subject of §2.3.

2.2 Dust Changing Model

2.2.1 The Disk Model

The protoplanetary disk models accepted in this thesis are based on the MMSN as follows. The gas surface density $\Sigma_g^{\bowtie}(r)$, disk scale height $h^{\bowtie}(r)$, and the temperature $T^{\bowtie}(r)$ of the disk are

$$\Sigma_g^{\bowtie}(r) = 1.7 \times 10^3 \left(\frac{r}{\text{au}} \right)^{-\frac{3}{2}} \text{ g cm}^{-2}, \quad (2.2)$$

$$h^{\bowtie}(r) = 4.7 \times 10^{-2} \left(\frac{r}{\text{au}} \right)^{\frac{5}{4}} \text{ au}, \quad (2.3)$$

$$T^{\bowtie}(r) = 2.8 \times 10^2 \left(\frac{r}{\text{au}} \right)^{-\frac{1}{2}} \text{ K}, \quad (2.4)$$

where r is the distance from the central star. This leads to gas density distribution

$$\rho_g^{\bowtie}(r) = 2.4 \times 10^{-9} \left(\frac{r}{\text{au}} \right)^{-\frac{11}{4}} \text{ g cm}^{-3}. \quad (2.5)$$

The dust-to-gas ratio in MMSN is $\simeq 1.0 \times 10^{-2}$.

I use the model by Cuzzi & Zahnle (2004), and introduce two species of dust, the smaller and the larger. I further assume that the surface density of the larger dust is 10% of the total dust surface density. These two species are also either ‘cationic’ and ‘anionic.’ The ‘cationic’ species receives the positive electric charge through dust-dust collision. I can also represent the role of various molecular ions by one abstract ion species ‘i,’ according to Okuzumi (2009)’s notations.

There are two motivations for employing this two-dust model. First, the two dust model is the simplest model that can handle the dust-dust collisional charge separation and the macroscopic relative velocity between the dust species. Second, the charge tendency of the dust aggregates is strongly correlated to their size. In one scenario, older dust aggregates are larger and also anionic. In another scenario, dust aggregates made of ice are larger and also cationic compared to dust aggregates made of silicate. (see §2.2.5 for the details.) Therefore, instead of considering four (cationic smaller dust, cationic larger dust, anionic smaller dust, and anionic larger dust) species of dust, I will correlate two size species with two charge tendency species, (Table 2.1), and consider that there are two species of dust. However, both correspondences (smaller dust is cationic / larger dust is cationic) are possible.

To summarize, the fiducial values for the density of the smaller dust $\rho_s^{\bowtie}(r)$ and the density of the larger dust $\rho_L^{\bowtie}(r)$ are

$$\rho_s^{\bowtie}(r) = 1.0 \times 10^{-2} \rho_g(r), \quad (2.6)$$

$$\rho_L^{\bowtie}(r) = 1.0 \times 10^{-3} \rho_g(r). \quad (2.7)$$

symbol	value/dimension	meaning	definition
— constants —			
r	2.7 au	orbital radius considered	-
Σ_g^{\bowtie}	$3.8 \times 10^2 \text{ g cm}^{-3}$	gas surface density of MMSN	(2.2)
h^{\bowtie}	$1.6 \times 10^{-1} \text{ au}$	scale height of MMSN	(2.3)
T^{\bowtie}	$1.7 \times 10^2 \text{ K}$	temperature of MMSN	(2.4)
ρ_g^{\bowtie}	$1.6 \times 10^{-10} \text{ g cm}^{-3}$	gas density of MMSN	(2.5)
ρ_s^{\bowtie}	$1.6 \times 10^{-12} \text{ g cm}^{-3}$	spatial density of smaller dust in MMSN	(2.6)
ρ_L^{\bowtie}	$1.6 \times 10^{-13} \text{ g cm}^{-3}$	spatial density of larger dust in MMSN	(2.7)
\mathcal{N}_{ch}	0.1	charge exchange efficiency	§2.2.5-I
σ_{ch}	$6.2 \times 10^9 \text{ e cm}^{-2}$	charge surface density	§2.2.5-I
u_L	$3.4 \times 10^3 \text{ cm sec}^{-1}$	bulk velocity of larger dust to other species	§2.2.7
v_I	$\sqrt{k_B T/m_I}$	random velocity of particles of species I	§2.2.7
$\Delta v_{L,s}$	$3.4 \times 10^3 \text{ cm sec}^{-1}$	mean collision velocity between a smaller dust and a larger dust	§2.2.7
— independent variables —			
\mathcal{N}	1	dust number density of the considered region divided by that of the MMSN model	
r_I	cm	radius of a dust aggregate of species I	(2.29)
D_I	1	fractal dimension of a dust aggregate of species I	(2.29)
— dependent variables —			
m_I	cm	mass of a dust aggregate of species I	(2.30)
ρ_s	g cm^{-3}	condensed density of smaller dust	$\mathcal{N} \rho_s^{\bowtie}$
ρ_L	g cm^{-3}	condensed density of larger dust	$\mathcal{N} \rho_L^{\bowtie}$
n_I	cm^{-3}	number density of dust I in condensed regions	ρ_I/m_I
q_I	esu	The charge carried by a single particle of I	-
Q_I	esu cm^{-3}	The charge density carried by species I	$q_I n_I$
$J_{I,I'}$	$\text{esu cm}^{-3} \text{ s}^{-1}$	charge transferred from species I to species I' per unit time per unit volume	(2.45-2.50)
S_{kiss}	cm^2	contact surface area within a dust-dust collision	(2.39)
$\Delta q_{A,C}$	esu	amount of charge exchanged within one collision	$\mathcal{N}_{ch} \sigma_{ch} S_{\text{kiss}}$
σ_{cou}	cm^2	cross section between two charged particles	(2.31),(2.32)
j_D	$\text{esu cm}^{-2} \text{ s}^{-1}$	current carried by dust particles	§2.3
j_p	$\text{esu cm}^{-2} \text{ s}^{-1}$	current carried by plasma particles	§2.3
E_{dis}	G	critical electric field strength for lightning	(2.77)
E_{\max}	G	(local maximum of) electric field generated in the protoplanetary disk	(2.82)
χ	1	whether the collision cross section between smaller dust and plasma particles are geometric ($\chi \ll 1$) or Coulomb ($\chi \gg 1$)	(2.101)
$\mathcal{N}_{\text{crit}}$	1	the dust number density at which lightning takes place	(2.110) and (2.112-2.114)

Table 2.2. The list of symbols frequently used in this chapter.

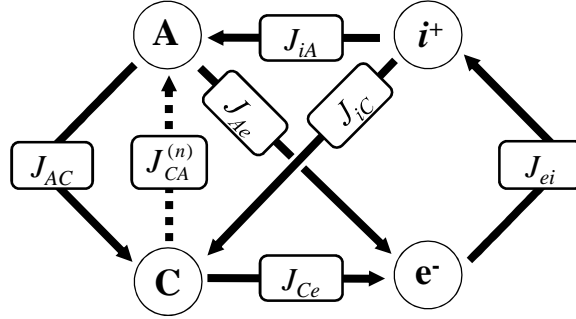


Figure 2.4. The circuit diagram of the charge exchange process in dust plasma. Each arrow represents ‘current’ density J , which has the unit $\text{esu cm}^{-3}\text{s}^{-1}$, the amount of charge passed from one component to the other per unit disk volume per unit time. The arrow points from the component that receives negative charge to the component that receives positive charge. In this figure, i and e are ions and electrons created from ionizing neutral disk gas. C and A are cationic and anionic dust.

J_{ei} represents gas ionization as ‘current’ from e vertex to i vertex; J_{iA} , J_{iC} , J_{Ae} , and J_{Ce} are ion and electron absorption to dust; J_{AC} is dust-dust collisional charge separation and $J_{CA}^{(n)}$ is neutralization current of charged dust-dust absorption.

I further assume that within the focused region, density for each dust component of the disk is multiplied from the MMSN by the factor \mathcal{N} . Then the density of gas, smaller dust and larger dust is given by

$$\rho_g = \rho_g^{\bowtie}(r), \quad (2.8)$$

$$\rho_s = \mathcal{N} \rho_s^{\bowtie}(r), \quad (2.9)$$

$$\rho_L = \mathcal{N} \rho_L^{\bowtie}(r). \quad (2.10)$$

Let mass of the smaller dust and the larger dust be m_s and m_L , respectively. Then, number density is defined by:

$$n_s = \frac{\rho_s}{m_s}, \quad (2.11)$$

$$n_L = \frac{\rho_L}{m_L}. \quad (2.12)$$

I estimate the mass as a function of the dust radius and the fractal dimension in §2.2.3.

2.2.2 Charge Exchange Equations

There are four species of charge carrier in the model — ions, electrons, cationic, and anionic dust (Table 2.1.) Charge exchange processes between these species considered here are ionization, plasma absorption, and dust-dust collision/neutralization (Figure 2.3.)

I label the particle species with letter **I**. The charge density carried by species **I** is Q_I (the unit is esu cm^{-3}), and the charge transferred from species **I** to species **I'** is $J_{I,I'}$ (the unit is $\text{esu cm}^{-3} \text{s}^{-1}$).

The charge density Q_I of a species I is the product of their number density n_I and their average charge per particle q_I . For dust species, I assume that n_I is known from number density model while q_I is unknown; for ion and electrons I assume q_I to be known but n_I not. This constitutes the four dynamical equations for four unknown variables q_A, q_C, n_i, n_e :

$$\frac{dq_A}{dt} = \frac{1}{n_A}(-J_{A,C} + J_{i,A} - J_{A,e} + J_{C,A}^{(n)}), \quad (2.13)$$

$$\frac{dq_C}{dt} = \frac{1}{n_C}(J_{A,C} + J_{i,C} - J_{C,e} - J_{C,A}^{(n)}) \quad (2.14)$$

$$\frac{dn_i}{dt} = \frac{1}{q_i}(J_{e,i} - J_{i,A} - J_{i,C}) \quad (2.15)$$

$$\frac{dn_e}{dt} = \frac{1}{q_e}(-J_{e,i} + J_{A,e} + J_{C,e}). \quad (2.16)$$

The current terms $J_{I,I'}$ are

$$J_{A,C} = \Delta q_{A,C} n_A n_C \sigma_{A,C} \Delta v_{A,C} \quad (2.17)$$

$$J_{C,A}^{(n)} = |q_S| n_A n_C \sigma_{A,C}^{(n)} \Delta v_{A,C} \quad (2.18)$$

$$J_{i,A} = e n_i n_A \sigma_{cou}(q_A, e) v_i \quad (2.19)$$

$$J_{i,C} = e n_i n_C \sigma_{cou}(q_C, e) v_i \quad (2.20)$$

$$J_{A,e} = e n_e n_A \sigma_{cou}(q_A, -e) v_e \quad (2.21)$$

$$J_{C,e} = e n_e n_C \sigma_{cou}(q_C, -e) v_e \quad (2.22)$$

$$J_{e,i} = \zeta n_g \quad (2.23)$$

where I have included neutral gas ionization $J_{e,i}$, dust-plasma absorption $J_{A,i}, J_{C,i}, J_{A,e}, J_{C,e}$, dust-dust collisional charge-up $J_{A,C}$, and dust-dust collisional neutralization $J_{C,A}^{(n)}$ terms. Here, v_i and v_e are the thermal velocity of the ions and the electrons, n_g is the number density of the neutral gas, ζ is the ionization rate, which is dominated by cosmic ray ionization near equatorial, $r = 2.7$ au of MMSN (Umebayashi & Nakano, 2009).

The problem then is to solve the equilibrium equations for the dynamic equations (2.13)-(2.16):

$$-J_{A,C} + J_{i,A} - J_{A,e} + J_{C,A}^{(n)} = 0 \quad (2.24)$$

$$J_{A,C} + J_{i,C} - J_{C,e} - J_{C,A}^{(n)} = 0 \quad (2.25)$$

$$J_{e,i} - J_{i,A} - J_{i,C} = 0 \quad (2.26)$$

$$-J_{e,i} + J_{A,e} + J_{C,e} = 0, \quad (2.27)$$

together with charge neutrality equation:

$$Q_A + Q_C + Q_i + Q_e = 0. \quad (2.28)$$

I use circuit diagram (Figure 2.4) to depict the dynamical equations (2.13)-(2.16), and to interpret the numerical equilibrium solutions (2.24)-(2.28) in §2.2.8. The circuit diagram

represents charge-exchange processes; each vertex represents the species of charge reservoir and each arrow represents the charge exchange process. The size of the vertex circles represents the amount of charge Q_I . The thickness of the arrows represents the amount of charge transfer $J_{I,I'}$. I define the direction of the arrows so that the arrows point to the positive charge receivers.

In the system of equations depicted by a circuit diagram, charge density of each vertex Q_I corresponds to an unknown quantities. Therefore, the number of unknown quantities is equal to the number of vertexes N_V . On the other hand, at the equilibrium, sum of the current flowing into each vertex is required to be zero (Kirchhoff's Laws); this gives us N_V equations but only $N_V - 1$ of them are independent. Charge neutrality gives us 1 equation. Thus I have N_V equations for N_V unknown values.

2.2.3 Fluffy Dust Model

I use model of dust aggregates by Wada et al. (2008). cf. Figure 2.1. Dust aggregates are modeled to be composed of a large number of spherical monomers with radius $r_m \simeq 0.1 \mu\text{m}$. Each dust species \mathbf{I} has its mass $m_{\mathbf{I}}$, the number of monomers that constitute the dust $N_{\mathbf{I}}$, and representative radius $r_{\mathbf{I}}$. I define the fractal dimension of the fluffy dust $D_{\mathbf{I}}$ in the following simple manner:

$$N_{\mathbf{I}} = \left(\frac{r_{\mathbf{I}}}{r_m}\right)^{D_{\mathbf{I}}}. \quad (2.29)$$

The dust mass is expressed in terms of monomer mass m_m as follows:

$$m_{\mathbf{I}} = m_m N_{\mathbf{I}} = m_m \left(\frac{r_{\mathbf{I}}}{r_m}\right)^{D_{\mathbf{I}}}. \quad (2.30)$$

Wada et al. (2008) study the collision of the fluffy dust of the radii $1.0 \times 10^{-5} \sim 9.1 \times 10^{-4}$ cm. The effect of offset collisions, collision between dust aggregates of much different sizes, and dust aggregates much larger than 9.1×10^{-4} cm have not been confirmed. Therefore I make the following assumptions on smaller dust-larger dust collision.

- If the smaller dust graze at the larger dust, i.e. if the line that passes the gravitational center of the smaller dust and is parallel to the relative velocity vector does not intersect with the larger dust, two dust aggregates do not stick to each other. Therefore the grazing cross section is of the order $r_s r_L$. In this case they separate $\Delta q_{A,C}$ of charge, which is the product of charge surface density σ_{ch} and contact surface area S_{kiss} . This contributes to the dust-dust charging current, $J_{C,A}$.
- If the smaller dust bump into the larger dust, i.e. if the line that passes the gravitational center of the smaller dust and is parallel to the relative velocity vector does intersect with the larger dust, the smaller dust do not penetrate the larger dust but becomes a part of the larger dust. The cross section is of the order r_L^2 . In this case all the charges of the smaller dust are removed from the smaller dust charge density and added up to the larger dust charge density. This contributes to the dust-dust neutralization current, $J_{C,A}^{(n)}$.

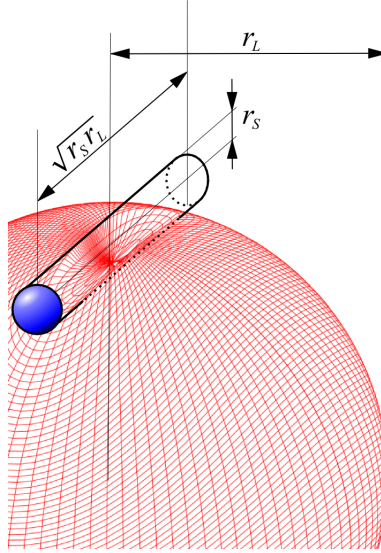


Figure 2.5. A grazing collision between a smaller dust (the solid sphere) and a larger dust (the wire-frame sphere). The smaller dust creates a trench on the larger dust (the black cylinder). Be noted that two spheres are not solidly filled; they are filled with μm -sized monomers and there are lots of space.

2.2.4 Collisional Cross Section and Contact Surface of Charged Fluffy Dust

In this section, I estimate collisional cross sections for dust. The collisional cross sections for two electrically charged spherical particle is given by

$$\sigma_{cou}(q) = \pi a^2 \exp\left(-\frac{qq'}{ak_B T}\right) \quad (qq' > 0), \quad (2.31)$$

$$\sigma_{cou}(q) = \pi a^2 \left(1 - \frac{qq'}{ak_B T}\right) \quad (qq' < 0) \quad (2.32)$$

where q and q' are particles' charges, T is the temperature of their relative motion and πa^2 is the geometric cross section (e.g. Spitzer, 1941).

Equation (2.32) represents the effect of Coulomb focusing: particles of the opposite charge attract each other and collide more often than when they are neutral. On the limit $|qq'a^{-1}| \gg k_B T$ the cross section is approximated as $\sigma_{cou}(q) \simeq -\pi a q q' (k_B T)^{-1}$, which is bi-linear on q and q' . On the other hand, cross section (2.31) represents the effect of Coulomb repulsion: for the collision between particles of the same charge only a portion of particles that belongs to the long tail of Boltzmann's distribution for temperature T can overcome the Coulomb barrier and collide. On the limit $qq'a^{-1} \gg k_B T$ the cross section vanishes quickly, but never reaches 0.

I use this Coulomb cross sections (2.31) and (2.32) to estimate the event rate of gas-dust collision and dust-dust collision.

The amount of charge exchanged in a collision, $\Delta q_{A,C}$, is product of area of contact S_{kiss} , upper limit of charge exchanged per unit surface area of contact σ_{ch} , and the non-

dimensional efficiency factor \mathcal{N}_{ch} . The detailed argument to determine $\mathcal{N}_{ch}\sigma_{ch}$ is done in §2.2.5. Here I assume that $\mathcal{N}_{ch}\sigma_{ch}$ is known and describe how to estimate contact surface area S_{kiss} . Since it requires another detailed simulation to estimate S_{kiss} qualitatively, I resort to an order-of-magnitude estimate for this part of the work.

Figure 2.5 illustrates the collision between a smaller dust and a larger dust. The smaller dust grazes the larger dust, pushes away the monomers that belong to the larger dust and creates a trench on the larger dust. The trench is a portion of the black cylinder in the figure. The radius and the length of the cylinder are r_s and $(r_s r_L)^{1/2}$, respectively. Therefore, the surface area of the trench S_C is of order

$$S_C \simeq r_s^{3/2} r_L^{1/2}, \quad (2.33)$$

and the number of monomers N_C required to fill the surface of the trench is

$$N_C \simeq r_m^{-2} r_s^{3/2} r_L^{1/2}. \quad (2.34)$$

Their total surface area is also of the order of S_C .

However, $S_{kiss} \simeq r_s^{3/2} r_L^{1/2}$ overestimates the actual contact surface area if the large dust is so fluffy that there is not enough monomers in the trenched volume to fill the trench surface. The overestimation must be corrected for as follows.

From the definition of the fractal dimension (2.29), the number density of monomers within the larger dust material is

$$n_L^{(M)} = N r_L^{-3} = r_m^{-D_L} r_L^{D_L - 3}. \quad (2.35)$$

On the other hand the volume of the trench is

$$V_F \simeq r_s^{5/2} r_L^{1/2}. \quad (2.36)$$

Therefore, the number of particle contained in the trench is

$$N_F = n_L^{(M)} V_F \simeq r_m^{-D_L} r_s^{5/2} r_L^{D_L - 5/2}, \quad (2.37)$$

and their total surface area is

$$S_F \simeq r_m^2 N_F \simeq r_m^{2-D_L} r_s^{5/2} r_L^{D_L - 5/2}. \quad (2.38)$$

If $N_F < N_C$, the surface of the trench is only partially covered by the monomers, and I estimate $S_{kiss} \simeq S_F$. On the other hand, if $N_F > N_C$, N_F monomers are crushed onto the trenched surface, and since they overlap, about N_C monomers will take part in the charge exchange. In this case I estimate $S_{kiss} \simeq S_C$. To summarize, I assume that S_{kiss} is the smaller of (2.33) or (2.38):

$$S_{kiss} = \min(r_s^{3/2} r_L^{1/2}, r_m^{2-D_L} r_s^{5/2} r_L^{D_L - 5/2}). \quad (2.39)$$

2.2.5 Charge Separation Processes

There are generally two classes of possible charge separation processes in protoplanetary disks.

One is surface charge exchange, where each dust has some kind of spontaneous charge separation (Kudin & Car, 2008), so at the initial condition each dust charge is zero as a whole (globally neutral), but charge separation is present within the dust particles (locally charged). For example, water ice crystals tend to gather negative charge at its surface and positive charge inside. When two dust aggregates with different charge collide and melt partially, they exchange molten material and the charge included in the molten material. As a result each dust gets globally charged.

The other charge separation mechanism may be triboelectric processes (e.g. Desch & Cuzzi, 2000). In this case, at the initial condition each dust is both globally and locally neutral. When two dust aggregates made of materials with different electron affinity collide, the surface electrons move from one material to the other. As a result each dust gets globally charged.

Surface Charge Exchange I — Larger Dust is Anionic

One of the plausible mechanisms for the dust-dust collisional charge separation is the surface charge exchange between ice dust. For the dust aggregate of ice mantled silicate, Cuzzi & Zahnle (2004) proposed a condensation scenario, that larger dust aggregates made of ice drifting inward will dissociate at the snow line and many smaller dust aggregates are formed.

There are established models on charge separation caused by ice-ice dust collision in the context of thundercloud meteorology (e.g. Dash et al. (2001)). I will import them as a charge separation model in protoplanetary disks. The essential steps to cause lightning on earth are (1) spontaneous charge separations on ice crystal surfaces, (2) existence of different dust species with different spontaneous charge separation per surface area, (3) collisions between the different dust that lead to global charging of each dust and (4) relative motion between the globally charged dust to create electrostatic field.

For (1), I assume that the charge separation per surface area is quantitatively the same as the values measured in laboratory experiments. For (2), dominating dust species in charge separation process in protoplanetary disks is uncertain, and we discuss two possibilities (cf. §2.2.5-I, §2.2.5-II) in this work. For (3) and (4), we make simple estimations for the collision rate and relative velocity in protoplanetary disks.

Ice crystal surface is intrinsically charge-separated. Ice is negatively charged near the surface, and the inside is positive. The typical charge surface density for stable ice surface is $\sigma_{ch} \simeq 3.0 \text{ esu cm}^{-2}$ or $\sigma_{ch} \simeq 6.2 \times 10^9 \text{ e cm}^{-2}$ and the typical skin depth of the charged layer is $d_{ch} \simeq 2.0 \times 10^{-4} \text{ cm}$, though charge surface density for fast-growing ice surfaces is larger and shallower (Dash et al., 2001). This charge separation has a general explanation as a result of interaction between hydroxide(OH^-) and hydronium (H_3O^+) ions and a hydrophobic surface (Kudin & Car, 2008; Muranushi & Tomiyasu, 2009), and the above value of typical charge surface density is observed at liquid water-air surfaces as well as at ice crystal-air surfaces (Takahashi, 2005). Therefore I use the value for ice-vacuum surfaces as well.

In the thundercloud, there are a variety of ice crystals with different surface charge densities, depending on the surface history of the ice crystals. Newly formed surfaces have larger charge surface density than old surfaces, because they have higher fractal dimension and deeper amorphous layers.

I now consider how surface charge exchange works in the model of Cuzzi & Zahnle (2004). Larger dust aggregates that migrate towards the snow line have old surface and have less negative charge surface density, while smaller dust aggregates formed at the snow line have new surface and larger negative charge surface density, as in meteorological case. Note that before collision each dust is globally neutral.

At the collision, the surface of the dust aggregates melts and the surface charge density is exchanged, and averaged. The larger dust aggregate, having less surface charge density than the smaller one, receives more negative charge than they give. Therefore the larger dust becomes anionic, smaller dust becomes cationic.

Laboratory experiments (Takahashi, 1978), in-situ observations and meteorological estimates (Gaskell et al., 1978; Christian et al., 1980) suggest that for mm-size ice crystals, at least 10 per cent of the total surface charge within contact surface is exchanged in a single collision; experiments by Mason & Dash (2000); Dash et al. (2001) suggests almost $\mathcal{N}_{ch} = 1.0$. As a conservative estimate, I use $\mathcal{N}_{ch} = 0.1$ unless mentioned otherwise.

Surface Charge Exchange II — Larger Dust is Cationic

It may be possible that charge separation processes in protoplanetary disks are different from those in the terrestrial thunderclouds. The collision time-scale in the protoplanetary disks is much longer than that in a thundercloud, so long that sintering may take place (Sirono, 1999). As a result, The surface state of old ice larger dust and young ice smaller dust might resemble each other. If they are identical, they do not exchange charge on average, although some random charge exchange by collision is still possible.

However, compared to thundercloud, protoplanetary disks are more dirty and fine-grained; they contain much dust made of materials other than ice such as silicates, and the monomer size is $0.1 \mu\text{m}$ rather than 1 mm. Since the monomer size is smaller than typical skin depth of the charge separation $d_{ch} \simeq 2.0 \times 10^{-4} \text{ cm}$ mentioned above, it is possible that ice smaller dust and silicate smaller dust with thin ice mantles formed at the snow line is inefficient in separating charge. There may be silicate aggregates with no surface charge separation. Meanwhile old larger dust that have traveled from the far end of the protoplanetary disk have undergone sintering and have developed thick mantles with full surface charge separation.

In such scenario, the larger dust has more surface charge separation than the smaller dust. Therefore, collision between a larger dust and a smaller dust still leads to charge separation but the larger dust becomes cationic, and the smaller dust is anionic in this case. I assume that $\mathcal{N}_{ch} = 0.1$ and $\sigma_{ch} \simeq -3.0 \text{ esu cm}^{-2}$ in this case (The charge exchange rate has the same magnitude but the opposite sign compared to that of §2.2.5-I.)

Both scenarios, the larger dust is anionic and the larger dust is cationic are plausible. They may even take place in the different parts of the same disk simultaneously. Therefore, I have decided to take both scenarios into consideration. To that end, I have introduced the concept of cationic and anionic dust separate from the concept of the size of the dust.

2.2.6 Relative Velocity

When a cloud of positively and negatively charged dust is separated much larger than plasma Debye length

$$\begin{aligned}\lambda_D &= \sqrt{\frac{T}{4\pi n_i e^2}} \\ &= 4.0 \times 10^2 \text{ cm} \left(\frac{T}{170K} \right)^{\frac{1}{2}} \left(\frac{n_i}{5.0 \times 10^{-2} \text{ cm}^{-3}} \right)^{-\frac{1}{2}}\end{aligned}\quad (2.40)$$

the electrostatic field between them become observable. In order to cause such macroscopic charge separation, there must be a significant relative bulk motion between anionic and cationic dust. Inward migration of large dust is a source of this bulk motion. The sedimentation may act in the same way. Also Desch & Cuzzi (2000) have proposed that largest eddies in turbulence of protoplanetary disks cause bulk motion between smaller dust and larger dust. Such effects on the relative velocity between dust species in MMSN has been studied (see Brauer et al. (2008) and references therein).

Here, I simply assume that the largest contribution to the smaller dust-larger dust relative velocity is the bulk motion of the larger dust, and the velocity is $\Delta v_{L,S} \equiv u_L \equiv 3.4 \times 10^3 \text{ cm s}^{-1}$, the catastrophic collision velocity of the ice dust aggregates of $9.1 \times 10^{-4} \text{ cm size dust}$ (Wada et al., 2008). Note that the non-sticking velocity threshold decrease as the monomer size increase (Blum & Wurm, 2000). I also test the analytic formulae with smaller values of $\Delta v_{L,S}$ and u_L assumed.

Dust migration speed are comparable to this value at some stages of the dust growth. On the other hand, turbulent motion is faster than the value for most of the parameter range. Turbulent mode that is larger than the scale of interest can be treated as bulk motion, and can be used to explain the charge separations of the scale. The scale can be as large as of order of disk scale-height (Balbus & Hawley, 1991).

2.2.7 The Charge Equilibrium Equations

Substituting the results of analyses up to here into equations (2.13-2.16) gives the following dynamic equation for charge transport:

$$\frac{dQ_L}{dt} = -J_{L,S} - J_{L,i} - J_{L,e} \quad (2.41)$$

$$\frac{dQ_S}{dt} = J_{L,S} - J_{S,i} - J_{S,e} \quad (2.42)$$

$$\frac{dQ_i}{dt} = J_{L,i} + J_{S,i} - J_{i,e} \quad (2.43)$$

$$\frac{dQ_e}{dt} = J_{L,e} + J_{S,e} + J_{i,e}, \quad (2.44)$$

where the current density terms (2.17-2.23) become:

$$\begin{aligned} J_{L,S} &= \left(\frac{2r_s}{r_L} \Delta q_{A,C} - \frac{Q_s}{n_s} \right) n_s n_L \Delta v_{L,S} \\ &\quad \sigma_{cou} \left(\frac{Q_L}{n_L}, \frac{Q_s}{n_s}, r_L, \frac{1}{2} m_s \Delta v_{L,S}^2 \right) \end{aligned} \quad (2.45)$$

$$J_{L,i} = -Q_i n_L \sigma_{cou} \left(\frac{Q_L}{n_L}, e, r_L, k_B T \right) v_i \quad (2.46)$$

$$J_{L,e} = -Q_e n_L \sigma_{cou} \left(\frac{Q_L}{n_L}, -e, r_L, k_B T \right) v_e \quad (2.47)$$

$$J_{S,i} = -Q_i n_S \sigma_{cou} \left(\frac{Q_s}{n_s}, e, r_s, k_B T \right) v_i \quad (2.48)$$

$$J_{S,e} = -Q_e n_S \sigma_{cou} \left(\frac{Q_s}{n_s}, -e, r_s, k_B T \right) v_e \quad (2.49)$$

$$J_{i,e} = -e \zeta n_g. \quad (2.50)$$

In (2.45), the amount of current exchange $\Delta q_{A,C}$ is product of contact surface area S_{kiss} and surface charge density σ_{ch} , each described in §2.2.4 and §2.2.5. The contact surface area S_{kiss} is the function of dust radii and dust fractal dimensions; see equation (2.39). The surface charge density σ_{ch} depends on the dust material. The relative velocity of the larger dust and the smaller dust is $\Delta v_{L,S} = 3.4 \times 10^3 \text{ cms}^{-1}$, as I have discussed in §2.2.6. The cross section term σ_{cou} is the Coulomb cross section introduced in §2.2.4. I assume v_i and v_e to be thermal velocities of ions and electrons. For ionization in MMSN at $r = 2.7 \text{ au}$, cosmic ray ionization is the main contributor and $\zeta \simeq 10^{-18}$ (Umebayashi & Nakano, 2009). I introduce the non-dimensional dust number density \mathcal{N} (dust number density in unit of MMSN values), so that in equations (2.8-2.10), $\mathcal{N}_g = 1$, and $\mathcal{N}_s = \mathcal{N}_L = \mathcal{N}$. From those density term, the number density terms n_g, n_s, n_L are given as $\rho_g/m_g, \rho_s/m_s, \rho_L/m_L$. The masses of dust aggregates m_s, m_L are function of their radii and fractal dimensions; see equation (2.30).

All the variables that appear in the current density terms (2.45-2.50) are controlled by five parameters; radii of the dust aggregates (r_s, r_L), their fractal dimension (D_s, D_L), and the non-dimensional dust number density \mathcal{N} .

The equilibrium equations (2.24-2.28) become:

$$-J_{L,S} - J_{L,i} - J_{L,e} = 0 \quad (2.51)$$

$$J_{L,S} - J_{S,i} - J_{S,e} = 0 \quad (2.52)$$

$$J_{L,i} + J_{S,i} - J_{i,e} = 0 \quad (2.53)$$

$$J_{L,e} + J_{S,e} + J_{i,e} = 0 \quad (2.54)$$

$$Q_L + Q_s + Q_i + Q_e = 0. \quad (2.55)$$

Again note that, out of four Kirchhoff's Laws (2.51-2.54) only three of them are independent, and the charge neutrality condition (2.55) is necessary.

(a)	ion-electron plasma phase	$ Q_e \simeq Q_i$ (in this thesis $2 Q_e > Q_i$)
(b)	ion-dust plasma phase	$2 Q_e < Q_i$, $ J_{A,C} < J_{A,e} $
(c)	charge-up phase	$ J_{A,e} < J_{A,C} < J_{i,C} $
(d)	dust phase	$ J_{i,C} < J_{A,C} $

Table 2.3. The names and conditions for four phases of charge separation. They are basically named after dominant charge carrier of each phase.

2.2.8 Four Phases of Charge Separation

I have found that as \mathcal{N} is increased while other dust parameters kept constant, the equilibrium charge densities $Q_i = q_i n_i$ experience four phases (Table 2.3). Figure 2.6 shows the typical four phases behavior.

In this and following sections, I explain the origin of the four phases, using the circuit diagrams (Figure 2.7) as a great help. The four-phase behavior I describe here is independent of most of the details of charge exchange processes. For example, the evolutions are almost similar when the opposite sign for dust-dust collisional charge exchange is assumed (§2.2.5-I v.s. §2.2.5-II.) The rest of the discussion in following sections is based on the §2.2.5-I case. The discussion is easily generalized to the other case.

To analyze the result, I first identify the dominant processes by comparing the competitive current in circuit diagram, then write down all the unknown values in simple polynomials of \mathcal{N} . Figure 2.7 illustrates the transition of dominant process in the circuit as dust number density \mathcal{N} increases. The two particles with the largest charge density is marked by larger circle. There are always two of them, one carrying most of the system's positive charge and the other negative, thus charge neutrality holds. The arrows and their line width represents direction and amount of currents. Labels for dominant currents are marked with thick rectangle, sub-dominant currents with thin rectangle, negligible currents with dashed rectangle. The names and conditions for each phase is listed in Table 2.3.

There are two major consequences of the size difference. Larger dust is much fewer in number density. So in the fewer dust limit ($\mathcal{N} \ll 1$) the larger dust carries much less charge density than smaller dust do. Since larger dust is the fewer, one larger dust collides with smaller dust much more often than one smaller dust does with larger dust. Therefore larger dust are the species that experience the quick charge density raise in (c)charge-up phase. The main role of the smaller dust is to absorb plasma and keep the charge neutrality.

Ion-electron Plasma Phase

In ion-electron plasma phase (Figure 2.7 (a)), the dominant path of charge transfer is

$$e^- \rightarrow i^+ \rightarrow C \rightarrow e^-, \quad (2.56)$$

the next-dominant path is

$$i^+ \rightarrow A \rightarrow e^-. \quad (2.57)$$

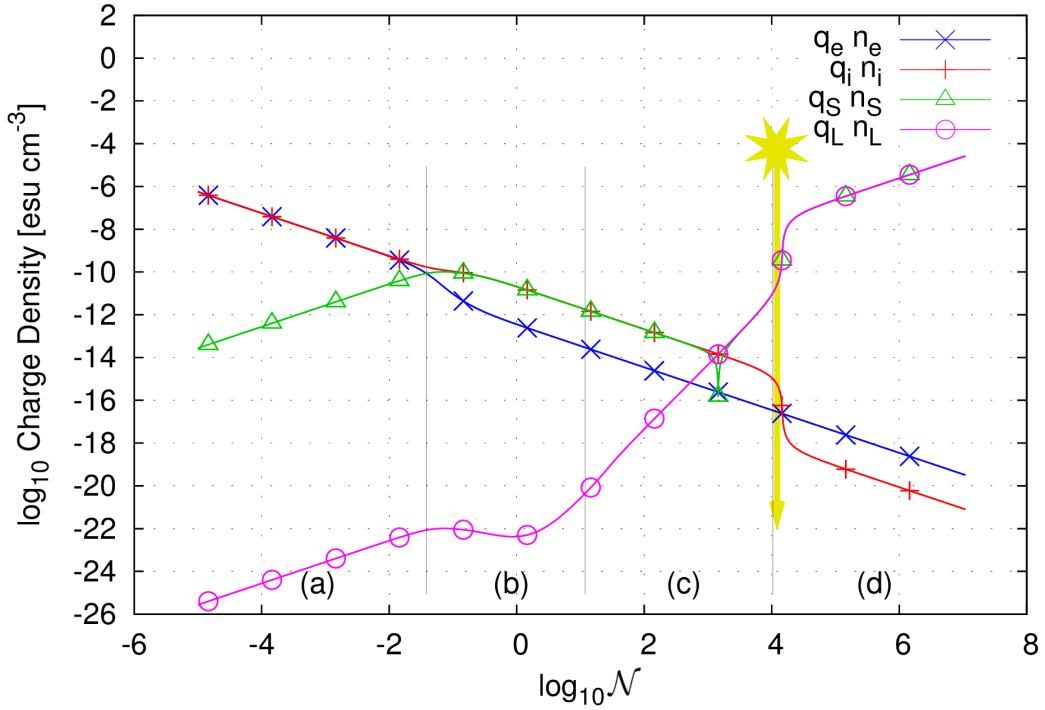


Figure 2.6. Amount of charge stored in each species, en_e , en_i , $|q_s| n_s$, and $|q_L| n_L$, as functions of N . This figure is for ice dust-ice dust case, so larger dust is anionic and smaller dust is cationic. The polarity matches that of Figure 2.7. The radius of smaller dust, radius of larger dust, fractal dimension of smaller dust, fractal dimension of larger dust are 1.0×10^{-4} cm, 1.0×10^2 cm, 3.0, and 3.0 respectively. (a), (b), (c), and (d) corresponds to the four phases described in §2.2.8. The yellow arrow denotes the critical number density N where the macroscopic electric discharge condition (2.84) is met. The settings of the simulation that produces this figure is in the Table. 2.2. This result was first presented in Muranushi (2010).

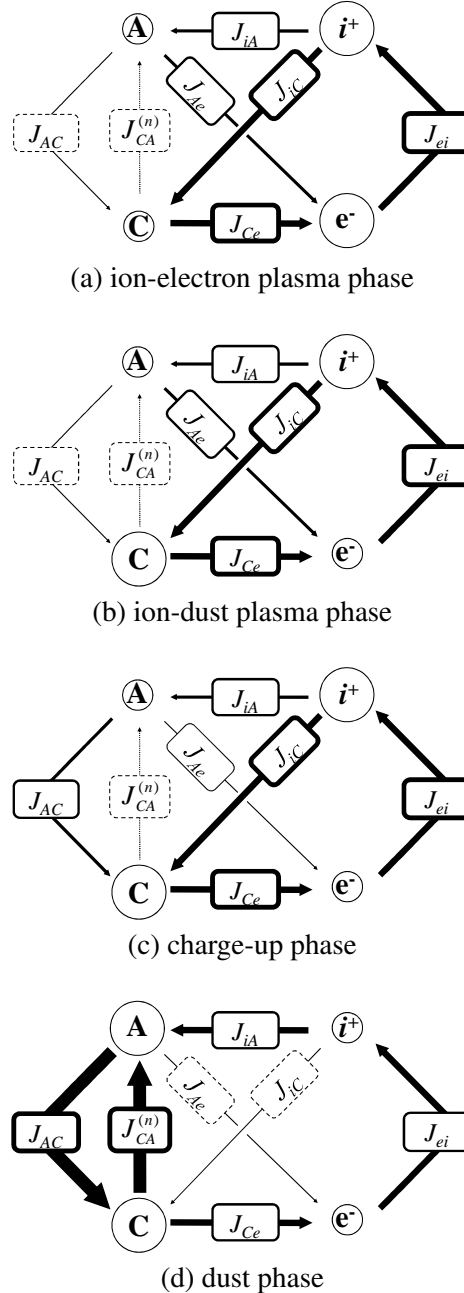


Figure 2.7. The evolution of the charge density and current density as \mathcal{N} increase. As dust number density \mathcal{N} increase, $J_{e,i} \propto \mathcal{N}^0$ is constant while $J_{A,C} \propto \mathcal{N}^2$ grows, and the particle experience four phases in order (a) \rightarrow (b) \rightarrow (c) \rightarrow (d). (a) At ion-electron plasma phase, most of the charge is carried by plasma species and the charge state of the dust is governed by plasma absorption. (b) At ion-dust plasma phase, the current balances are same as it was in ion-electron plasma phase, but now the negative charge carrier is cationic smaller dust. (c) At charge-up phase, anionic larger dust has sufficient charge to cut off J_{A,e^-} . (d) At dust phase, most of the charge is carried by dust species and the collisional charging current $J_{A,C}$ balance with neutralization current $J_{C,A}^{(n)}$.

This leads to the following hierarchy of the current amplitude:

$$\begin{aligned} J_{e,i} &\simeq J_{i,C} \simeq J_{C,e} \propto \mathcal{N}^0 \\ &\gg J_{i,A} \simeq J_{A,e} \\ &\gg J_{A,C}. \end{aligned} \quad (2.58)$$

The amount of current for path (2.56) is constrained by edge $e^- \rightarrow i^+$; since I have assumed that ζ and n_g is independent of \mathcal{N} , so is $J_{e,i}$.

From charge neutrality (2.28), $Q_e = Q_i$ and therefore $n_e = n_i$. So equation $J_{i,C} \simeq J_{C,e}$ is satisfied by setting, in equations (2.20) and (2.22),

$$\sigma_{cou}(q_C, e)v_i = \sigma_{cou}(q_C, -e)v_e, \quad (2.59)$$

$$\frac{\sigma_{cou}(q_C, e)}{\sigma_{cou}(q_C, -e)} \simeq \frac{v_e}{v_i} \propto \mathcal{N}^0. \quad (2.60)$$

Equation (2.60) tells us that $\sigma_{cou}(q_C, e)/\sigma_{cou}(q_C, -e)$ is independent of \mathcal{N} . This means $q_C \propto \mathcal{N}^0$ because the only \mathcal{N} -dependent term in σ_{cou} is q_C . By definition of dust number density factor \mathcal{N} , $n_C \propto \mathcal{N}^1$, so $Q_C \propto \mathcal{N}^1$.

By similar argument starting from $J_{i,A} \simeq J_{A,e}$ one can deduce $Q_A \propto \mathcal{N}^1$.

Then, $J_{i,C} \propto \mathcal{N}^0$ and $\simeq J_{C,e} \propto \mathcal{N}^0$ leads to $n_i, n_e \propto \mathcal{N}^{-1}$. And from $q_i, q_e \propto \mathcal{N}^0$ one can deduce $Q_i, Q_e \propto \mathcal{N}^{-1}$.

In this phase, ions and electrons are the major carriers of positive and negative charge. Equation (2.60) also tells us that $\sigma_{cou}(q_C, e)/\sigma_{cou}(q_C, -e) \simeq v_e/v_i \gg 1$. This is interpreted as follows: Since thermal velocity of electron is much faster than that of molecular ions, electron is more rapidly absorbed to neutral dust than ions. Therefore dust continues to acquire negative charge, until its negative charge is enough to repulse most of the electrons inflow to attain a current equilibrium. Both cationic and anionic dust are forced to charge negative to hold back the overwhelming electron absorption.

To summarize,

$$Q_i \propto \mathcal{N}^{-1}, Q_e \propto \mathcal{N}^{-1}, Q_A \propto \mathcal{N}^{+1}, Q_C \propto \mathcal{N}^{+1}. \quad (2.61)$$

Ion-dust Plasma Phase

The system enters ion-dust plasma phase when the negative charge in dust Q_C become comparable to that in plasma Q_e . Charge neutrality (2.28) requires free electrons to decrease. So the Coulomb barrier of dust species become weaker until Coulomb cross section approximates geometric cross section $\sigma_{cou}(q_C, e) \simeq \sigma_{cou}(q_C, i) \simeq \pi a_C^2 \propto \mathcal{N}^0$ where electrons and ions are equally absorbed to the dust.

In ion-dust plasma phase (Figure 2.7 (b)), the dominant path is still

$$e^- \rightarrow i^+ \rightarrow C \rightarrow e^-, \quad (2.62)$$

and the next-dominant path is still

$$i^+ \rightarrow A \rightarrow e^-, \quad (2.63)$$

and the same current hierarchy holds:

$$\begin{aligned} J_{e,i} &\simeq J_{i,C} \simeq J_{C,e} \propto \mathcal{N}^0 \\ &\gg J_{i,A} \simeq J_{A,e} \\ &\gg J_{A,C}. \end{aligned} \quad (2.64)$$

However, now that $\sigma_{cou}(q_C, e) \simeq \sigma_{cou}(q_C, i)$, equation $J_{i,C} \simeq J_{C,e}$ is satisfied by setting, in equations (2.20) and (2.22),

$$n_i v_i = n_e v_e, \quad (2.65)$$

$$\frac{n_i}{n_e} \simeq \frac{v_e}{v_i} \propto \mathcal{N}^0. \quad (2.66)$$

So the ratio n_i/n_e is kept constant to $v_e/v_i = 6.1 \times 10^1$. Still, in order to have $J_{i,C} \propto \mathcal{N}^0$ and $\simeq J_{C,e} \propto \mathcal{N}^0$ it is necessary that $n_i, n_e \propto \mathcal{N}^{-1}$. And since $q_i, q_e \propto \mathcal{N}^0, Q_i, Q_e \propto \mathcal{N}^{-1}$.

In this phase the cationic dust carry most of the negative charge while ions carry most of the positive charge of the system. Therefore, the charge neutrality equation (2.28) is dominated by these two components, and $Q_C \propto Q_i \propto \mathcal{N}^{-1}$.

In this phase anionic dust also feels the same environment as cationic dust, so $Q_A \propto \mathcal{N}^{-1}$. However as \mathcal{N} approaches to (c)charge-up phase, dust-dust collisional charge separation $J_{A,C}$ gradually comes into play and Q_A increases. Therefore in Figure 2.6 the power law $Q_A \propto \mathcal{N}^{-1}$ is present only at the beginning of (b)ion-dust plasma phase.

To summarize,

$$Q_i \propto \mathcal{N}^{-1}, Q_e \propto \mathcal{N}^{-1}, Q_A \propto \mathcal{N}^{-1}, Q_C \propto \mathcal{N}^{-1}. \quad (2.67)$$

In ion-electron plasma phase and ion-dust plasma phase the dust-dust collisional charging is ineffective. Therefore the existence of the two phases have been mentioned in previous literature that did not take dust-dust collisional charging into account (see Okuzumi (2009) and references therein.)

Charge-up Phase

The system enters (c)charge-up phase when $J_{A,C}$ becomes larger than $J_{A,e}$. Now anionic dust has their own negative charge supply from dust-dust collision, their negative charge grow quickly, and $\sigma_{cou}(q_A, -e)$ become rapidly small. At this point, the circuit switches one of its current path.

In charge-up phase (Figure 2.7 (c)), the dominant path is still

$$e^- \rightarrow i^+ \rightarrow C \rightarrow e^-, \quad (2.68)$$

but the next-dominant path is

$$i^+ \rightarrow A \rightarrow C. \quad (2.69)$$

The amount of current for path (2.68) is constrained by edge $e^- \rightarrow i^+$; since I have assumed that ζ and n_g is independent of \mathcal{N} , so is $J_{e,i}$. The amount of current for path (2.69) is

constrained by edge $A \rightarrow C$ (2.17); since I have also assumed that $\Delta q_{A,C}$ is independent of \mathcal{N} , $J_{A,C} \propto \mathcal{N}^2$.

The above conditions lead to the following hierarchy:

$$\begin{aligned} J_{e,i} &\simeq J_{i,C} \simeq J_{C,e} \propto \mathcal{N}^0 \\ \gg J_{i,A} &\simeq J_{A,C} \propto \mathcal{N}^2 \\ \gg J_{A,e}. \end{aligned} \quad (2.70)$$

The path (2.68) is as same in ion-dust plasma phase, leading to $Q_i, Q_e \propto \mathcal{N}^{-1}$, and charge neutrality requires $Q_C \propto \mathcal{N}^{-1}$.

In dust charge-up phase, however, anionic dust has so much charge that electrostatic potential for electron and ion at the surface of larger dust is larger than their thermal energy; this is $qq'a^{-1} \gg k_B T$ limit of the Coulomb cross section (2.31), (2.31). Thus $\sigma_{cou}(q_A, -e) \rightarrow 0$ and $\sigma_{cou}(q_A, e) \propto q_A$ in (2.19). Substituting $n_i \propto \mathcal{N}^{-1}$ and $n_A \propto \mathcal{N}^1$ into $J_{i,A} \propto \mathcal{N}^2$ leads to $q_A \propto \mathcal{N}^2$ and $Q_A \propto \mathcal{N}^3$.

To summarize,

$$Q_i \propto \mathcal{N}^{-1}, Q_e \propto \mathcal{N}^{-1}, Q_A \propto \mathcal{N}^{+3}, Q_C \propto \mathcal{N}^{-1}. \quad (2.71)$$

Dust Phase

The system enters (d)dust phase when $J_{A,C}$ becomes larger than $J_{i,C}$. Now the charge states of both anionic and cationic dust is governed by dust-dust collision, and the plasma component is sub-dominant to the dust.

In dust phase (Figure 2.7 (d)), the dominant path is

$$A \rightarrow C \rightarrow A, \quad (2.72)$$

the dust-dust collision is now short-circuiting. The next-dominant path is

$$C \rightarrow e^- \rightarrow i^+ \rightarrow A. \quad (2.73)$$

The amount of current for path (2.72) is constrained by edge $A \rightarrow C$ (2.17). And since I have assumed that $\Delta q_{A,C}$ is independent of \mathcal{N} , $J_{A,C} \propto \mathcal{N}^2$.

In the same manner, the amount of current for path (2.73) is constrained by edge $e^- \rightarrow i^+$. And since I have assumed that ζ and n_g is independent of \mathcal{N} , so is $J_{e,i}$.

The above conditions lead to the following hierarchy:

$$\begin{aligned} J_{A,C} &\simeq J_{C,A}^{(n)} \propto \mathcal{N}^2 \\ \gg J_{C,e} &\simeq J_{e,i} \simeq J_{i,A} \propto \mathcal{N}^0 \\ \gg J_{A,e}. \end{aligned} \quad (2.74)$$

Equation $J_{A,C} \simeq J_{C,A}^{(n)}$ (2.74) requires $\Delta q_{A,C} \sigma_{A,C} = q_C \sigma_{A,C}^{(n)}$. Therefore only \mathcal{N} dependent term q_C must satisfy $q_C \propto \mathcal{N}^0$, leading to $Q_C \propto \mathcal{N}^1$. Charge neutrality leads to $Q_A \propto \mathcal{N}^1$.

The path (2.73) gives us $Q_i, Q_e \propto \mathcal{N}^{-1}$, same as in ion-dust plasma phase and in dust charge-up phase.

At the boundary of (c)charge-up phase and (d)dust phase there is a jump of dust charge. This is because when \mathcal{N} cross the boundary dust charge grows until dust-dust collisional neutralization can compensate dust-dust charge separation.

To summarize,

$$Q_i \propto \mathcal{N}^{-1}, Q_e \propto \mathcal{N}^{-1}, Q_A \propto \mathcal{N}^{+1}, Q_C \propto \mathcal{N}^{+1}. \quad (2.75)$$

Summary of the Section

In this section I have studied plasma with charge-separating ice dust. I have shown that as dust number density \mathcal{N} increase, the charge density distribution experience four phases: (a)ion-electron plasma phase, (b)ion-dust plasma phase, (c)charge-up phase and (d)dust phase. The former two phases are studied in detail by Okuzumi (2009), while the latter two phases are unique results of taking dust-dust collision into consideration.

2.3 Lightning due to Dust Charge

2.3.1 Critical Dust Number Density for Lightning

In this section I derive the strength of electric field generated by the relative motion of the large and small dust, and set conditions for macroscopic electric discharge events, or lightning.

Lightning occurs when the maximum electric field in the plasma comoving frame E' exceeds the critical value E_{crit} . The critical electric field E_{crit} is determined by the condition that an electron accelerated by the field has kinetic energy large enough to ionize a neutral gas molecule. Let l_{mfp} be the mean free path for electron. Then an electron accelerated in electric field of strength E receive the energy of order $e E l_{\text{mfp}}$. The ionization potentials ΔW_{ion} for H, H₂, and He molecules are 13.6 eV, 15.4 eV, and 24.6 eV respectively (Duley & Williams, 1984). I use $\Delta W_{\text{ion}} = 15.4$ eV in this work. Therefore the critical value E_{crit} of electric field for the lightning satisfies:

$$e E_{\text{crit}} l_{\text{mfp}} = \Delta W_{\text{ion}}, \quad (2.76)$$

$$E_{\text{crit}} = \frac{\Delta W_{\text{ion}}}{e l_{\text{mfp}}}. \quad (2.77)$$

Next I derive the value of E' . When the differential motion between the oppositely charged dust species continues much longer than the plasma Debye length, it can be interpreted as current carried by the dust j_D generating electrostatic field, and the plasma counter-current j_p is induced in the neutralizing direction. I approximate that j_p is carried by electrons, and neglect current carried by positive ions because it is at most the same order as that by electrons. Moreover, even if positive ions are accelerated to ΔW_{ion} and ionize other molecules, they increase the electron number density only linearly, not exponentially.

The dust current j_D is estimated simply, by the product of dust charge density Q_L and macroscopic motion u_L , as:

$$j_D = Q_L u_L. \quad (2.78)$$

On the other hand the particle current j_p is determined by the Ohm's law:

$$j_p = \nu E', \quad (2.79)$$

where ν is the electric conductivity,

$$\nu = \frac{n_e l_{\text{mfp}} e^2}{m_e v_e}. \quad (2.80)$$

E' is determined at the equilibrium of these two currents j_D and j_p :

$$j_D + j_p = 0. \quad (2.81)$$

By substituting Equations (2.78), (2.79), and (2.80) into Equation (2.81),

$$E' = -\frac{m_e v_e Q_L u_L}{n_e l_{\text{mfp}} e^2}. \quad (2.82)$$

Now that both E' and E_{crit} are known, the condition for electric discharge is

$$|E'| \geq E_{\text{crit}}. \quad (2.83)$$

Substituting (2.77) and (2.82) into (2.83) gives the following form of the condition for electric discharge:

$$\left| \frac{Q_L}{Q_e} \right| \geq \frac{\Delta W_{\text{ion}}}{m_e v_e |u_L|}. \quad (2.84)$$

Within the parameter range of interest, the dependence of the left hand side of (2.84) on \mathcal{N} is as follows. As \mathcal{N} increase, the left hand side first keeps values much smaller than the right hand side and then it monotonically increases (cf. Figure 2.6). Thus there is a unique value of \mathcal{N} at which the equality for (2.84) holds. I denote this value by symbol $\mathcal{N}_{\text{crit}}$, the critical dust number density at which lightning takes place. Note that the condition doesn't depend on the detail of the electron stopping processes, because l_{mfp} can be eliminated from the condition.

2.3.2 Numerical Simulations for Uniform-box Lightning Estimation

I now briefly explain the second numerical experiments, where I varied the set of input parameters, r_s , r_L , D_s , and D_L , and for each set of input parameters I calculated the critical dust number density $\mathcal{N}_{\text{crit}}$ at which the lightning takes place. The numerical results strongly suggest that the parameter space (r_s, r_L, D_s, D_L) is subdivided into several regions, at each of which $\mathcal{N}_{\text{crit}}$ is a simple analytic function of parameters (r_s, r_L, D_s, D_L) .

The parameter ranges are

$$1.0 \times 10^{-4} \text{ cm} < r_s < 1.0 \times 10^2 \text{ cm}, \quad (2.85)$$

$$1.0 \text{ cm} < r_L < 1.0 \times 10^3 \text{ cm}, \quad (2.86)$$

$$2.0 < D_s < 3.0, \quad (2.87)$$

$$2.0 < D_L < 3.0, \quad (2.88)$$

with additional constraints

$$r_s < r_L, \quad (2.89)$$

$$D_s < D_L, \quad (2.90)$$

$$1.0 < \mathcal{N} < 1.0 \times 10^6. \quad (2.91)$$

Constraint (2.89) requires that the smaller dust is smaller than the larger dust. Constraint (2.90) comes from empirical fact that larger dust aggregates have experienced more compaction, and have higher fractal dimension (Suyama et al., 2008; Wada et al., 2008). Constraint (2.91) is cutoff value of our computation.

I visualize the four-dimensional field $\mathcal{N}_{\text{crit}}(r_s, r_L, D_s, D_L)$ in the figures 2.8-2.12, by choosing some representative points and presenting several 2-dimensional sections that passes the point. As the mass, the radius, and the fractal dimension of a dust is related by equation (2.30), there is freedom of choosing the direction of 2-dimensional section. I choose to keep m_I constant when varying D_I (the dust puff up with constant mass); I keep D_I constant when varying r_I (the dust mass increase with constant fractal dimension).

First, Figure 2.8 shows the ‘fluffy dust’ cross sections, where the representative dust are $r_s = 1.0 \times 10^{-2}$ cm, $r_L = 1.0 \times 10^2$ cm, $m_s = 3.9 \times 10^{-9}$ g, $m_L = 1.5 \times 10^2$ g, $D_s = 2.0$, and $D_L = 2.4$. The critical number density is $\mathcal{N}_{\text{crit}} = 7.37 \times 10^1$ for this representative parameter.

The second set of Figure 2.9 uses the ‘hard dust’ cross sections, where $r_s = 1.0 \times 10^{-4}$ cm, $r_L = 1.0$ cm, $m_s = 1.9 \times 10^{-12}$ g, $m_L = 3.9$ g, $D_s = 2.7$, and $D_L = 3.0$. The critical number density is $\mathcal{N}_{\text{crit}} = 3.01 \times 10^2$ for this representative parameter.

The third set of Figure 2.10, is the $\mathcal{N}_{\text{crit}}$ averaged over the parameters that do not appear in the axes, to show the tendency of overall dependence on the parameters, and to demonstrate the precision of the analytic formulae.

The fourth set of Figure 2.11 uses the same representative dust as in Figure 2.8, but is the result of another simulations, where it is pessimistically assumed that the charge exchange is four orders of magnitude inefficient ($\mathcal{N}_{ch} = 1.0 \times 10^{-5}$ instead of $\mathcal{N}_{ch} = 1.0 \times 10^{-1}$). Even though, the number density $\mathcal{N}_{\text{crit}}$ required for lightning has raised only by two order of one magnitude. The critical number density is $\mathcal{N}_{\text{crit}} = 6.59 \times 10^3$ for the representative parameter.

The fifth set of Figure 2.12 shows the averaged $\mathcal{N}_{\text{crit}}$ for the pessimistic case $\mathcal{N}_{ch} = 1.0 \times 10^{-5}$. I later examine the accuracy of our formulae by fitting Figure 2.12 with the formulae using correction factors determined by Figure 2.10 data.

2.3.3 Analytic Formulae for Lightning Conditions

In this section I derive the analytic form of $\mathcal{N}_{\text{crit}}$ and lightning conditions. Numerical results obtained in §2.3.2 are of great help in deriving these analytic formulae. I show at the end of §2.3.3 that the analytic formulae can fit 364325 numerically-obtained points distributed among six decades with 21 per cent precision. Moreover, the formulae “predicts” the results of another simulation with 59 per cent precision, where charge exchange is 10^4 times inefficient. These agreements are good evidences for correctness of both numerical and analytic results.

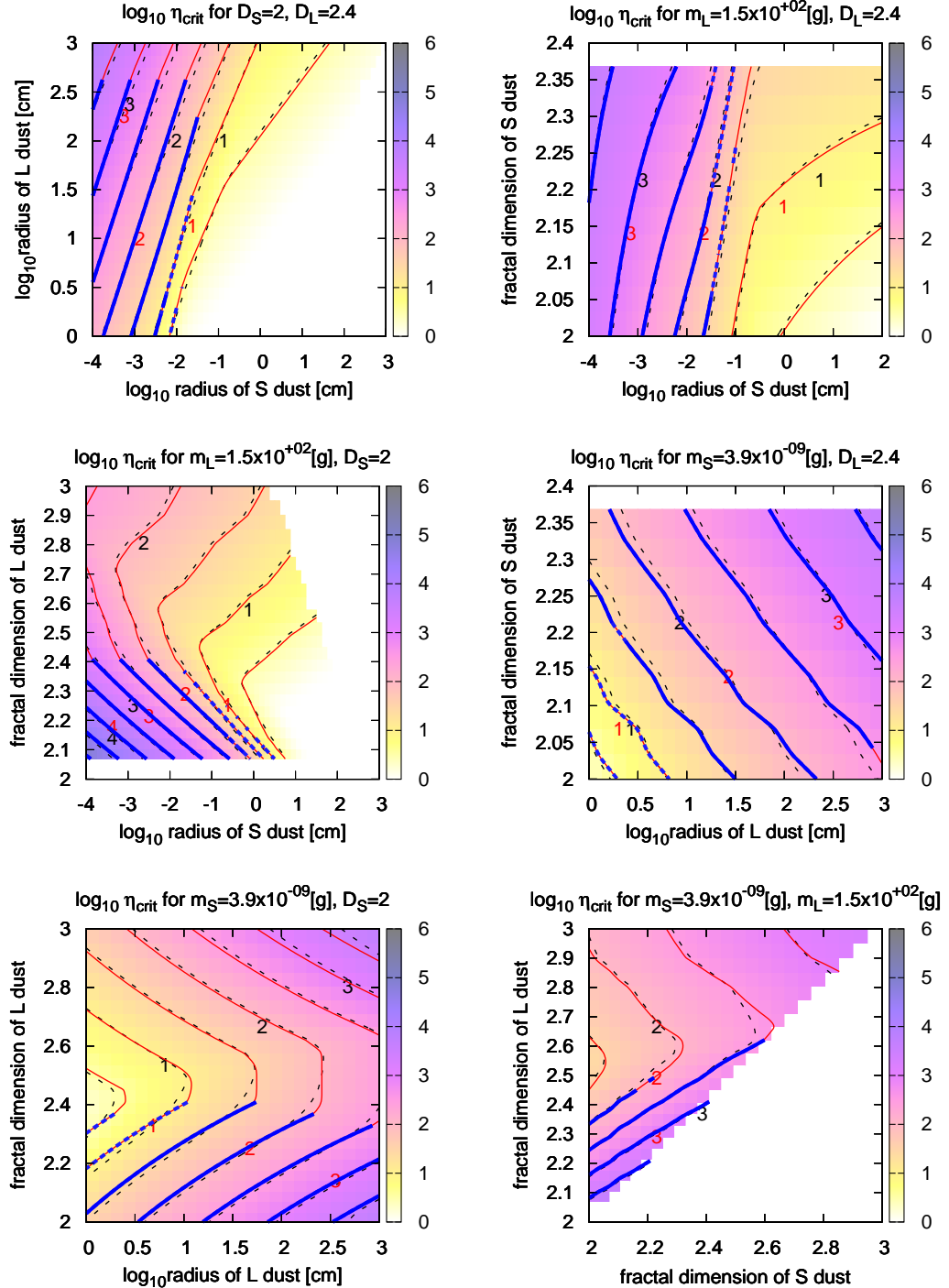


Figure 2.8. Value of η_{crit} as function of dust radius r_s, r_L and fractal dimension D_s, D_L . The base values are $r_s = 1.0 \times 10^{-2}$ cm, $r_L = 1.0 \times 10^2$ cm, $m_s = 3.9 \times 10^{-9}$ g, $m_L = 1.5 \times 10^2$ g, $D_s = 2.0$, and $D_L = 2.368$. m_i is kept constant when varying D_i ; D_i is kept constant when varying r_i . Numerical results are in color maps and black dashed contours; analytic values in colored solid contours (cf. §2.3.3 for the details of the plots.)

These results were first presented in Muranushi (2010).

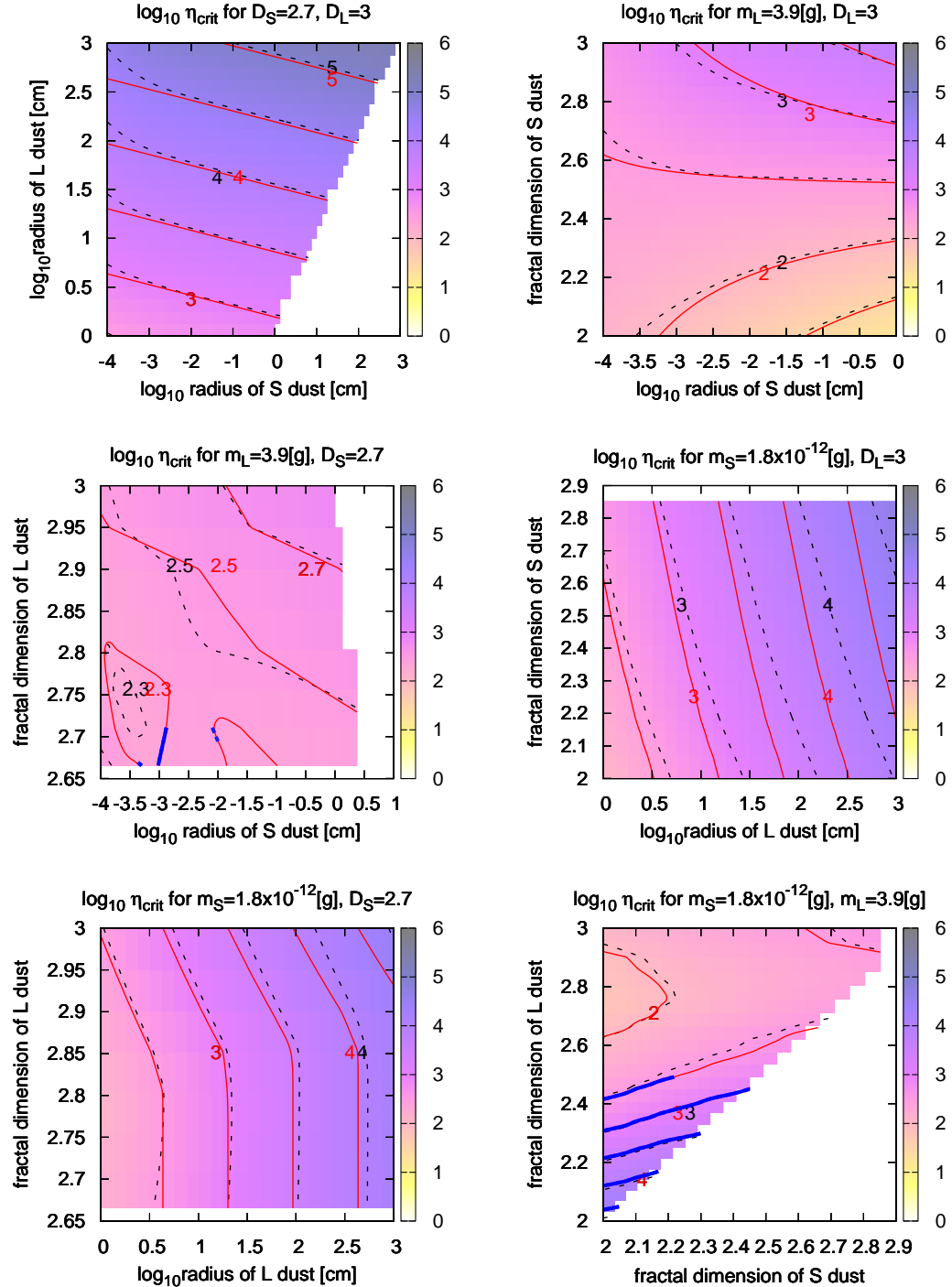


Figure 2.9. Value of η_{crit} as function of dust radius r_s, r_L and fractal dimension D_s, D_L . The base values are $r_s = 1.0 \times 10^{-4} \text{ cm}$, $r_L = 1.0 \text{ cm}$, $m_s = 1.9 \times 10^{-12} \text{ g}$, $m_L = 3.9 \text{ g}$, $D_s = 2.665$, and $D_L = 3.0$. m_1 is kept constant when varying D_1 ; D_1 is kept constant when varying r_1 . Numerical results are in color maps and black dashed contours; analytic values in colored solid contours (cf. §2.3.3 for the details of the plots.)

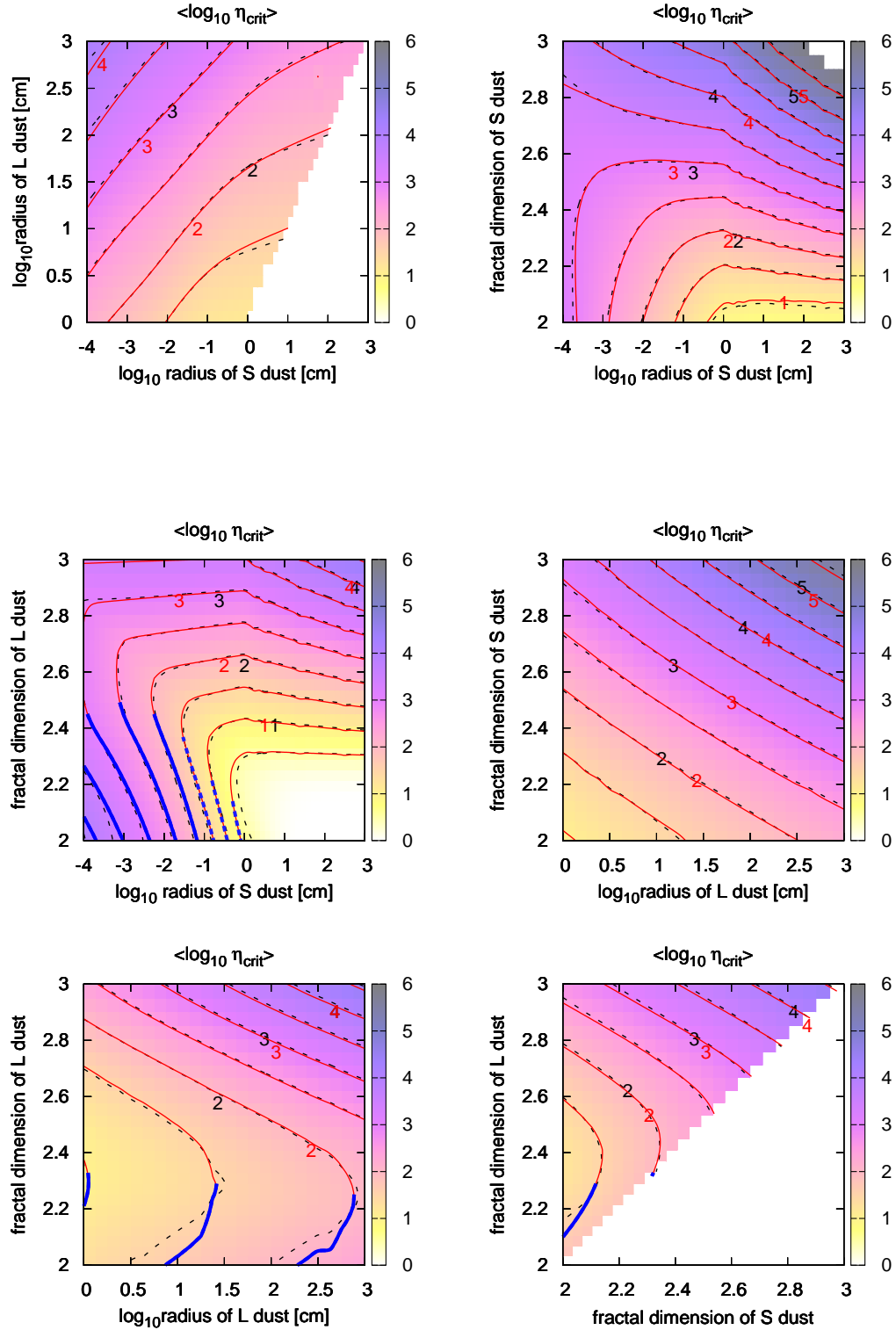


Figure 2.10. Value of η_{crit} as function of r_s , r_L , D_s , and D_L . Parameters do not appear in x-axis or y-axis are uniformly averaged over the parameter range accepted in this thesis. Numerical results are in color maps and black dashed contours; analytic values in colored solid contours (cf. §2.3.3 for the details of the plots.)

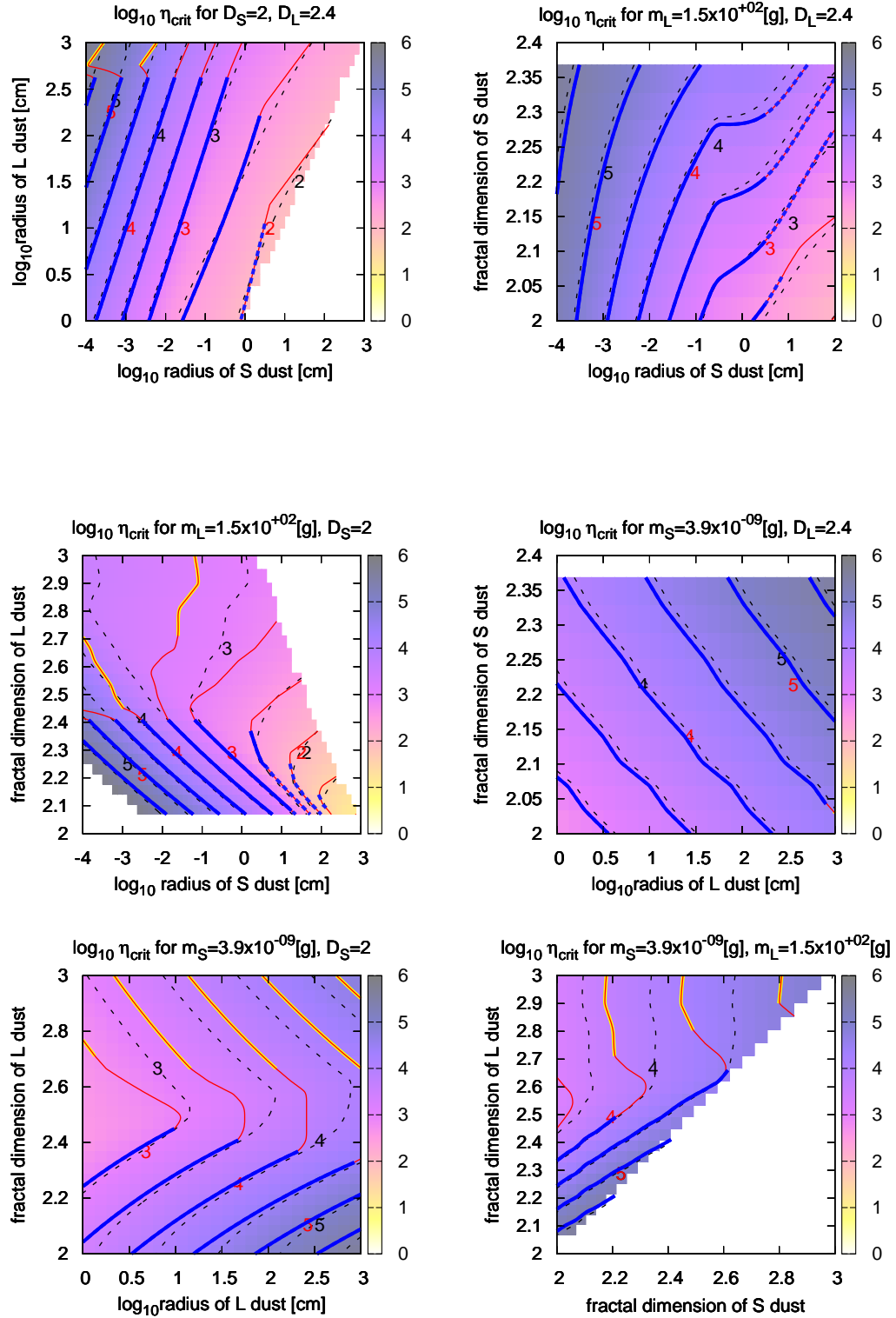


Figure 2.11. In the above plots, all the parameters but the charge separation efficiency is same as that of Figure 2.8, while the the charge separation efficiency $\eta_{ch} = 1.0 \times 10^{-5}$ for this figure. Numerical results are in color maps and black dashed contours; analytic values in colored solid contours (cf. §2.3.3 for the details of the plots.)

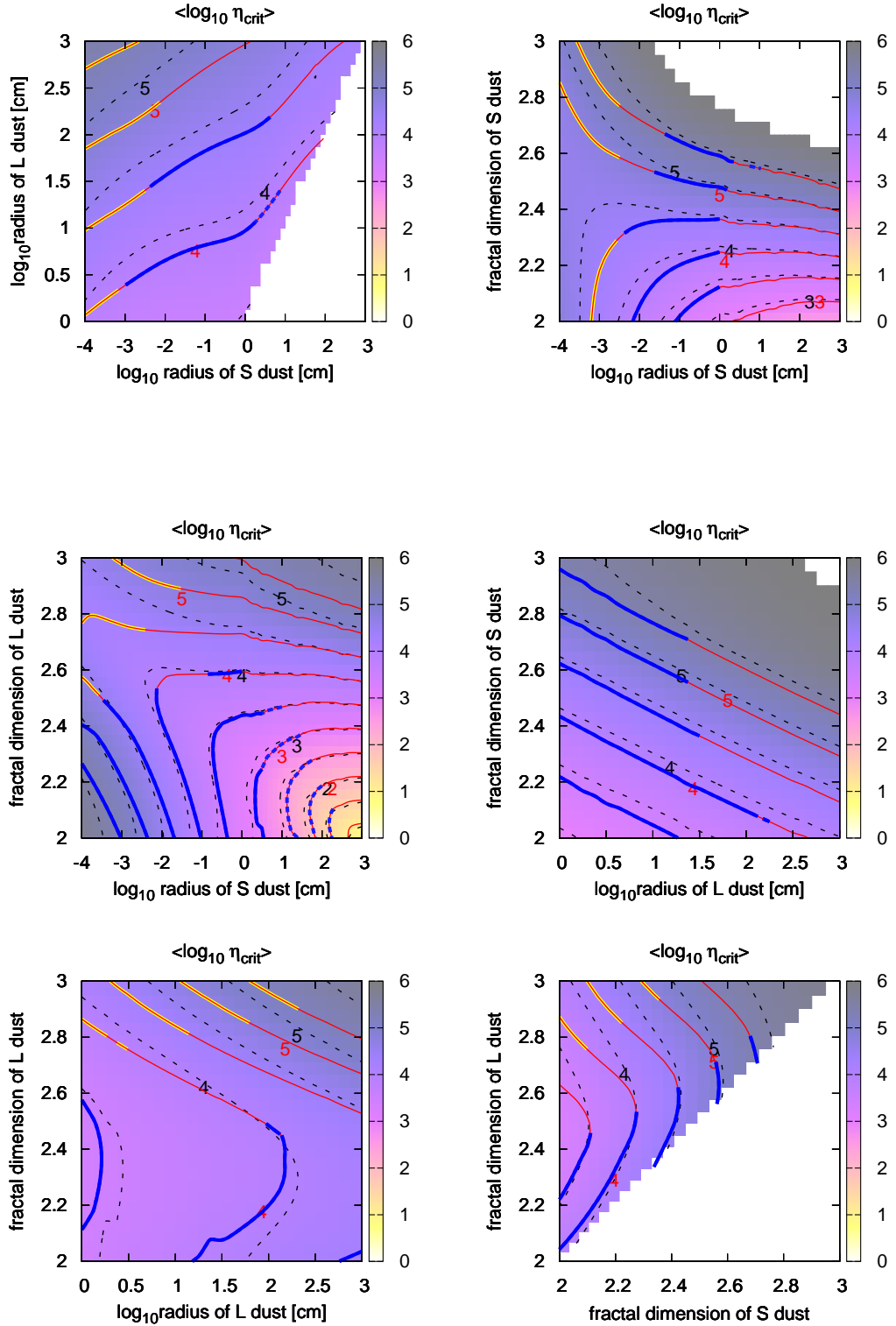


Figure 2.12. Value of η_{crit} as function of r_s , r_L , D_s , and D_L . Parameters do not appear in x-axis or y-axis are uniformly averaged over the parameter range as in Figure 2.10, and I assume $\eta_{ch} = 1.0 \times 10^{-5}$ as in Figure 2.11. Numerical results are in color maps and black dashed contours; analytic values in colored solid contours (cf. §2.3.3 for the details of the plots.)

I made plots like Figure 2.6 for many points within our parameter space, and found that $\mathcal{N} = \mathcal{N}_{\text{crit}}$ is met at the boundary of (c)charge-up phase and (d)dust phase in most cases, and sometimes in (d)dust phase or (c)charge-up phase. Therefore I derive analytic form of \mathcal{N} corresponding to these three cases in §2.3.3 to §2.3.3, and combine them in §2.3.3.

Analytic Formulae for Charge-up Phase / Dust Phase Boundary

I first calculate $\mathcal{N}^{(cd)}$, the value of \mathcal{N} corresponding to the (c)charge-up phase / (d)dust phase boundary.

The boundary satisfies $J_{L,S} = J_{i,S}$ (Table 2.3). I use the approximations in (c)charge-up phase to find the break point of the phase. Then

$$J_{L,S} \simeq 2\pi r_S r_L \Delta q_{A,C} n_S n_L \Delta v_{L,S} \quad (2.92)$$

$$J_{S,i} \simeq -Q_i n_S \pi r_S^2 \sigma_{S,i} v_i. \quad (2.93)$$

Here I have ignored the neutralization current $J_{L,S}^{(n)}$, used the approximations $\sigma_{L,S} = \pi r_L^2$, $\sigma_{S,i} = \pi r_S^2$ (geometric cross sections) and $\sigma_{L,i} = \pi r_L^2 |eQ_L| (r_L k_B T n_L)^{-1}$ ($qq'a^{-1} \gg k_B T$ limit of Coulomb cross section (2.32)).

In dust charge-up phase, both ions and electrons are mainly absorbed by smaller dust, so from (2.53) and (2.54) I have

$$Q_i = \frac{e\zeta n_g}{n_S \sigma_{S,i} v_i} \quad (2.94)$$

$$Q_e = \frac{-e\zeta n_g}{n_S \sigma_{S,e} v_e} \quad (2.95)$$

and the absorption cross sections are geometric : $\sigma_{S,i} = \sigma_{S,e} = \pi r_S^2$.

By substituting (2.94) into (2.93)

$$J_{S,i} = e\zeta n_g = J_{e,i} \quad (2.96)$$

cf. Figure 2.6(c) and in equation (2.70).

The argument led to a simple result, that $\mathcal{N}_{\text{crit}}$ satisfies

$$J_{L,S} = J_{e,i}. \quad (2.97)$$

Substituting equations (2.92), (2.96), together with $n_S = \mathcal{N}^{(cd)} n_S^\bowtie$ and $n_L = \mathcal{N}^{(cd)} n_L^\bowtie$ into equation (2.97) and solving for dust number density \mathcal{N} ,

$$\mathcal{N}^{(cd)} = \left(\frac{\alpha^{(cd)}}{2\pi} \frac{e}{\Delta q_{A,C}} \frac{n_g}{n_S^\bowtie n_L^\bowtie r_S r_L} \frac{\zeta}{\Delta v_{L,S}} \right)^{\frac{1}{2}}. \quad (2.98)$$

Here I introduce a non-dimensional correction factor $\alpha^{(cd)}$, a constant that does not depend on r_S, r_L, D_S, D_L . The factor is needed to compensate the error arising from using the formulae in (c)charge-up phase to find the break point of itself. The actual value for $\alpha^{(cd)}$ is in §2.3.3.

Analytic Formula for $\mathcal{N}_{\text{crit}}$ in Dust Phase

Next, I derive the analytic formula of the critical density $\mathcal{N}_{\text{crit}}^{(d)}$, where the condition for electric discharge (2.84) is met in (d)dust phase (cf. §2.2.8, Figure 2.7(d)).

Imposing $J_{L,S} = 0$ in (2.45), and by approximating the charge neutrality (2.55) with $Q_S + Q_L = 0$,

$$Q_S = |Q_L| = \Delta q_{A,C} n_S \frac{2r_S}{r_L} \quad (2.99)$$

By approximating equation (2.54) with $J_{S,e} + J_{i,e} = 0$,

$$Q_e = -\frac{en_g\zeta}{\pi n_S r_S^2 (1+\chi) v_e} \quad (2.100)$$

$$\text{where } 1+\chi = 1 + \frac{Q_S e}{n_S r_S k_B T}; \quad (2.101)$$

the factor $(1+\chi)$ comes from the Coulomb cross section (2.32).

Substituting Q_L and Q_e , the equality for the lightning condition (2.84) becomes

$$\frac{2\pi\Delta q_{A,C}}{e} \frac{n_S^2 r_S^3 (1+\chi)}{n_g r_L} \frac{v_e}{\zeta} = \frac{\Delta W_{\text{ion}}}{m_e v_e u_L} \quad (2.102)$$

Substituting $n_S = \mathcal{N}_{\text{crit}}^{(d)} n_S^{\bowtie}$ and solving for $\mathcal{N}_{\text{crit}}^{(d)}$ gives the following analytic formula for $\mathcal{N}_{\text{crit}}^{(d)}$:

$$\mathcal{N}_{\text{crit}}^{(d)} = \left(\frac{\alpha^{(d)}}{2\pi(1+\chi)} \frac{e}{\Delta q_{A,C}} \frac{n_g r_L}{n_S^{\bowtie 2} r_S^3} \frac{\zeta}{u_L} \frac{\Delta W_{\text{ion}}}{k_B T} \right)^{\frac{1}{2}}. \quad (2.103)$$

Here I introduce another non-dimensional correction constant $\alpha^{(d)}$ as in §2.3.3.

Analytic Formula for $\mathcal{N}_{\text{crit}}$ in Charge-up Phase

Finally, I derive the analytic formula of the critical density $\mathcal{N}_{\text{crit}}^{(c)}$, where the condition for electric discharge (2.84) is met in (c)charge-up phase (cf. §2.2.8, Figure 2.7(c)).

By approximating equations (2.53) and (2.55) with $J_{S,i} = J_{i,e}$ and $Q_S + Q_i = 0$,

$$Q_i = -Q_S = \frac{en_g\zeta}{\pi n_S r_S^2 v_i} \quad (2.104)$$

Ignoring $J_{L,e}$ in equation (2.51) and the second term in equation (2.45) gives

$$\frac{2r_S}{r_L} \Delta q_{A,C} n_S n_L \Delta v_{L,S} \pi r_L^2 - Q_i n_L \sigma_{L,i} v_i = 0, \quad (2.105)$$

$$\text{where } \sigma_{L,i} = \frac{Q_L e}{n_L r_L l_B T} \pi r_L^2, \quad (2.106)$$

here the $qq'a^{-1} \gg k_B T$ limit of Coulomb cross section (2.32) is used.

Solving this for Q_L gives

$$|Q_L| = \frac{2\Delta q_{A,C}}{e^2} \frac{n_s^2 n_L r_s^3}{n_g} \frac{\Delta v_{L,S} k_B T}{\zeta} \quad (2.107)$$

And from equation (2.54) one can derive

$$Q_e = -\frac{en_g \zeta}{\pi n_s r_s^2 v_e} \quad (2.108)$$

Substituting these Q_L and Q_e to the equality for the lightning condition (2.84), and replacing $n_s = \mathcal{N}_{\text{crit}}^{(c)} n_s^{\bowtie}$ and $n_L = \mathcal{N}_{\text{crit}}^{(c)} n_L^{\bowtie}$, and solving for $\mathcal{N}_{\text{crit}}^{(c)}$ gives the following analytic formula for $\mathcal{N}_{\text{crit}}^{(c)}$:

$$\mathcal{N}_{\text{crit}}^{(c)} = \left(\frac{\alpha^{(c)}}{2\pi} \frac{e^3}{\Delta q_{A,C}} \frac{n_g^2}{n_s^{\bowtie} n_L^{\bowtie} r_s^5} \frac{\zeta^2}{\Delta v_{L,S} u_L} \frac{\Delta W_{\text{ion}}}{(k_B T)^2} \right)^{\frac{1}{4}} \quad (2.109)$$

I introduce a third non-dimensional correction constant $\alpha^{(c)}$ as I did in previous sections.

The Combined Analytic Formula for $\mathcal{N}_{\text{crit}}$

The critical number density $\mathcal{N}_{\text{crit}}$ is either one of $\mathcal{N}_{\text{crit}}^{(c)}$, $\mathcal{N}_{\text{crit}}^{(cd)}$, $\mathcal{N}_{\text{crit}}^{(d)}$. To choose the correct one, calculation of the phase boundary conditions (cf. Table 2.3) is required. Instead, I propose the following convenient scheme to choose the correct one:

$$\begin{aligned} \mathcal{N}_{\text{crit}} &= \mathcal{N}_{\text{crit}}^{(d)} && \text{if } \mathcal{N}_{\text{crit}}^{(d)} > \mathcal{N}_{\text{crit}}^{(cd)}, \\ &= \mathcal{N}_{\text{crit}}^{(cd)} && \text{if } \mathcal{N}_{\text{crit}}^{(c)} > \mathcal{N}_{\text{crit}}^{(cd)} > \mathcal{N}_{\text{crit}}^{(d)}, \\ &= \mathcal{N}_{\text{crit}}^{(c)} && \text{otherwise.} \end{aligned} \quad (2.110)$$

This scheme is based on the intuition that the (cd)phase boundary is included in both (c)charge-up phase and (d)dust phase. Therefore it is reasonable to assume that if $\mathcal{N}_{\text{crit}}^{(d)} > \mathcal{N}_{\text{crit}}^{(cd)}$, the number density $\mathcal{N}_{\text{crit}}^{(cd)}$ is not large enough to cause lightning, and that if $\mathcal{N}_{\text{crit}}^{(c)} < \mathcal{N}_{\text{crit}}^{(cd)}$, the number density $\mathcal{N}_{\text{crit}}^{(c)}$ is already large enough to cause lightning.

Now, without the correction, e.g. with $\alpha^{(c)} = \alpha^{(cd)} = \alpha^{(d)} = 1$, the analytic values for $\mathcal{N}_{\text{crit}}$ differs from the numerical values $\mathcal{N}_{\text{crit}}^{(\text{num})}$ calculated in §2.3.2, because of approximations used. Now I determine the values for $\alpha^{(c)}$, $\alpha^{(cd)}$, $\alpha^{(d)}$ by the condition that the following squared-error integral over the entire parameter ranges (2.85-2.91) is minimum:

$$\iiint dr_s dr_L dD_s dD_L (\log_{10} \mathcal{N}_{\text{crit}} - \log_{10} \mathcal{N}_{\text{crit}}^{(\text{num})})^2 \quad (2.111)$$

This gives $\alpha^{(c)} = 9.4 \times 10^{-1}$, $\alpha^{(cd)} = 3.3 \times 10^{-1}$, $\alpha^{(d)} = 8.5 \times 10^{-1}$. Taking these corrections into account, the values for $\mathcal{N}_{\text{crit}}^{(c)}$, $\mathcal{N}_{\text{crit}}^{(cd)}$, $\mathcal{N}_{\text{crit}}^{(d)}$ are as follows:

$$\begin{aligned} \mathcal{N}_{\text{crit}}^{(c)} = & 1.1 \times 10^3 \left(\frac{\Delta q_{A,C}}{6.2 \times 10^2 \text{ e}} \right)^{-\frac{1}{4}} \left(\frac{n_g}{4.7 \times 10^{13} \text{ cm}^{-3}} \right)^{\frac{1}{2}} \\ & \left(\frac{n_s^\bowtie}{8.8 \times 10^{-1} \text{ cm}^{-3}} \right)^{-\frac{3}{4}} \left(\frac{n_L^\bowtie}{4.0 \times 10^{-14} \text{ cm}^{-3}} \right)^{-\frac{1}{4}} \\ & \left(\frac{r_s}{1.0 \times 10^{-4} \text{ cm}} \right)^{-\frac{5}{4}} \\ & \left(\frac{\zeta}{1.0 \times 10^{-18} \text{ sec}^{-1}} \right)^{\frac{1}{2}} \\ & \left(\frac{\Delta v_{L,S}}{3.4 \times 10^3 \text{ cm sec}^{-1}} \right)^{-\frac{1}{4}} \left(\frac{u_L}{3.4 \times 10^3 \text{ cm sec}^{-1}} \right)^{-\frac{1}{4}} \\ & \left(\frac{\Delta W_{\text{ion}}}{15.4 \text{ eV}} \right)^{\frac{1}{2}} \left(\frac{T}{1.7 \times 10^2 \text{ K}} \right)^{-\frac{1}{2}}, \end{aligned} \quad (2.112)$$

$$\begin{aligned} \mathcal{N}^{(cd)} = & 3.3 \times 10^2 \left(\frac{\Delta q_{A,C}}{6.2 \times 10^2 \text{ e}} \right)^{-\frac{1}{2}} \left(\frac{n_g}{4.7 \times 10^{13} \text{ cm}^{-3}} \right)^{\frac{1}{2}} \\ & \left(\frac{n_s^\bowtie}{8.8 \times 10^{-1} \text{ cm}^{-3}} \right)^{-\frac{1}{2}} \left(\frac{n_L^\bowtie}{4.0 \times 10^{-14} \text{ cm}^{-3}} \right)^{-\frac{1}{2}} \\ & \left(\frac{r_s}{1.0 \times 10^{-4} \text{ cm}} \right)^{-\frac{1}{2}} \left(\frac{r_L}{1.0 \text{ cm}} \right)^{-\frac{1}{2}} \\ & \left(\frac{\zeta}{1.0 \times 10^{-18} \text{ sec}^{-1}} \right)^{\frac{1}{2}} \\ & \left(\frac{\Delta v_{L,S}}{3.4 \times 10^3 \text{ cm sec}^{-1}} \right)^{-\frac{1}{2}}, \end{aligned} \quad (2.113)$$

$$\begin{aligned} \mathcal{N}_{\text{crit}}^{(d)} = & 5.9 \times 10^1 \left(\frac{\Delta q_{A,C}}{6.2 \times 10^2 \text{ e}} \right)^{-\frac{1}{2}} \left(\frac{n_g}{4.7 \times 10^{13} \text{ cm}^{-3}} \right)^{\frac{1}{2}} \\ & \left(\frac{n_s^\bowtie}{8.8 \times 10^{-1} \text{ cm}^{-3}} \right)^{-1} \\ & \left(\frac{r_s}{1.0 \times 10^{-4} \text{ cm}} \right)^{-\frac{3}{2}} \left(\frac{r_L}{1.0 \text{ cm}} \right)^{\frac{1}{2}} \\ & \left(\frac{\zeta}{1.0 \times 10^{-18} \text{ sec}^{-1}} \right)^{\frac{1}{2}} \left(\frac{u_L}{3.4 \times 10^3 \text{ cm sec}^{-1}} \right)^{-\frac{1}{2}} \\ & \left(\frac{\Delta W_{\text{ion}}}{15.4 \text{ eV}} \right)^{\frac{1}{2}} \left(\frac{T}{1.7 \times 10^2 \text{ K}} \right)^{-\frac{1}{2}}. \end{aligned} \quad (2.114)$$

Note that $\Delta q_{A,C}$, n_s^\bowtie , and n_L^\bowtie also depends on dust parameters: r_s , r_L , D_s , and D_L . Using equation (2.39) and the \mathcal{N}_{ch} , σ_{ch} introduced in §2.2.5-I,

$$\Delta q_{A,C} = \mathcal{N}_{ch} \sigma_{ch} S_{\text{kiss}} \quad (2.115)$$

$$\begin{aligned} = & 6.2 \times 10^2 \text{ e} \cdot \frac{\mathcal{N}_{ch}}{0.1} \frac{\sigma_{ch}}{6.2 \times 10^9 \text{ e cm}^{-2}} \\ & \frac{\min(r_s^{3/2} r_L^{1/2}, r_m^{2-D_L} r_s^{5/2} r_L^{D_L-5/2})}{1.0 \times 10^{-6} \text{ cm}^2}. \end{aligned} \quad (2.116)$$

Using equations (2.6-2.12) and equation (2.30),

$$\begin{aligned} n_s^{\bowtie} &= 4.0 \times 10^2 \left(\frac{r_s}{r_m} \right)^{-D_S} \text{ cm}^{-3} \\ &\quad \left(\frac{r}{2.7 \text{ au}} \right)^{-11/4} \left(\frac{m_m}{3.9 \times 10^{-15} \text{ g}} \right)^{-1} \end{aligned} \quad (2.117)$$

$$\begin{aligned} n_L^{\bowtie} &= 4.0 \times 10^1 \left(\frac{r_L}{r_m} \right)^{-D_L} \text{ cm}^{-3} \\ &\quad \left(\frac{r}{2.7 \text{ au}} \right)^{-11/4} \left(\frac{m_m}{3.9 \times 10^{-15} \text{ g}} \right)^{-1}, \end{aligned} \quad (2.118)$$

and the monomer radius

$$r_m = 1.0 \times 10^{-5} \text{ cm}. \quad (2.119)$$

These analytic solutions (2.112-2.114) combined with the condition (2.110) are in excellent agreement with the numerical results. Quantitatively, the root-mean-square error is

$$\sqrt{\frac{\iiint dr_s dr_L dD_S dD_L (\log_{10} \mathcal{N}_{\text{crit}} - \log_{10} \mathcal{N}_{\text{crit}}^{(\text{num})})^2}{\iiint dr_s dr_L dD_S dD_L}} = 9.2 \times 10^{-2}. \quad (2.120)$$

Moreover, using the values of $\alpha^{(c)}$, $\alpha^{(cd)}$, $\alpha^{(d)}$ obtained only from the ‘normal’ run, the formulae (2.112-2.114) can fit the results of the ‘pessimistic’ simulations, where the charge exchange efficiency \mathcal{N}_{ch} is set to be 10^4 times smaller value, by a root-mean-square error of 2.6×10^{-1} . I also performed the simulations with smaller values of relative velocity $\Delta v_{L,S}$ and fit the results. The root-mean-square errors were 5.6×10^{-2} , 6.4×10^{-2} , 1.1×10^{-1} , for $\Delta v_{L,S} = u_L = 3.4 \times 10^2 \text{ cm s}^{-1}$, $3.4 \times 10^1 \text{ cm s}^{-1}$, 3.4 cm s^{-1} , respectively. These fits prove the predictability of our analytic formulae (2.110) and (2.112-2.114).

Summary of the Section

In this section I have studied a uniform-box model for protoplanetary disk lightning, first by numerical simulations and then fitting the results by analytic formulae. I have calculated the dust number density $\mathcal{N}_{\text{crit}}$ at which lightning strikes, as function of dust radius r_s , r_L and fractal dimension D_S , D_L numerically. Using the numerical results, I have derived the analytic formulae for $\mathcal{N}_{\text{crit}}$; equations (2.110), (2.112-2.114). Because the generated electrostatic field $E_{\max}(\eta)$ grows more rapidly than that estimated by Gibbard et al. (1997) in the newly found (c)charge-up phase and (d)dust phases, lightning in protoplanetary discs are possible with smaller dust number densities.

Chapter 3

Self Sustainment of Magnetorotational Instability

3.1 Magnetorotational Instability with nonlinear Ohm's law

3.1.1 Physical Motivation

Protoplanetary disks are the sites of planet formation. The disk turbulence greatly affects the mutual sticking of the planetesimals, their settlement to the disk midplane. The turbulence is the source of the angular momentum transport in the disk that causes gas accretion and migration of the planetesimal onto the central star. Thus understanding the evolution of the turbulence within protoplanetary disks is an essential step both in the studies of the disk evolution and the planet formation.

The magnetorotational instability (MRI) is considered to be the major source of turbulence in many types of accretion disks including protoplanetary disks (Balbus & Hawley (1998) and references therein). One of the distinct properties of the protoplanetary disks compared to other accretion disks is that the major parts of the protoplanetary disks are only weakly ionized, and hence the magnetic diffusivity affects the MRI (Sano et al. (1998); Fleming et al. (2000).) The low ionization degree is due to their low temperature and high number density of the dust component.

In protoplanetary disks, MRI and the dust components affect each other. The turbulence is one of the sources for the relative velocities of the colliding dust (Ormel & Cuzzi, 2007; Brauer et al., 2008), and contributes to both dust growth and disruption (Blum & Wurm, 2008; Wada et al., 2008; Güttsler et al., 2010; Wettlaufer, 2010). On the other hand, dust particles in protoplanetary disks are the major sites of charged particle recombination, and thereby influences the ionization degree of the disk (Sodha et al., 2009; Umebayashi & Nakano, 2009; Grach et al., 2010).

This chapter is based on the refereed journal article “*Interdependence of Electric Discharge and Magnetorotational Instability in Protoplanetary Disks*” (Muranushi et al., 2012). Reproduced by permission of the AAS.

The dead zone can occupy a large volume of a protoplanetary disk, especially in the presence of abundant small dust grains (Gammie, 1996; Sano et al., 2000; Ilgner & Nelson, 2006). However, various electric discharge mechanisms in protoplanetary disks have been proposed (Horanyi et al., 1995; Desch & Cuzzi, 2000; Muranushi, 2010). These may provide ionization degree higher than the values predicted by the dust-absorption equilibrium models, resulting in the increased MRI activity in the disk.

The electron avalanche process leads to an exponential growth in the number of conducting electrons that takes place when the kinetic energy of the electrons exceeds the ionization energy of a neutral gas molecule. The result is electrostatic breakdown, the lowering of the resistivity of the fluid and electric discharge, increase of the electric current through the fluid.

Moreover, a model in which the MRI itself provides sufficient ionization is proposed (Inutsuka & Sano, 2005). They have shown that the electric field typically generated by the protoplanetary disk turbulence is strong enough to drive the electrons away from the thermal Maxwell-Boltzmann distribution. Those energetic electrons contained in electric current cause the electric discharge and maintains the ionization degree high enough for the MRI to survive. They have also shown that the energy supply from the shearing motion is about 30 times larger than the energy required to maintain the sufficient number of electrons in the presence of standard dust grains.

However, they have studied only one-zone models with only one set of parameters, those of at 1 au of the disk. In this thesis, I extend Inutsuka & Sano (2005)'s model to a local, 3D simulations of protoplanetary disks and study the interaction of the MRI with the discharge ionization. I also apply the model to global models of protoplanetary disks and study where and when in the disk the self-sustainment of MRI takes place.

3.1.2 Numerical Setup

There are three diffusion terms in MHD; Ohmic diffusion, Hall diffusion, and ambipolar diffusion. In protoplanetary disks any one of the three modes can be the dominant mode depending on dust and gas density (e.g. Wardle, 2007), and interaction between the different modes may alter the activity of the MRI (Wardle & Salmeron, 2012). In this thesis I focus only on the Ohmic diffusion because it is the most studied one in the context of the MRI. I leave the treatment of other diffusion modes for future studies.

Taking the electric discharge into account, I construct a simple model of the discharge as follows, in terms of an appropriate choices of η_0 and J_{crit} :

$$\mathbf{E}' = \frac{4\pi}{c^2} \eta(J) \mathbf{J}, \quad (3.1)$$

$$\begin{aligned} \eta(J) &= \eta_0 && \text{if } J < J_{\text{crit}}, \\ &= \frac{J_{\text{crit}}}{J} \eta_0 && \text{if } J > J_{\text{crit}}. \end{aligned} \quad (3.2)$$

This nonlinear diffusivity model states that the electric field on the fluid co-moving frame never exceeds a critical value, $E'_{\text{crit}} = 4\pi c^{-2} \eta_0 J_{\text{crit}}$, and thus the magnetic diffusivity η varies depending on electric current J , and Ohm's law become nonlinear.

Note that the smallest space scale dealt in the simulations is of order of 10^{-2} AU. The actual scale of the discharge structures can be much smaller than this. The estimate for the

Symbol	Value (Dimension)	Definition	Location
ρ_g	($[g \text{ cm}^{-3}]$)	Gas density	(3.7)
\mathbf{u}_g	($[\text{cm s}^{-1}]$)	Gas velocity	(3.8)
\mathbf{B}	($[g^{1/2} \text{ cm}^{-1/2} \text{ s}^{-1}]$)	Magnetic field	(3.9)
P	$c_s^2 \rho$	Pressure with isothermal equation of state	(3.10)
\mathbf{E}	($[g^{1/2} \text{ cm}^{-1/2} \text{ s}^{-1}]$)	Electric field in the lab frame	(3.11)
\mathbf{E}'	($[g^{1/2} \text{ cm}^{-1/2} \text{ s}^{-1}]$)	Electric field in the comoving frame	(3.1)
\mathbf{J}	($[g^{1/2} \text{ cm}^{-3/2} \text{ s}^{-1}]$)	Electric current	(3.13)
η_0	($[\text{cm}^2 \text{ s}^{-1}]$)	Linear coefficient and —	
J_{crit}	($[g^{1/2} \text{ cm}^{-3/2} \text{ s}^{-1}]$)	— critical current for extended Ohm's law	(3.2)
P_0	($[g \text{ cm}^{-1} \text{ s}^{-2}]$)	Initial pressure	
β	$2c_s^2/v_{\text{AZ}}^2$	Plasma beta	
B_{z0}	$\sqrt{\beta} B_{\text{eqp}}$	Initial, vertical net magnetic field	(3.16)
h	c_s/Ω	Disk scale-height	(3.6)
B_{eqp}	$\sqrt{8\pi P_0}$	The nondimensionalization unit of magnetic field	(3.4)
J_{eqp}	$cB_{\text{eqp}}/4\pi H$	The nondimensionalization unit of current	(3.5)
R_M	$v_{\text{AZ}}^2/\eta_0 \Omega$	Magnetic Reynolds number	§3.1.3
f_Σ	1.0	Surface Density Multiplier	(3.39)
γ	3/2	Power Law Index of the Surface Density	(3.39)
a_d	$0.1 \mu \text{ m}$	Radius of Solid Dust Particle	(3.46)
f_d	0.01	Dust to Gas Ratio	(3.49)

Table 3.1. The list of symbols used in this chapter.

lower limit of the size of such structures is their thickness, which is of the order of 5000 times electron mean free path (Pilipp et al., 1992).

However, the macroscopic discharge model can be derived from the microscopic discharge relation $|E'| < E'_{\text{crit}}$ that holds everywhere in the plasma. For example, the x -component of the discretized electric field $\langle E'_x \rangle$ is obtained from the line integral of the real field over the discretization length ΔV , as

$$\begin{aligned} |\langle E'_x \rangle| &= \left| \frac{\int E'_x dV}{\Delta V} \right| \\ &\leq \frac{\int |E'_x| dV}{\Delta V} \\ &\leq \frac{\int E'_{\text{crit}} dV}{\Delta V} \\ &= E'_{\text{crit}}. \end{aligned} \quad (3.3)$$

Therefore, Equations (3.1), (3.2) can be used as a “coarse-grained model” where E' , J are interpreted as spatial averages. If the electrical breakdown occurs in a scale smaller than the grid size, the spatially averaged electric field is smaller than E'_{crit} . Thus, in general, the electrical breakdown may occur even in the region where $\langle E'_{\text{crit}} \rangle$ is smaller than E'_{crit} . Therefore, Equations (3.1) and (3.2) may underestimate, but not overestimate, the occurrence of electric discharges.

I use the following units of magnetic field and electric current:

$$B_{\text{eqp}} \equiv \sqrt{8\pi P_0}, \quad (3.4)$$

$$J_{\text{eqp}} \equiv \frac{c B_{\text{eqp}}}{4\pi H}, \quad (3.5)$$

and the scale height

$$h = \frac{c_s}{\Omega}. \quad (3.6)$$

I adopt a local, Kepler-rotation shearing box that has radial (x), azimuthal (y) and vertical (z) axes, and solve the following resistive magnetohydrodynamic (MHD) equations numerically:

$$\frac{\partial \rho_g}{\partial t} + \nabla \cdot (\rho_g \mathbf{u}_g) = 0, \quad (3.7)$$

$$\begin{aligned} \frac{\partial \mathbf{u}_g}{\partial t} + \mathbf{u}_g \cdot \nabla \mathbf{u}_g &= -\frac{1}{\rho_g} \nabla (P + \frac{B^2}{8\pi}) + \frac{1}{4\pi\rho_g} (\mathbf{B} \cdot \nabla \mathbf{B}) \\ &\quad - 2\boldsymbol{\Omega} \times \mathbf{u}_g + 3\Omega^2 x \hat{\mathbf{x}}, \end{aligned} \quad (3.8)$$

$$\frac{\partial \mathbf{B}}{\partial t} = -c \nabla \times \mathbf{E}, \quad (3.9)$$

with isothermal EOS

$$P = c_s^2 \rho_g. \quad (3.10)$$

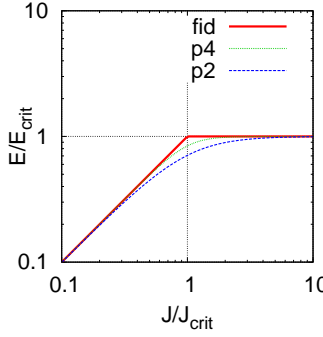


Figure 3.1. Electric field amplitude as functions of current in the three different models of nonlinear Ohm's law. The symbols `fid`, `p2`, and `p4` correspond to equation (3.2), (3.14), and (3.15), respectively.

Had I used the adiabatic EOS, the internal energy would have kept growing as the linear function of time (Hawley et al. (1995)). Therefore, I instead use the isothermal EOS to approximate the steady state attained by the cooling processes present in the protoplanetary disks.

The nonlinear Ohm's law reads:

$$\mathbf{E} = -\frac{1}{c}\mathbf{u}_g \times \mathbf{B} + \frac{4\pi}{c^2}\eta(J)\mathbf{J}, \quad (3.11)$$

$$(3.12)$$

$$\mathbf{J} = \frac{c}{4\pi}\nabla \times \mathbf{B}, \quad (3.13)$$

Here, I have studied three different models for nonlinear diffusivity $\eta(J)$. In addition to the fiducial model(`fid`), Eqs. (3.1) (3.2), I have studied the following two models:

$$(p2) : \eta(J) = (1 + (\frac{J_{\text{crit}}}{J})^{-2})^{-\frac{1}{2}}, \quad (3.14)$$

$$(p4) : \eta(J) = (1 + (\frac{J_{\text{crit}}}{J})^{-4})^{-\frac{1}{4}}. \quad (3.15)$$

The electric field as a function of current density in these three models is shown in Figure 3.1.

In lines of Hawley et al. (1995), I set up numerical initial conditions as follows. I use the disk scaleheight H as the unit length. The box size is $(L_x, L_y, L_z) = (1, 2\pi, 1)$. First, I set the average values $\rho_{g0} = 1$ and $P_0 = 10^{-6}$ to every mesh, and let fluid velocity to be at rest in shearing box frame; $(v_x, v_y, v_z) = (0, -(3/2)\Omega x, 0)$. Here, $c_s = 10^{-3}$, and also $\Omega = 10^{-3}$.

Next, I introduce random perturbations in density, pressure, and velocity. The density and pressure perturbations are in proportion so that the isothermal EOS is met, and the amplitude is $\delta\rho/\rho_0 = \delta P/P_0 = 2.5 \times 10^{-2}$. I perturb the velocity component-wise, with the amplitude $\delta v_i = 5 \times 10^{-3}c_s$ for each.

I set uniform magnetic field in the z -direction, and express the initial field strength by the plasma beta,

$$\beta \equiv {B_{\text{eqp}}}^2/{B_{z0}}^2 = 8\pi P_0/{B_{z0}}^2. \quad (3.16)$$

The plasma beta satisfy the following relation held between the sound speed c_s and the Alfvén velocity along the magnetic field v_{AZ} :

$$\beta = \frac{2c_s^2}{{v_{\text{AZ}}}^2}. \quad (3.17)$$

I define the magnetic Reynolds number as

$$R_M \equiv {v_{\text{AZ}}}^2/\eta_0\Omega, \quad (3.18)$$

using the Alfvén velocity $v_{\text{AZ}} = B_{z0}/\sqrt{4\pi\rho_g}$ set by the initial vertical magnetic field. This is in accordance with Sano et al. (2000) and Inutsuka & Sano (2005) while some literature adopts different definition (e.g. $R_M \equiv c_s^2/\eta_0\Omega$ in Fleming et al., 2000).

I use multidimensional mesh-based MHD code ‘ATHENA’ (Gardiner & Stone, 2005, 2008), an open-source MHD code for my simulations.

3.1.3 Simulations Procedure

I vary the initial magnetic field strength and the diffusivity models, and I classify each set of parameters as either \circlearrowright active zone, \times dead zone, or \triangle sustained zone. The experiment method and the definition of the three classes are given in this section.

The parameters I have investigated are the initial vertical field strength (represented by plasma β), the linear diffusivity (represented by magnetic Reynolds number R_M), and the critical current J_{crit} . The range of the survey was $400 \leq \beta \leq 25600$, $0.002 \leq R_M \leq 2$ and $0.01 \leq J_{\text{crit}}/J_{\text{eqp}} \leq 100$. In addition, the limiting cases of $R_M = \infty$ and $J_{\text{crit}}/J_{\text{eqp}} = \infty$, that respectively correspond to ideal MHD models and linear Ohm's law models, are studied for comparison with the literature.

For each value of β , I prepared the initial condition as described in section 3.1.2, and continued the simulation for 10 orbits ($t = 20\pi/\Omega$), at first with magnetic diffusivity turned off ($\eta(J) = 0$). While running the simulations, I created restart data for every periodic points ($t = 2n\pi/\Omega$ where n is an integer). The condition allowed the MRI to grow and saturate in about 5 orbits ($t = 10\pi/\Omega$).

Then, for each pair of $(R_M, J_{\text{crit}}/J_{\text{eqp}})$, I turned on the diffusivity and re-started the simulation either from the initial laminar flow ($t = 0$) or the saturated MRI states at 8, 9 and 10 orbit ($t = 16\pi/\Omega, 18\pi/\Omega, 20\pi/\Omega$). I numerically evolved them until they reach 20 orbit ($t = 40\pi/\Omega$). The reason why I have adopted three different MRI saturated initial conditions ($t = 16\pi/\Omega, 18\pi/\Omega, 20\pi/\Omega$) for each set of the parameters is that a ‘turbulent initial condition’ is not unique; therefore whether our results depend on the choice of the initial condition or not requires investigation.

During each simulation run, I recorded the space averages of physical quantities as the functions of time, such as magnetic energy density B^2 , the Reynolds and Maxwell stress $\rho v_x \delta v_y, -B_x B_y/4\pi$, and the squared current J^2 . After the simulations I studied the time

zone	from laminar?	from ideal MRI?
○active	unstable	unstable
×dead	stable	stable
△sustained	stable	unstable

Table 3.2. The zone names and the meaning of the symbols in Figures 3.3 and 3.4.

average of the quantities. For a physical quantity A , I denote its space and time average by $\langle A \rangle$ and \bar{A} , respectively. Their definitions are as follows:

$$\langle A \rangle \equiv \frac{\int dx \int dy \int dz A}{\int dx \int dy \int dz}, \quad (3.19)$$

$$\bar{A} \equiv \frac{\int dt A}{\int dt}. \quad (3.20)$$

The space average is taken for the entire computational domain ($0 < x < L_x$, $0 < y < L_y$, $0 < z < L_z$), numerical resolution is $(N_x, N_y, N_z) = (64, 128, 64)$, and the time average is taken for the last five orbit ($30\pi < t < 40\pi$) unless otherwise mentioned. The statistics for the important sets of parameters are presented at the end of the chapter as tables.

Using the average values, I classify each set of the parameter $(\beta, R_M, J_{\text{crit}}/J_{\text{eqp}})$ as follows (c.f. Table 3.2). First, a parameter is in ○active zone if the MRI is observed both in the simulation started from laminar flow as well as in all of the three simulations started from the saturated MRI states. Second, a parameter is in ×dead zone if the instability is not observed neither in the simulation started from laminar flow as well as in any of the three simulations started from the saturated MRI states. Finally, a parameter is in △sustained zone, if the MRI is observed at in all the three simulations started from the saturated MRI states, but *not* at the end of the simulation started from laminar flow.

3.1.4 The Result of Shearing-Box Simulations

The typical behavior of the current for the active zone, dead zone and sustained zone are in Figure 3.2. From the simulations I have observed that the three classes (active, dead and sustained) are exhaustive: that the runs started from 8,9 and 10 orbit always agree in terms of the classification; and that if the MRI dies when starting from saturated initial condition, it also does not activate starting from laminar initial condition.

To classify the active, dead and sustained zone, I need to assess the magnetorotational instability of the system, so I introduce the following criteria for quantitative assessment. The system is magnetorotationally unstable if the averaged current $\langle J^2 \rangle^{1/2}$ is greater than $0.1J_{\text{eqp}}$, and stable if otherwise. Here, the time average is taken for the last five orbit ($30\pi < t < 40\pi$). Previous simulations tell that the quantity $\langle J^2 \rangle^{1/2}$ is a good indicator for the stability, since it either fluctuates around mean value $\langle J^2 \rangle^{1/2} \simeq 10J_{\text{eqp}}$ (unstable) or go under $\langle J^2 \rangle^{1/2} < 0.1J_{\text{eqp}}$ almost monotonically with little vibration (stable), and there is no ambiguity between the two; c.f. Figure 3.2.

However, as R_M becomes smaller, the diffusion timescale becomes shorter, and the wall clock time for the simulations until $t = 40\pi$ becomes impractically larger. Therefore,

3.1. MAGNETOROTATIONAL INSTABILITY WITH NONLINEAR OHM'S LAW55

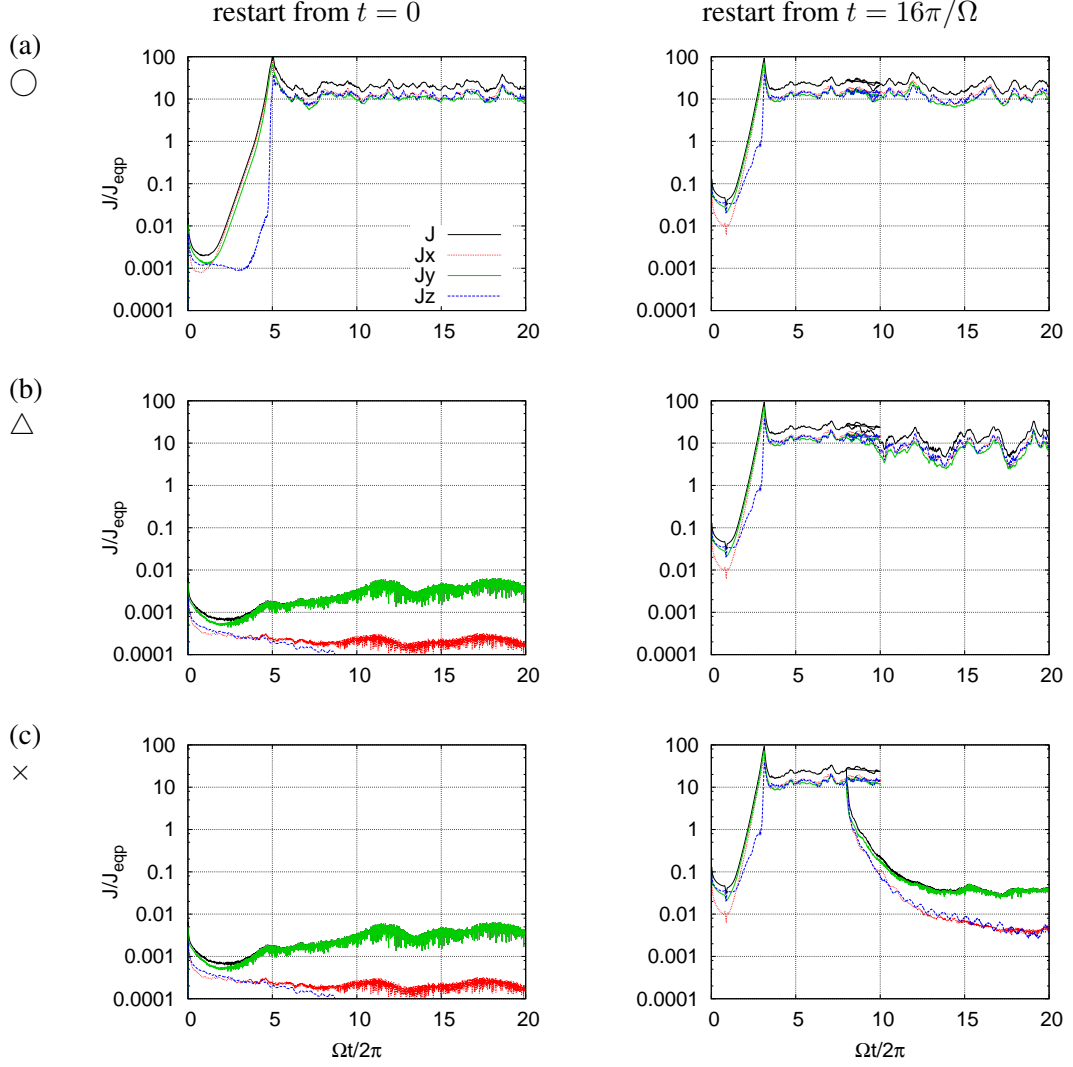


Figure 3.2. Time evolution of the averaged current density for three magnetic diffusivity models. Models are (a) $\beta = 400$, $R_M = 0.6$, $J_{\text{crit}}/J_{\text{eqp}} = 1$ (b) $\beta = 400$, $R_M = 0.2$, $J_{\text{crit}}/J_{\text{eqp}} = 1$ (c) $\beta = 400$, $R_M = 0.2$, $J_{\text{crit}}/J_{\text{eqp}} = 10$. The graphs show typical current behavior for (a) \circlearrowleft active zone, (b) \triangle sustained zone, or (c) \times dead zone.

These results, as well as other results in this chapter, was first presented in Muranushi et al. (2012).

for the parameter range $R_M < 0.01$, I terminate the simulations at 1.5×10^6 cycles and determine the class by extrapolations.

Figures 3.3 and 3.4 show the result of the parameter survey. I have found that sustained zone exist — the MRI does exhibit hysteresis behavior for a certain set of parameters.

To study the influences of the numerical resolutions, I have performed simulations using the different numerical resolution $N_x = 32, 48, 64$ (fiducial) and 80 while keeping the aspect ratio $N_x : N_y : N_z = 1 : 2 : 1$, for three different set of parameters $(\beta, R_M, J_{\text{crit}}/J_{\text{eqp}}) = (400, 0.6, 1), (400, 0.2, 1)$ and $(400, 0.2, 1)$. Figure 3.5 summarizes the convergence tests. Within these sets of parameters, no dependence of the classification on the numerical resolution was observed.

I have also studied if the results depend on the model of nonlinear Ohm's law. In addition to the fiducial(`fid`) model, Eq. (3.2), I have studied two smoothly transiting models, Eqs. (3.14) and (3.15). To distinguish the three models see Figure 3.1.

Figure 3.6 summarizes the time evolution of the current density in the simulations with the three typical sets of parameters $(\beta, R_M, J_{\text{crit}}/J_{\text{eqp}}) = (400, 0.6, 1), (400, 0.2, 1)$ and $(400, 0.2, 1)$. Within the regime tested, the hysteresis behavior does not depend on the detail of the non-linear resistivity models.

Figures 3.3 and 3.4 suggest the following condition for the \triangle sustained zone:

$$\frac{J_{\text{crit}}}{J_{\text{eqp}}} \frac{1}{R_M} \leq f_{\text{whb}}, \quad (3.21)$$

where f_{whb} is a proportionality constant that satisfies $f_{\text{whb}} \simeq 5 - 15$ for $400 \leq \beta \leq 1600$, and $f_{\text{whb}} \simeq 15 - 50$ for $\beta \geq 3200$. I will now deduce the interpretation of this relation in terms of the *work-heat balance* in the resistive MRI.

I also remark that within parameter regions that is in active zone, $R_M < 1$, and with larger J_{crit} , large-amplitude time-variability of physical quantities was observed, such as in magnetic fields. The variability is due to repeated growth and reconnection of the channel solutions. This phenomenon is reported by Fleming et al. (2000).

3.1.5 Interpretation of The Simulation Results

In this section, I show that Equation (3.21) can be understood as a condition of the balance between the magnetic energy dissipated by Joule heating per unit volume (W_J) and the work done by shearing motion per unit volume (W_{sh}).

Q_{whb} is the left hand side of Equation (3.21):

$$Q_{\text{whb}} \equiv \frac{J_{\text{crit}}}{J_{\text{eqp}}} \frac{1}{R_M}. \quad (3.22)$$

The condition for self-sustained MRI is $Q_{\text{whb}} < f_{\text{whb}}$, which is to be explained in this section.

First, substitute $R_M \equiv v_{\text{AZ}}^2 / \eta_0 \Omega$;

$$Q_{\text{whb}} = \frac{J_{\text{crit}}}{J_{\text{eqp}}} \frac{\eta_0 \Omega}{v_{\text{AZ}}^2} \quad (3.23)$$

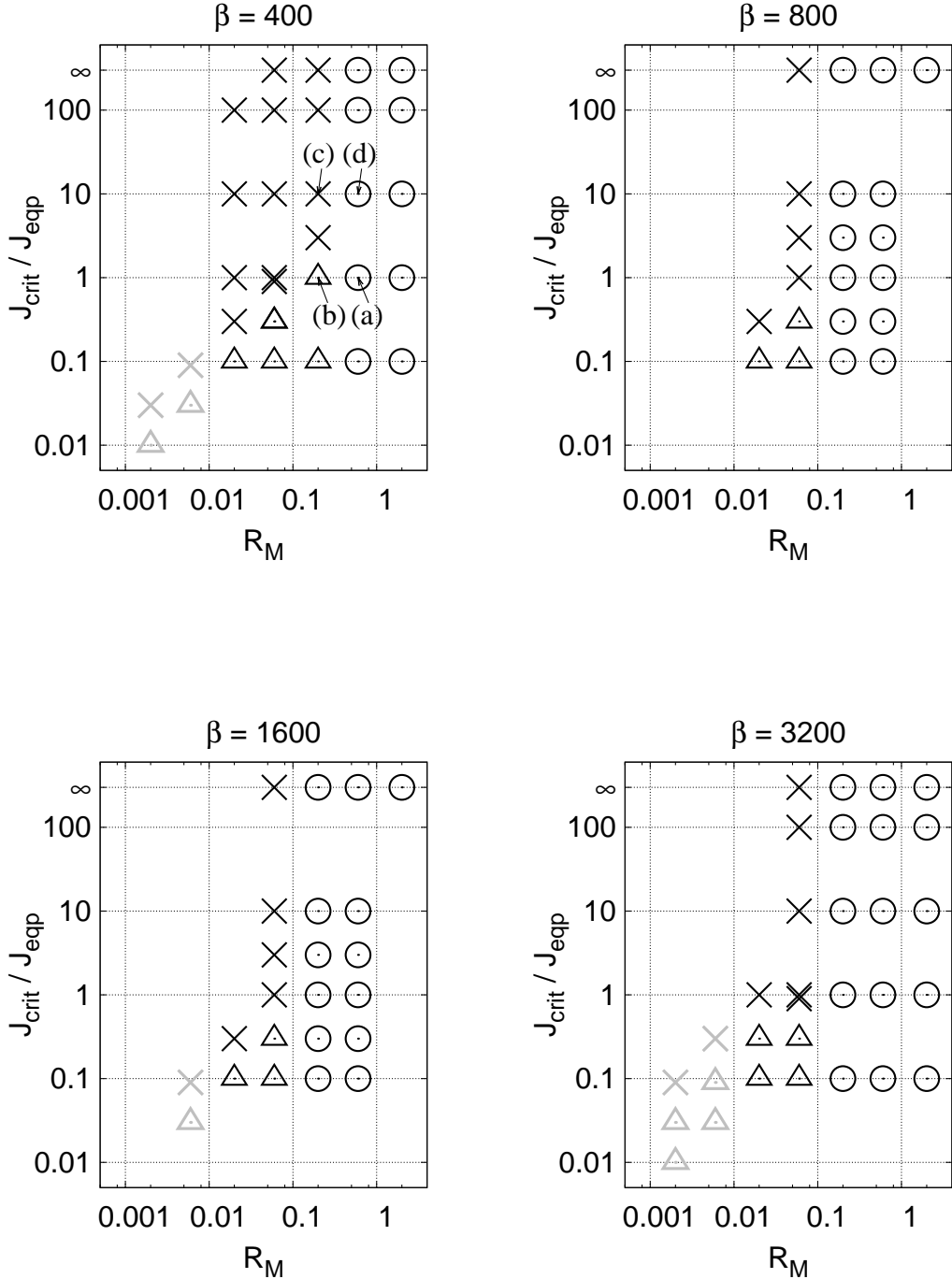


Figure 3.3. Distribution of the sets of parameters (β , R_M , $J_{\text{crit}} / J_{\text{eqp}}$) in my simulations. I classify each of them as either \bigcirc active zone, \triangle sustained zone, or \times dead zone. This page includes the data for $400 \leq \beta \leq 3200$. The parameters classified by extrapolations are marked by light gray symbols.

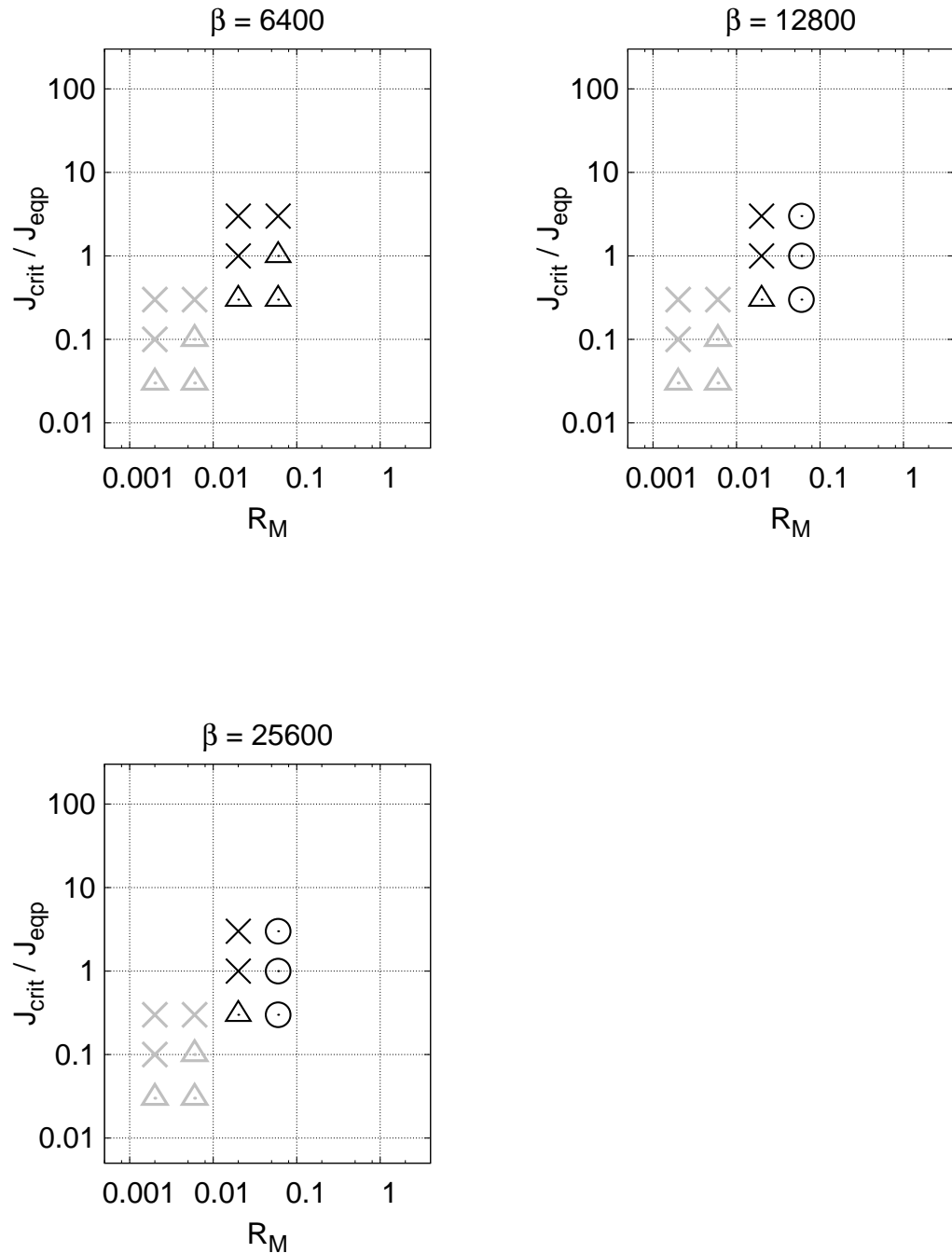


Figure 3.4. Continued from Figure 3.3, the data for $6400 \leq \beta \leq 25600$.

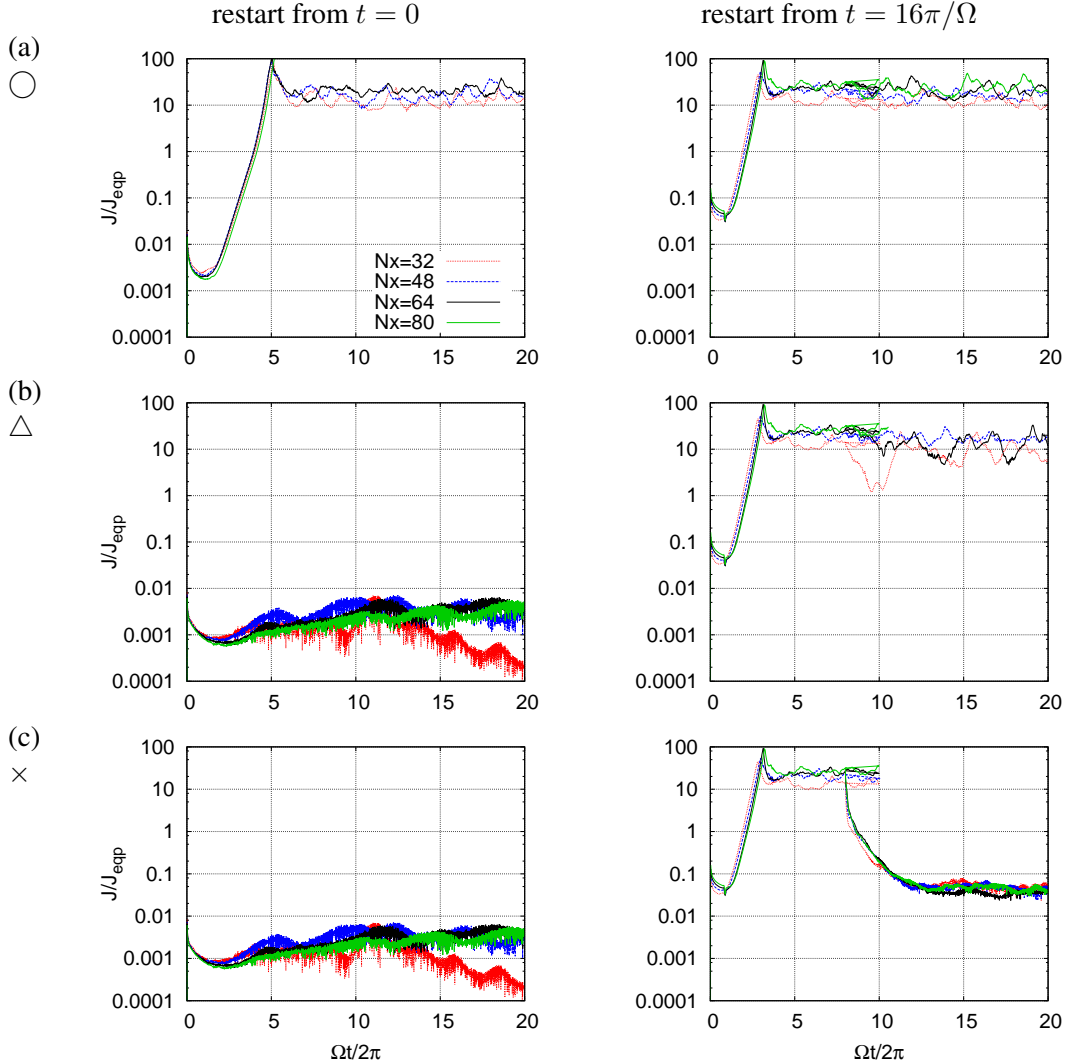


Figure 3.5. Dependence of the MRI behavior on the resolution. The development of electric current over time in the simulations using the different numerical resolution $N_x = 32, 48, 64$ (fiducial) and 80 while keeping the aspect ratio $N_x : N_y : N_z = 1 : 2 : 1$, for three different set of parameters (a) $\beta = 400$, $R_M = 0.6$, $J_{\text{crit}}/J_{\text{eqp}} = 1$, (b) $\beta = 400$, $R_M = 0.2$, $J_{\text{crit}}/J_{\text{eqp}} = 1$ and (c) $\beta = 400$, $R_M = 0.2$, $J_{\text{crit}}/J_{\text{eqp}} = 10$. They are typical parameter sets for (a) \circlearrowleft active zone, (b) \triangle sustained zone, and (c) \times dead zone, respectively.

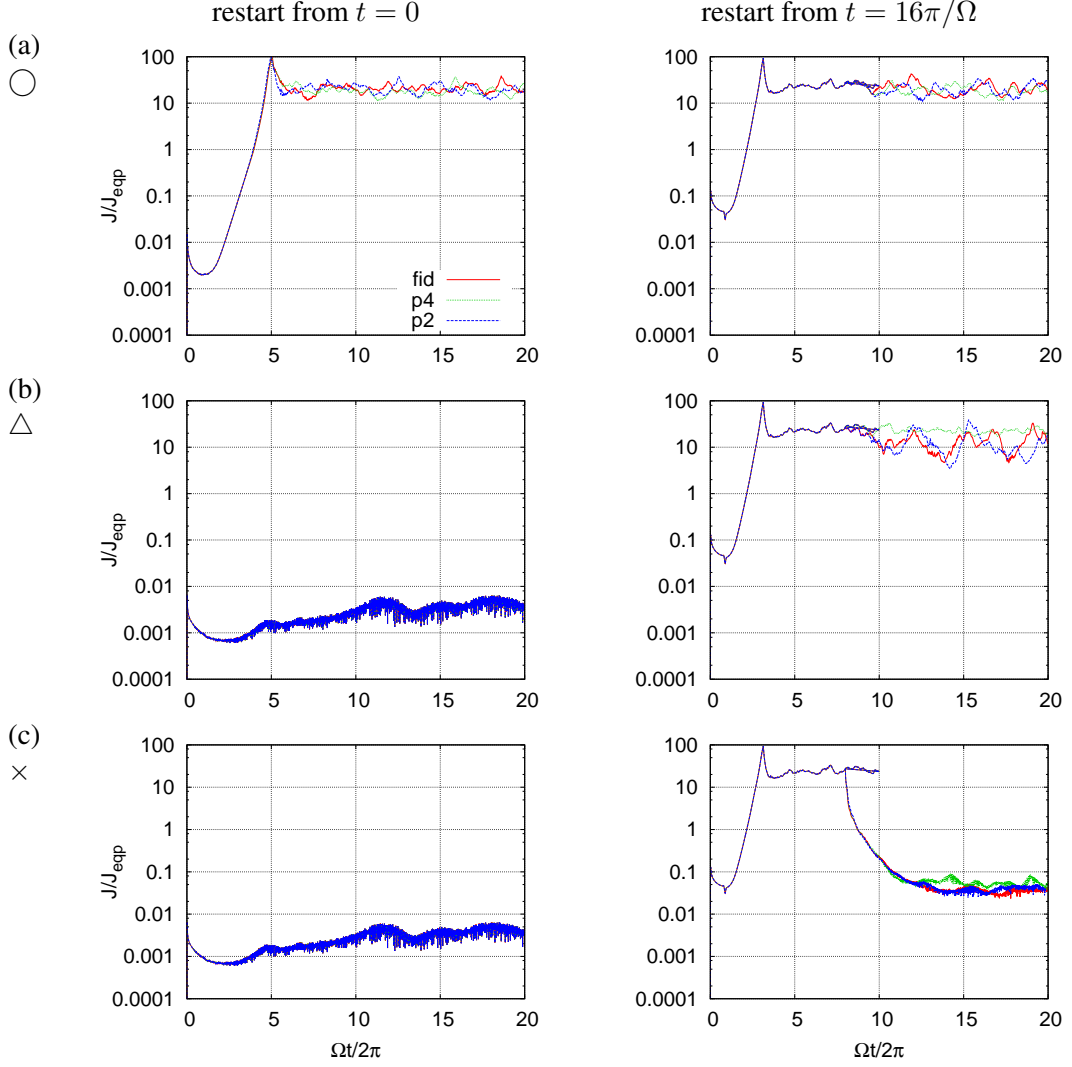


Figure 3.6. Dependence of the MRI behavior on resistivity models. The development of electric current over time in the simulations using different resistivity models *fid*(Eqs. (3.1) (3.2)), *p₂* (Eq. 3.14) and *p₄* (Eq. 3.15), for three sets of parameters (a) $\beta = 400$, $R_M = 0.6$, $J_{\text{crit}}/J_{\text{eqp}} = 1$, (b) $\beta = 400$, $R_M = 0.2$, $J_{\text{crit}}/J_{\text{eqp}} = 1$ and (c) $\beta = 400$, $R_M = 0.2$, $J_{\text{crit}}/J_{\text{eqp}} = 10$; which are typical parameter sets for (a) \circlearrowleft active zone, (b) \triangle sustained zone, and (c) \times dead zone, respectively.

,

Next, when the MRI is active, $\langle J^2 \rangle^{1/2} \simeq f_{\text{sat}} J_{\text{eqp}}$ where f_{sat} is of the order of 10. Since this average current strength lies in super-critical regime of Ohm's law ($J > J_{\text{crit}}$), the electric field is $E'_{\text{crit}} = 4\pi c^{-2} \eta_0 J_{\text{crit}}$ as modeled in Equation (3.1) and (3.2). Therefore, Joule heating per unit volume is estimated as

$$\begin{aligned} W_J &= E'_{\text{crit}} \cdot \langle J^2 \rangle^{1/2} \\ &= E'_{\text{crit}} \cdot f_{\text{sat}} J_{\text{eqp}} \\ &= 4\pi f_{\text{sat}} c^{-2} \eta_0 J_{\text{crit}} J_{\text{eqp}}. \end{aligned} \quad (3.24)$$

To explain the work-heat balance qualitatively, this estimate needs correction due to the high space variability of current field under the discharge conditions. I introduce f_{fill} , the filling factor, the ratio of the volume that contributes to the Joule heating to the total volume. Formally, f_{fill} is defined as the ratio between volume averages of the actual Joule heat generated and the Joule heat estimated by this method:

$$\begin{aligned} f_{\text{fill}} &\equiv \frac{\langle E' J \rangle}{E'_{\text{crit}} \cdot \langle J^2 \rangle^{1/2}} \\ &= \frac{\langle f(J) J \rangle}{\langle J^2 \rangle^{1/2}}, \end{aligned} \quad (3.25)$$

where

$$f(J) = \begin{cases} 1 & \text{if } J > J_{\text{crit}} \\ \frac{J}{J_{\text{crit}}} & \text{if } J < J_{\text{crit}} \end{cases}. \quad (3.26)$$

Using this f_{fill} , Equation (3.24) is rewritten as:

$$W_J \equiv 4\pi f_{\text{fill}} f_{\text{sat}} c^{-2} \eta_0 J_{\text{crit}} J_{\text{eqp}}. \quad (3.27)$$

Substituting η_0 in (3.23) with (3.27) gives

$$\begin{aligned} Q_{\text{whb}} &= \frac{c^2 W_J \Omega}{4\pi f_{\text{fill}} f_{\text{sat}} J_{\text{eqp}}^2 v_{\text{AZ}}^2}, \\ W_J &= \frac{4\pi f_{\text{fill}} f_{\text{sat}} J_{\text{eqp}}^2 v_{\text{AZ}}^2 Q_{\text{whb}}}{c^2 \Omega}. \end{aligned} \quad (3.28)$$

Substituting v_{AZ} with Equation (3.17) and then c_s with (3.6), J_{eqp} with Equation (3.5) and then B_{eqp} with Equation (3.4) gives

$$W_J = \frac{4 f_{\text{fill}} f_{\text{sat}} P_0 \Omega Q_{\text{whb}}}{\beta}. \quad (3.29)$$

On the other hand,

$$\begin{aligned} W_{\text{sh}} &\equiv \frac{3}{2} \Omega \langle w_{xy} \rangle \\ &= \frac{3}{2} \alpha \Omega P, \end{aligned} \quad (3.30)$$

β	$\bar{\alpha}$	$\overline{\left\langle \frac{B^2}{8\pi P_0} \right\rangle}$	$\overline{f_{\text{sat}}}$	$\overline{f_{\text{fill}}}$	$f_{\text{whb}}(\beta)$
400	0.176 ± 0.036	0.222 ± 0.040	14.5 ± 1.7	0.252 ± 0.001	7.19 ± 0.81
800	0.143 ± 0.035	0.206 ± 0.057	17.4 ± 2.7	0.259 ± 0.001	9.33 ± 1.03
1600	0.104 ± 0.027	0.166 ± 0.047	17.4 ± 1.8	0.265 ± 0.002	13.3 ± 2.3
3200	0.0523 ± 0.0206	0.0916 ± 0.0411	12.2 ± 3.9	0.262 ± 0.008	19.0 ± 3.9
6400	0.0236 ± 0.0041	0.0386 ± 0.0072	9.58 ± 1.04	0.263 ± 0.003	22.2 ± 1.6
12800	0.0182 ± 0.0032	0.0300 ± 0.0060	9.84 ± 0.88	0.270 ± 0.000	32.6 ± 2.8
25600	0.0185 ± 0.0063	0.0315 ± 0.0128	10.7 ± 1.5	0.275 ± 0.001	58.5 ± 12.4

Table 3.3. The $f_{\text{whb}}(\beta)$ calculated from the experimental data. I first calculated the time and space averaged quantities $\bar{\alpha}$ and $\overline{f_{\text{sat}}}$ for each runs. Then for the ensemble of runs, I calculated the means and the standard deviations of the quantities. The ensemble constitutes of runs that (1) belong to \triangle sustained zone, (2) are restarted runs ($t = 16\pi/\Omega, 18\pi/\Omega, 20\pi/\Omega$) so that they are magnetorotationally unstable, and (3) have the largest product $J_{\text{crit}}/J_{\text{eqp}} \cdot 1/R_M$ so that they face the \triangle sustained zone - \times dead zone boundary.

where α is Shakura & Sunyaev (1973) 's α parameter. Substituting Equation (3.30) into Equation (3.29), one obtains

$$W_J = \frac{8f_{\text{fill}}f_{\text{sat}}Q_{\text{whb}}}{3\alpha\beta}W_{\text{sh}}. \quad (3.31)$$

For the MRI to sustain itself by the discharge process, the Joule heating W_J needs to be equal or smaller than W_{sh} :

$$W_J \lesssim W_{\text{sh}}. \quad (3.32)$$

This gives the following constraint on the left hand side of Equation (3.23):

$$\begin{aligned} Q_{\text{whb}} &= \frac{3\alpha\beta}{8f_{\text{fill}}f_{\text{sat}}} \frac{W_J}{W_{\text{sh}}}, \\ \frac{J_{\text{crit}}}{J_{\text{eqp}}} \frac{1}{R_M} &\lesssim \frac{3\alpha\beta}{8f_{\text{fill}}f_{\text{sat}}} \equiv f_{\text{whb}}(\beta). \end{aligned} \quad (3.33)$$

Thus, the work-heat balance poses an upper limit on the product of $J_{\text{crit}}/J_{\text{eqp}}$ and $1/R_M$, provided that f_{fill} , f_{sat} and α are constants that do not depend on J_{crit} and R_M , but only on β . This explains the inverse-proportional relations observed in Figures 3.3 and 3.4. The $f_{\text{whb}}(\beta)$ calculated with this interpretation using the experimental data are in Table 3.3.

Equation (3.33) can be further simplified by use of the saturation predictor proposed by Hawley et al. (1995) . The proposed predictors read

$$\alpha P = 0.61 \pm 0.06 \overline{\left\langle \frac{B^2}{8\pi} \right\rangle}, \quad (3.34)$$

$$\overline{\left\langle \frac{B^2}{8\pi} \right\rangle} = (1.21 \pm 0.29) \cdot 2\pi \sqrt{\frac{16}{15} \cdot \frac{2}{\beta} P_0}. \quad (3.35)$$

$$(3.36)$$

Using this, Equation (3.33) is rewritten as follows:

$$\begin{aligned} \frac{J_{\text{crit}}}{J_{\text{eqp}}} \frac{1}{R_M} &\lesssim f_{\text{whb}}(\beta) \\ &\simeq (2.54 \pm 0.66) \frac{\beta^{1/2}}{f_{\text{fill}} f_{\text{sat}}}. \end{aligned} \quad (3.37)$$

By ignoring the dependence of f_{fill} and f_{sat} on β , I assume $\overline{f_{\text{fill}}} = 0.264 \pm 0.007$ and $\overline{f_{\text{sat}}} = 13.1 \pm 3.1$. This further simplifies the Equation (3.33) as:

$$f_{\text{whb}}(\beta) \simeq (0.74 \pm 0.26) \beta^{1/2}. \quad (3.38)$$

This is in agreement with the experimental data (Table 3.3) within factor of 2.

3.2 Distribution of The Three MRI Zones within The Protoplanetary Disks

3.2.1 Protoplanetary Disk Model

In the previous section, I have performed the shearing-box simulations of MRI with non-linear Ohm's law, and found the three classes of MRI behavior; active, dead and sustained zones. I have also found the condition for the MRI to be self-sustained. In this section, I apply the findings to the global model of the protoplanetary disks and analyze how they are divided into the three zones.

I will use Minimum-Mass Solar Nebula (MMSN) model introduced by Hayashi et al. (1985) as the fiducial disk model;

$$\Sigma^{\bowtie}(r) = f_{\Sigma} \Sigma_0 \left(\frac{r}{\text{AU}} \right)^{-\gamma}, \quad (3.39)$$

$$T^{\bowtie}(r) = T_0 \left(\frac{r}{\text{AU}} \right)^{-\frac{1}{2}}. \quad (3.40)$$

Here, $\Sigma_0 = 1.7 \times 10^3 \text{ g cm}^{-3}$ and $T_0 = 2.8 \times 10^2 \text{ K}$ are the surface density and the temperature at 1AU, respectively. f_{Σ} is the nondimensional surface density parameter. Fiducial value for the surface density power index is $\gamma = 3/2$. Since I assume the isotropic equation of state (EOS), the ratio of specific heats $\gamma = 1$ in my model, and the thermal velocities for gas molecules and electrons are

$$c_s(r) = \sqrt{\frac{k_B T}{\mu m_H}}, \quad (3.41)$$

$$v_e(r) = \sqrt{\frac{k_B T}{m_e}}, \quad (3.42)$$

respectively, where μ is the mean molecular weight of the gas.

Since the self gravity of the disk is negligible, the disk is approximately in Kepler rotation and its orbital angular velocity is

$$\Omega(r) = \sqrt{\frac{GM_*}{r^3}}. \quad (3.43)$$

From the equilibrium between vertical pressure gradient and vertical component of the stellar gravity, the disk density and pressure distributions are:

$$\rho_g(r, z) = \frac{\Sigma}{\sqrt{2\pi}h} \exp\left(\frac{-z^2}{2h^2}\right), \quad (3.44)$$

$$P(r, z) = \frac{\rho_g k_B T}{\mu m_H}, \quad (3.45)$$

where h is the definition of the disk scale-height; c.f. Equation (3.6).

For simplicity, I assume that the every dust particle to be solid sphere of the equal radius a_d and density ρ_s . The mass m_d and geometrical cross section σ_d of the dust particle are

$$m_d = \frac{4\pi}{3} \rho_s a_d^3, \quad (3.46)$$

$$\sigma_d = \pi a_d^2, \quad (3.47)$$

respectively. The fiducial values are $a_d = 0.1 \mu\text{m}$ and $\rho_s = 3 \text{ g cm}^{-3}$.

Using this m_d and dust-to-gas density ratio $f_d = 0.01$, the number densities of dust and gas component are:

$$n_g(r, z) = \frac{\rho_g}{\mu m_H}, \quad (3.48)$$

$$n_d(r, z) = \frac{f_d \rho_g}{m_d}. \quad (3.49)$$

$$(3.50)$$

3.2.2 Ionization Processes

Methods for calculating the charge equilibrium of the dust-plasma in the protoplanetary disks has been studied (Umebayashi & Nakano, 1980, 2009; Fujii et al., 2011). Among those I use Okuzumi (2009) 's method because of its numerical efficiency and generality. First, the gas column density above (χ_\top) and below (χ_\perp) the certain coordinate (r, z) in the disk are

$$\begin{aligned} \chi_\top(r, z) &= \int_z^\infty \rho_g dz \\ &= \frac{\Sigma}{2} \left[1 - \operatorname{erf}\left(\frac{z}{\sqrt{2}h}\right) \right], \end{aligned} \quad (3.51)$$

$$\begin{aligned} \chi_\perp(r, z) &= \int_{-\infty}^z \rho_g dz \\ &= \frac{\Sigma}{2} \left[1 + \operatorname{erf}\left(\frac{z}{\sqrt{2}h}\right) \right], \end{aligned} \quad (3.52)$$

respectively, where

$$\operatorname{erf}(x) \equiv \frac{2}{\sqrt{\pi}} \int_x^\infty e^{-t^2} dt \quad (3.53)$$

is the error function.

According to Sano et al. (2000), the effective ionization rate in the disk is

$$\begin{aligned}\zeta(r, z) \approx & \frac{\zeta_{\text{CR}}}{2} \left\{ \exp\left(-\frac{\chi_{\perp}}{\chi_{\text{CR}}}\right) \right. \\ & \left. + \exp\left(-\frac{\chi_{\perp}}{\chi_{\text{CR}}}\right) \right\} + \zeta_{\text{RA}},\end{aligned}\quad (3.54)$$

where $\chi_{\text{CR}} = 96 \text{ g cm}^{-2}$, $\zeta_{\text{CR}} = 1.0 \times 10^{-17} \text{ s}^{-1}$, and $\zeta_{\text{RA}} = 6.9 \times 10^{-23} \text{ s}^{-1}$.

Using this, Okuzumi (2009)'s nondimensional parameter Θ is calculated as

$$\Theta = \frac{\zeta n_g e^2}{s_i c_s \sigma_d a_d n_d^2 k_B T}, \quad (3.55)$$

and Γ is defined as the solution of the equation

$$\frac{1}{1 + \Gamma} - \left(\frac{s_i}{s_e} \sqrt{\frac{m_e}{\mu m_H}} \exp \Gamma + \frac{\Gamma}{\Theta} \right) = 0. \quad (3.56)$$

Numerically solving Equation (3.56) for Γ gives the number density of ions and electrons, n_i, n_e , as well as the root mean square of the charge per dust particle, $\sqrt{\langle Z^2 \rangle} e$, as follows:

$$n_i(r, z) = \frac{\zeta n_g}{s_i c_s \sigma_d n_d (1 + \Gamma)}, \quad (3.57)$$

$$n_e(r, z) = \frac{\zeta n_g \exp \Gamma}{s_e v_e \sigma_d n_d}, \quad (3.58)$$

$$\langle Z^2 \rangle = \left(\frac{\Gamma a_d}{\lambda} \right)^2 + \frac{1 + \Gamma}{2 + \Gamma} \frac{a_d}{\lambda} \quad (3.59)$$

$$\text{where } \lambda = \frac{e^2}{k_B T},$$

I assume sticking probabilities $s_i = 1$ and $s_e = 0.3$ as assumed by Okuzumi (2009).

Next, I estimate the plasma conductivity. The rate coefficient for the collision between the neutrals and the ions is

$$\langle \sigma v \rangle_i = 2.41 \pi \left(\frac{\alpha e^2}{\mu m_H} \right)^{\frac{1}{2}}. \quad (3.60)$$

I use $\alpha = 7.66 \times 10^{-25} \text{ cm}^3$ as an averaged polarizability. $\langle \sigma v \rangle_e$ is the rate coefficient for collision between neutrals and electrons, whose forms are given in Sano et al. (2000). The rate coefficient for dust particles is

$$\langle \sigma v \rangle_d = \frac{4\pi}{3} a_d^2 c_s. \quad (3.61)$$

This expression is valid as long as a_d is much smaller than the mean free path of the gas molecules.

With these, the magnetic diffusivity is calculated component-wise:

$$\eta_e = \frac{c^2 m_e n_g \langle \sigma v \rangle_e}{4\pi e^2 n_e}, \quad (3.62)$$

$$\eta_i = \frac{c^2 \mu m_H n_g \langle \sigma v \rangle_i}{4\pi e^2 n_i}, \quad (3.63)$$

$$\eta_d = \frac{c^2 \mu m_H n_g \langle \sigma v \rangle_d}{4\pi \langle Z^2 \rangle e^2 n_d}, \quad (3.64)$$

$$\eta_0 = (\eta_e^{-1} + \eta_i^{-1} + \eta_d^{-1})^{-1} \quad (3.65)$$

The value of E'_{crit} is set by the condition that the kinetic energy of the electrons accelerated by the electric field is large enough to initiate the electron avalanche.

$$\begin{aligned} \Delta W &= f_{\text{DP}} e E'_{\text{crit}} l_{\text{mfp}}; \\ E'_{\text{crit}} &= \frac{\Delta W}{f_{\text{DP}} e l_{\text{mfp}}} \\ &= \frac{\Delta W n_g \langle \sigma v \rangle_e}{f_{\text{DP}} e v_e}. \end{aligned} \quad (3.66)$$

Here, $f_{\text{DP}} = 0.43\sqrt{\mu m_H/m_e}$ is the coefficient for average energy of electrons in weakly ionized plasma (Inutsuka & Sano (2005)), and $l_{\text{mfp}} = v_e/(n_g \langle \sigma v \rangle_e)$ is the mean free path of electrons. For ionization energy I use the value for a hydrogen molecule $\Delta W = 15.4 \text{ eV}$.

With this, the critical current is

$$J_{\text{crit}} = \frac{c^2}{4\pi\eta_0} E'_{\text{crit}}. \quad (3.67)$$

Note that the discharge electric field, Equation (3.66) is calculated using the strong electric field limit of the electron distribution function, while I used the weak field limit formulae for charge distributions, Equations (3.55)-(3.61). I adopt this treatment for simplicity.

3.2.3 The Self-Sustained MRI in Global Disk Models

Now I study the distribution of active, sustained and dead zones in the protoplanetary disk models. Sano et al. (2000) gives the condition for MRI unstable region as follows:

$$\frac{2\pi v_{\text{AZ}}}{\Omega} \leq \sqrt{2}H \wedge \frac{2\pi\eta}{v_{\text{AZ}}} \leq \sqrt{2}H. \quad (3.68)$$

Combination of this with work-heat balance model Equation (3.21) gives the following

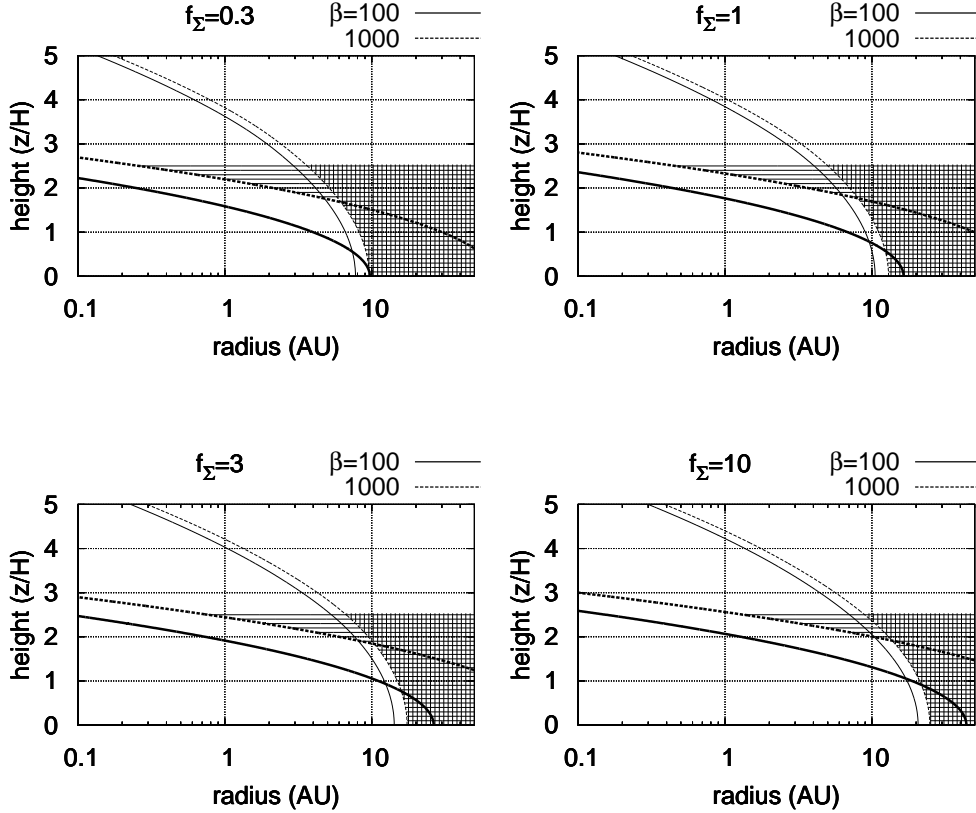


Figure 3.7. Unstable regions in the protoplanetary disks. The thin solid and thin dashed curves represent $\lambda_{\text{res}}/\sqrt{2}H = 1$ for the cases of the magnetic field strength $\beta = 100$ and 1000, respectively, inside of which is dead zone if the MRI self-sustainment is not taken into account (Sano et al. (2000)). The regions above the thick solid and thick dashed curves satisfies Equation (3.21) for $\beta = 100$ and 1000, respectively, and are sustained zones according to the work-heat balance model. Unstable region predicted by Sano et al. (2000) is compared to that predicted by my model for $\beta = 1000$. The unstable regions according to Sano et al. (2000)'s and my model are marked by vertical and horizontal stripes, respectively.

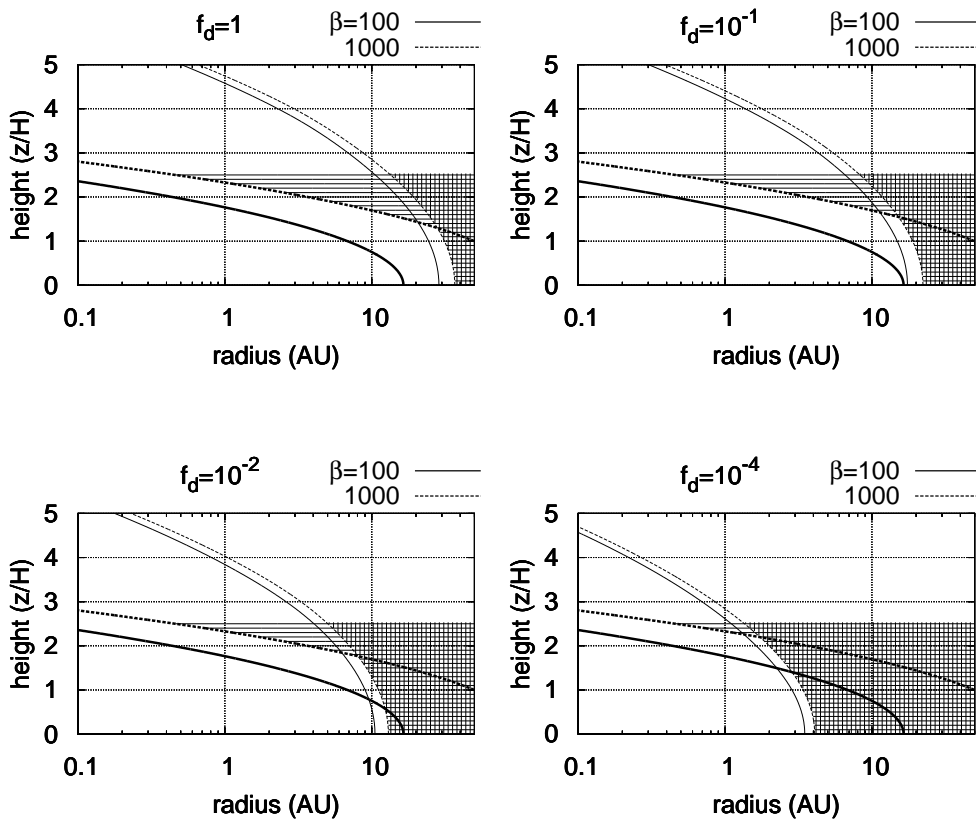


Figure 3.8. Unstable regions for different dust-to-gas ratio. The MRI-unstable regions according to (Sano et al. (2000)) and my model are marked by vertical and horizontal stripes, respectively, for $\beta = 1000$.

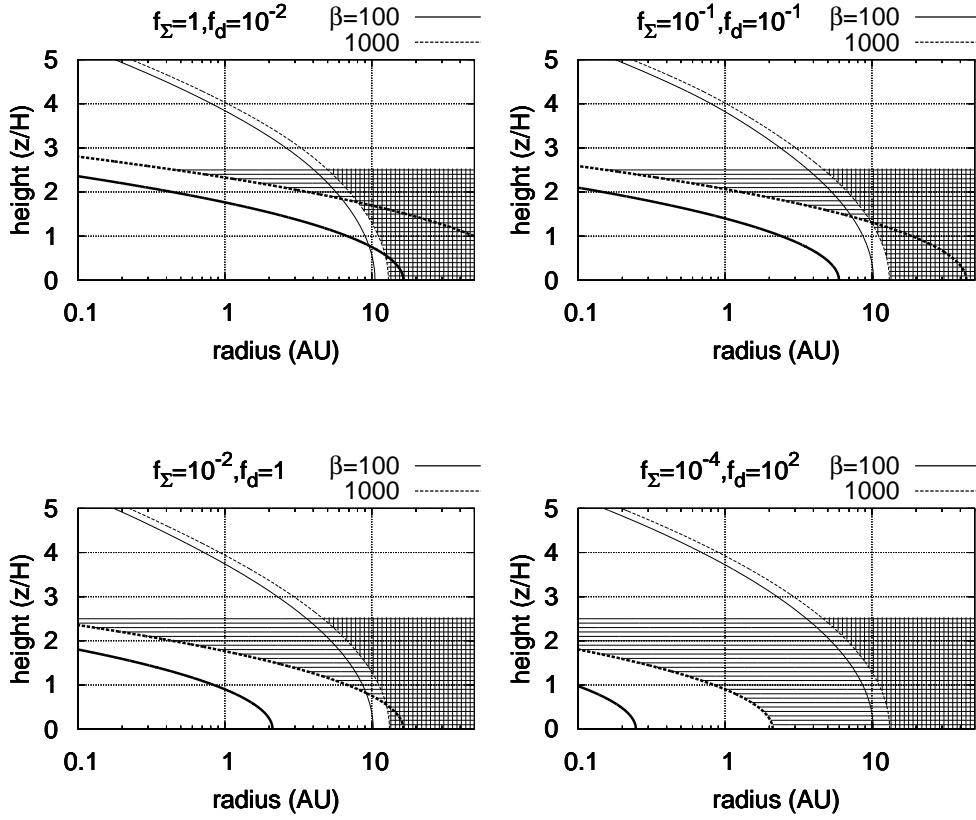


Figure 3.9. Change of unstable regions as the gas density of the disk decreases, while the dust density is kept constant. The MRI-unstable regions according to (Sano et al. (2000)) and my model are marked by vertical and horizontal stripes, respectively, for $\beta = 1000$.

conditions for active, sustained and dead zones, respectively:

$$\frac{2\pi v_{\text{AZ}}}{\Omega} \leq \sqrt{2}H \wedge \frac{2\pi\eta}{v_{\text{AZ}}} \leq \sqrt{2}H \quad (3.69)$$

$$\frac{2\pi v_{\text{AZ}}}{\Omega} \leq \sqrt{2}H \wedge \frac{2\pi\eta}{v_{\text{AZ}}} > \sqrt{2}H \wedge \frac{J_{\text{crit}}}{J_{\text{eqp}}} \frac{1}{R_M} \leq f_{\text{whb}} \quad (3.70)$$

$$\frac{2\pi v_{\text{AZ}}}{\Omega} > \sqrt{2}H \vee (\frac{2\pi\eta}{v_{\text{AZ}}} > \sqrt{2}H \wedge \frac{J_{\text{crit}}}{J_{\text{eqp}}} \frac{1}{R_M} > f_{\text{whb}}) \quad (3.71)$$

Using these Equations (3.69)-(3.71), I construct the active, sustained and dead zones for various global disk model Equations (3.39)-(3.40).

First, Figure 3.7 shows the unstable zones for varying disk surface density, $f_\Sigma = 0.3$, $f_\Sigma = 1$ (the fiducial model), $f_\Sigma = 3$, and $f_\Sigma = 10$. In this figure and following figures, the thick curves are the boundary of the work-heat balance model Equation (3.21), while the thin curves are the boundary of the instability condition in the resistive limit, i.e. the second condition in Equation (3.68). The solid and dashed curves correspond to the plasma beta at the mid-plane $\beta = 100$ and $\beta = 1000$, respectively. The active zones are marked by meshes, and the sustained zones are marked by horizontal stripes.

Figure 3.8 shows the active and sustained zones for dust-to-gas ratio $f_d = 1$, $f_d = 0.1$, $f_d = 0.01$ (the fiducial model), and $f_d = 10^{-4}$. The work-heat balance condition Equation (3.21) is not affected by changing the dust properties such as dust-to-gas ratio f_d or dust size a_d . One can understand this by rewriting the condition Equation (3.23) in the following form:

$$\frac{E'_{\text{crit}}\Omega}{4\pi c^{-2} J_{\text{eqp}} v_{\text{AZ}}^2} \leq f_{\text{whb}}. \quad (3.72)$$

This form does not include a term affected by the dust properties, such as the magnetic diffusivity. On the other hand, E'_{crit} is inversely proportional to the electron mean free path l_{mfp} , and is proportional to the gas number density.

Figure 3.9 shows the evolution of the active and sustained zones as the gas density becomes lower while the dust density is kept constant. The set of parameters (f_Σ, f_d) varies from $(1, 0.01)$ (the fiducial model) to $(0.1, 0.1)$, $(0.01, 1)$, and $(10^{-4}, 100)$. In Figure 3.9 zones are marked for $\beta = 1000$. The midplane of the disk between the radii 2 AU – 20 AU becomes the sustained zone as the gas density becomes 10^{-4} times the fiducial model.

3.3 Conclusions and Discussions

By performing numerical simulations of MHD with nonlinear Ohm's law of the three-dimensional local disks, hysteresis behavior is discovered for certain diffusivity model: If the simulation starts from the laminar-flow initial conditions with small seed fluctuations, the MRI does not activate because of the diffusivity and the flow remains laminar; on the other hand, if the simulation starts from an MRI-turbulent state from an ideal-MHD

simulation, MRI remains active under the same diffusivity model. I have surveyed in three-parameter space (β , J_{crit} , R_M) in search for the regions that the self-sustained MRI in the context of Inutsuka & Sano (2005) takes place. I found the condition, the work-heat balance model, for this hysteresis behavior to take place. The model is $W_J \lesssim W_{\text{sh}}$, where W_J is the magnetic energy dissipated by Joule heating per unit volume and W_{sh} is the work done by background shearing motion per unit volume. This leads to the proportionality relation $\frac{J_{\text{crit}}}{J_{\text{eqp}}} \frac{1}{R_M} \leq f_{\text{whb}}$.

Inutsuka & Sano (2005) concluded that the the energy supply from the shearing motion should be ~ 30 times greater than the energy needed to supplying the enough ionization for the MRI, and predicted the entire disk to be active. However, applying the work-heat balance model to various protoplanetary disk models, I found that in most of the models, the sustained zone is above $z/H > 2 - 3$.

I conclude that in the fiducial protoplanetary disks environment the Joule heating (which has been neglected in Inutsuka & Sano (2005)) becomes the dominant energy dissipation channel and constrains the self-sustainment of MRI, and the midplane of the disk remain dead. However, the gas of the disk dissipates (Alexander et al. (2006a,b); Suzuki et al. (2010)) with observed timescale of $10^6 - 10^7$ years (Cieza et al. (2007); Hernández et al. (2008)), while planetesimals remain and continue planet formation processes. In such late phase of the disk, the sustained zone occupies larger volume of the disk.

Although nonlinear Ohm's law models in this thesis are inspired by the lightning phenomena, whether the Joule heating in this model takes the form of spatially and temporally concentrated stream of ionizing electrons — lightning — or not, has yet to be studied in future works, employing nonthermal plasma studies. This thesis is limited to pointing out some distinguishing properties of such lightning which makes it an interesting subject. The work-heat balance model suggests that in sustained zones the major portion of the shearing motion energy is converted to heat through nonlinear channel of the Ohmic dissipation. This means that the lightning can be one of the most dominant energy channels in the sustained zones. It will also pose a significant back-reaction to the accretion dynamics. The future studies will need to reconsider the contribution of lightning in situations it has been neglected due to lack of energetically viable models, e.g. in chondrule formation (Weidenschilling, 1997).

runID	t	β	$\frac{J_{\text{crit}}}{J_{\text{eqp}}}$	R_M	$\left\langle \frac{B^2}{8\pi P_0} \right\rangle$	$\left\langle \frac{-B_x B_y}{4\pi P_0} \right\rangle$	$\left\langle \frac{\rho v_x \delta v_y}{P_0} \right\rangle$	$\left\langle \frac{J^2}{J_{\text{eqp}}^2} \right\rangle^{0.5}$
3160	0	400	∞	$(1.99 \pm 0.60) \times 10^{-1}$	$(1.05 \pm 0.37) \times 10^{-1}$	$(3.01 \pm 1.49) \times 10^{-2}$	$(2.04 \pm 0.24) \times 10^1$	$\left.\begin{array}{l} \\ \\ \end{array}\right]$
	10	800	∞	$(1.64 \pm 0.69) \times 10^{-1}$	$(8.27 \pm 3.65) \times 10^{-2}$	$(2.26 \pm 0.96) \times 10^{-2}$	$(1.94 \pm 0.30) \times 10^1$	$\left.\begin{array}{l} \\ \\ \end{array}\right]$
	220	0	1600	∞	$(1.94 \pm 0.61) \times 10^{-1}$	$(9.47 \pm 3.19) \times 10^{-2}$	$(2.34 \pm 0.84) \times 10^{-2}$	$(2.07 \pm 0.26) \times 10^1$
	3180	0	3200	∞	$(1.30 \pm 0.27) \times 10^{-1}$	$(6.08 \pm 1.47) \times 10^{-2}$	$(1.68 \pm 0.52) \times 10^{-2}$	$(1.85 \pm 0.18) \times 10^1$
	3612	0	6400	∞	$(7.16 \pm 2.57) \times 10^{-2}$	$(3.14 \pm 0.85) \times 10^{-2}$	$(8.28 \pm 2.51) \times 10^{-3}$	$(1.51 \pm 0.15) \times 10^1$
	3616	0	12800	∞	$(3.61 \pm 0.83) \times 10^{-2}$	$(1.70 \pm 0.35) \times 10^{-2}$	$(6.15 \pm 2.40) \times 10^{-3}$	$(1.24 \pm 0.10) \times 10^1$
3620	0	25600	∞	$(3.61 \pm 0.84) \times 10^{-2}$	$(1.63 \pm 0.36) \times 10^{-2}$	$(5.40 \pm 1.84) \times 10^{-3}$	$(1.22 \pm 0.09) \times 10^1$	$\left.\begin{array}{l} \\ \\ \end{array}\right]$
	3292	0	400	1.0	0.6	$(2.92 \pm 1.56) \times 10^{-1}$	$(1.67 \pm 1.04) \times 10^{-1}$	$(4.81 \pm 3.63) \times 10^{-2}$
	3293	$16\pi/\Omega$	400	1.0	0.6	$(2.74 \pm 1.43) \times 10^{-1}$	$(1.62 \pm 0.99) \times 10^{-1}$	$(4.63 \pm 3.05) \times 10^{-2}$
	3294	$18\pi/\Omega$	400	1.0	0.6	$(2.07 \pm 0.71) \times 10^{-1}$	$(1.21 \pm 0.44) \times 10^{-1}$	$(3.68 \pm 1.62) \times 10^{-2}$
	3295	$20\pi/\Omega$	400	1.0	0.6	$(2.34 \pm 0.82) \times 10^{-1}$	$(1.36 \pm 0.54) \times 10^{-1}$	$(3.86 \pm 1.80) \times 10^{-2}$
	3352	0	400	1.0	0.2	$(2.50 \pm 0.00) \times 10^{-3}$	$(8.24 \pm 6.55) \times 10^{-13}$	$(4.83 \pm 2.58) \times 10^{-7}$
3353	$16\pi/\Omega$	400	1.0	0.2	$(2.03 \pm 1.27) \times 10^{-1}$	$(1.27 \pm 0.86) \times 10^{-1}$	$(4.07 \pm 2.99) \times 10^{-2}$	$(2.10 \pm 0.43) \times 10^1$
	3354	$18\pi/\Omega$	400	1.0	0.2	$(2.21 \pm 0.98) \times 10^{-1}$	$(1.33 \pm 0.50) \times 10^{-1}$	$(4.68 \pm 2.68) \times 10^{-2}$
	3355	$20\pi/\Omega$	400	1.0	0.2	$(2.52 \pm 1.65) \times 10^{-1}$	$(1.56 \pm 1.02) \times 10^{-1}$	$(4.57 \pm 2.72) \times 10^{-2}$
	3348	0	400	10.0	0.2	$(2.50 \pm 0.00) \times 10^{-3}$	$(8.24 \pm 6.55) \times 10^{-13}$	$(4.83 \pm 2.58) \times 10^{-7}$
	3349	$16\pi/\Omega$	400	10.0	0.2	$(2.50 \pm 0.00) \times 10^{-3}$	$(1.77 \pm 1.01) \times 10^{-7}$	$(9.90 \pm 7.50) \times 10^{-5}$
	3350	$18\pi/\Omega$	400	10.0	0.2	$(2.50 \pm 0.00) \times 10^{-3}$	$(2.31 \pm 1.64) \times 10^{-6}$	$(6.06 \pm 9.16) \times 10^{-5}$
3351	$20\pi/\Omega$	400	10.0	0.2	$(2.50 \pm 0.00) \times 10^{-3}$	$(4.85 \pm 3.58) \times 10^{-7}$	$(6.62 \pm 8.64) \times 10^{-5}$	$(4.11 \pm 0.94) \times 10^{-3}$
	3348	0	400	10.0	0.2	$(2.50 \pm 0.00) \times 10^{-3}$	$(8.24 \pm 6.55) \times 10^{-13}$	$(3.60 \pm 0.54) \times 10^{-2}$
	3349	$16\pi/\Omega$	400	10.0	0.2	$(2.50 \pm 0.00) \times 10^{-3}$	$(1.77 \pm 1.01) \times 10^{-7}$	$(3.49 \pm 0.54) \times 10^{-2}$
	3350	$18\pi/\Omega$	400	10.0	0.2	$(2.50 \pm 0.00) \times 10^{-3}$	$(2.31 \pm 1.64) \times 10^{-6}$	$(3.43 \pm 0.36) \times 10^{-2}$
	3351	$20\pi/\Omega$	400	10.0	0.2	$(2.50 \pm 0.00) \times 10^{-3}$	$(4.85 \pm 3.58) \times 10^{-7}$	$(1.67 \pm 0.59) \times 10^1$
	3352	0	400	10.0	0.2	$(2.50 \pm 0.00) \times 10^{-3}$	$(8.24 \pm 6.55) \times 10^{-13}$	$(4.11 \pm 0.94) \times 10^{-3}$
(a)	3353	$16\pi/\Omega$	400	10.0	0.2	$(2.50 \pm 0.00) \times 10^{-3}$	$(1.77 \pm 1.01) \times 10^{-7}$	$(1.50 \pm 0.60) \times 10^1$
	3354	$18\pi/\Omega$	400	10.0	0.2	$(2.50 \pm 0.00) \times 10^{-3}$	$(2.31 \pm 1.64) \times 10^{-6}$	$(1.66 \pm 0.41) \times 10^1$
	3355	$20\pi/\Omega$	400	10.0	0.2	$(2.50 \pm 0.00) \times 10^{-3}$	$(4.85 \pm 3.58) \times 10^{-7}$	$(1.67 \pm 0.59) \times 10^1$
	3348	0	400	10.0	0.2	$(2.50 \pm 0.00) \times 10^{-3}$	$(8.24 \pm 6.55) \times 10^{-13}$	$(4.11 \pm 0.94) \times 10^{-3}$
	3349	$16\pi/\Omega$	400	10.0	0.2	$(2.50 \pm 0.00) \times 10^{-3}$	$(1.77 \pm 1.01) \times 10^{-7}$	$(3.60 \pm 0.54) \times 10^{-2}$
	3350	$18\pi/\Omega$	400	10.0	0.2	$(2.50 \pm 0.00) \times 10^{-3}$	$(2.31 \pm 1.64) \times 10^{-6}$	$(3.49 \pm 0.54) \times 10^{-2}$
(b)	3351	$20\pi/\Omega$	400	10.0	0.2	$(2.50 \pm 0.00) \times 10^{-3}$	$(4.85 \pm 3.58) \times 10^{-7}$	$(1.67 \pm 0.59) \times 10^1$
	3352	0	400	10.0	0.2	$(2.50 \pm 0.00) \times 10^{-3}$	$(8.24 \pm 6.55) \times 10^{-13}$	$(4.11 \pm 0.94) \times 10^{-3}$
	3353	$16\pi/\Omega$	400	10.0	0.2	$(2.50 \pm 0.00) \times 10^{-3}$	$(1.77 \pm 1.01) \times 10^{-7}$	$(3.60 \pm 0.54) \times 10^{-2}$
	3354	$18\pi/\Omega$	400	10.0	0.2	$(2.50 \pm 0.00) \times 10^{-3}$	$(2.31 \pm 1.64) \times 10^{-6}$	$(3.49 \pm 0.54) \times 10^{-2}$
	3355	$20\pi/\Omega$	400	10.0	0.2	$(2.50 \pm 0.00) \times 10^{-3}$	$(4.85 \pm 3.58) \times 10^{-7}$	$(1.67 \pm 0.59) \times 10^1$
	3348	0	400	10.0	0.2	$(2.50 \pm 0.00) \times 10^{-3}$	$(8.24 \pm 6.55) \times 10^{-13}$	$(4.11 \pm 0.94) \times 10^{-3}$
(c)	3349	$16\pi/\Omega$	400	10.0	0.2	$(2.50 \pm 0.00) \times 10^{-3}$	$(1.77 \pm 1.01) \times 10^{-7}$	$(3.60 \pm 0.54) \times 10^{-2}$
	3350	$18\pi/\Omega$	400	10.0	0.2	$(2.50 \pm 0.00) \times 10^{-3}$	$(2.31 \pm 1.64) \times 10^{-6}$	$(3.49 \pm 0.54) \times 10^{-2}$
	3351	$20\pi/\Omega$	400	10.0	0.2	$(2.50 \pm 0.00) \times 10^{-3}$	$(4.85 \pm 3.58) \times 10^{-7}$	$(3.43 \pm 0.36) \times 10^{-2}$

Table 3.4. Statistics of the local simulations abridged. Each run is labeled by an integer. The re-start time is in the second column. Next three columns indicate the initial magnetic field strength, the critical current, and the magnetic Reynolds number. The physical quantity are represented in terms of the time average and standard deviation of the space average, i.e. A is in the format $\overline{\langle A \rangle} \pm \left(\langle A \rangle^2 - \overline{\langle A \rangle}^2 \right)^{0.5}$. In this table are runs for ideal MHD, runs in Figure 3.2 that represent the behavior in (a) active, (b) sustained, and (c) dead zones, runs that constitute sustained-dead zone boundaries for $\beta = 400, 3200$

runID	t	β	$\frac{J_{\text{crit}}}{J_{\text{eqp}}}$	R_M	$\left\langle \frac{B^2}{8\pi P_0} \right\rangle$	$\left\langle \frac{-B_x B_y}{4\pi P_0} \right\rangle$	$\left\langle \frac{\rho v_x \delta v_y}{P_0} \right\rangle$	$\left\langle \frac{J^2}{J_{\text{eqp}}^2} \right\rangle^{0.5}$
3352	0	400	1.0	0.2	$(2.50 \pm 0.00) \times 10^{-3}$	$(8.24 \pm 6.55) \times 10^{-13}$	$(4.83 \pm 2.58) \times 10^{-7}$	$(4.11 \pm 0.94) \times 10^{-3}$
3353	$16\pi/\Omega$	400	1.0	0.2	$(2.03 \pm 1.27) \times 10^{-1}$	$(1.27 \pm 0.86) \times 10^{-1}$	$(4.07 \pm 2.99) \times 10^{-2}$	$(1.50 \pm 0.60) \times 10^1$
3452	0	400	0.9	0.06	$(2.50 \pm 0.00) \times 10^{-3}$	$(3.05 \pm 2.55) \times 10^{-13}$	$(4.29 \pm 2.47) \times 10^{-7}$	$(2.22 \pm 0.52) \times 10^{-3}$
3453	$16\pi/\Omega$	400	0.9	0.06	$(2.50 \pm 0.00) \times 10^{-3}$	$(1.22 \pm 0.75) \times 10^{-8}$	$(2.29 \pm 1.58) \times 10^{-4}$	$(3.02 \pm 0.46) \times 10^{-2}$
3448	0	400	0.3	0.06	$(2.50 \pm 0.00) \times 10^{-3}$	$(3.05 \pm 2.55) \times 10^{-13}$	$(4.29 \pm 2.47) \times 10^{-7}$	$(2.22 \pm 0.52) \times 10^{-3}$
3449	$16\pi/\Omega$	400	0.3	0.06	$(2.29 \pm 2.53) \times 10^{-1}$	$(1.43 \pm 1.71) \times 10^{-1}$	$(4.61 \pm 4.95) \times 10^{-2}$	$(1.39 \pm 0.90) \times 10^1$
3436	0	400	0.3	0.02	$(2.50 \pm 0.00) \times 10^{-3}$	$(9.13 \pm 12.07) \times 10^{-13}$	$(1.20 \pm 1.54) \times 10^{-7}$	$(3.43 \pm 2.16) \times 10^{-4}$
3437	$16\pi/\Omega$	400	0.3	0.02	$(2.50 \pm 0.00) \times 10^{-3}$	$(2.39 \pm 1.08) \times 10^{-9}$	$(8.02 \pm 6.85) \times 10^{-5}$	$(1.17 \pm 0.23) \times 10^{-2}$
3432	0	400	0.1	0.02	$(2.50 \pm 0.00) \times 10^{-3}$	$(9.55 \pm 12.38) \times 10^{-13}$	$(8.32 \pm 8.82) \times 10^{-8}$	$(2.91 \pm 1.54) \times 10^{-4}$
3433	$16\pi/\Omega$	400	0.1	0.02	$(2.00 \pm 2.42) \times 10^{-1}$	$(1.14 \pm 1.50) \times 10^{-1}$	$(3.54 \pm 4.61) \times 10^{-2}$	$(1.23 \pm 0.98) \times 10^1$
								$\} \triangle$
3372	0	3200	1.0	0.2	$(1.11 \pm 0.62) \times 10^{-1}$	$(5.22 \pm 2.79) \times 10^{-2}$	$(1.39 \pm 0.68) \times 10^{-2}$	$(1.58 \pm 0.31) \times 10^1$
3373	$16\pi/\Omega$	3200	1.0	0.2	$(1.00 \pm 0.41) \times 10^{-1}$	$(4.29 \pm 1.61) \times 10^{-2}$	$(9.90 \pm 3.04) \times 10^{-3}$	$(1.52 \pm 0.24) \times 10^1$
3460	0	3200	0.9	0.06	$(3.12 \pm 0.00) \times 10^{-4}$	$(3.02 \pm 1.86) \times 10^{-12}$	$(4.68 \pm 2.21) \times 10^{-7}$	$(1.89 \pm 0.39) \times 10^{-3}$
3461	$16\pi/\Omega$	3200	0.9	0.06	$(3.35 \pm 0.24) \times 10^{-4}$	$(9.82 \pm 10.64) \times 10^{-6}$	$(3.36 \pm 3.24) \times 10^{-5}$	$(5.07 \pm 2.78) \times 10^{-2}$
3456	0	3200	0.3	0.06	$(3.12 \pm 0.00) \times 10^{-4}$	$(3.02 \pm 1.86) \times 10^{-12}$	$(4.68 \pm 2.21) \times 10^{-7}$	$(1.89 \pm 0.39) \times 10^{-3}$
3457	$16\pi/\Omega$	3200	0.3	0.06	$(1.19 \pm 0.48) \times 10^{-1}$	$(5.44 \pm 1.88) \times 10^{-2}$	$(1.42 \pm 0.51) \times 10^{-2}$	$(1.65 \pm 0.26) \times 10^1$
3444	0	3200	0.3	0.02	$(3.12 \pm 0.00) \times 10^{-4}$	$(8.60 \pm 6.12) \times 10^{-13}$	$(5.18 \pm 2.54) \times 10^{-7}$	$(1.55 \pm 0.35) \times 10^{-3}$
3445	$16\pi/\Omega$	3200	0.3	0.02	$(9.38 \pm 4.06) \times 10^{-2}$	$(4.50 \pm 1.88) \times 10^{-2}$	$(1.15 \pm 0.46) \times 10^{-2}$	$(1.29 \pm 0.27) \times 10^1$
3440	0	3200	0.1	0.02	$(3.12 \pm 0.00) \times 10^{-4}$	$(8.60 \pm 6.12) \times 10^{-13}$	$(5.18 \pm 2.54) \times 10^{-7}$	$(1.55 \pm 0.35) \times 10^{-3}$
3441	$16\pi/\Omega$	3200	0.1	0.02	$(8.15 \pm 3.91) \times 10^{-2}$	$(3.79 \pm 1.70) \times 10^{-2}$	$(1.05 \pm 0.50) \times 10^{-2}$	$(1.41 \pm 0.23) \times 10^1$
								$\} \triangle$

Table 3.4. (continued)

Chapter 4

Lightning Morphology and Implication for Observations

4.1 Multi-dimensional Simulations of Disk Lightning Propagation

4.1.1 The Two-dimensional Model for Disk Lightning

Now that I have studied the one-zone behavior of the dust plasma. Then, the natural question arises next is “how does the lightning look like?” To answer this question and to provide quantitative predictions such as event ratio, energy spectrum and morphology of the lightning, I must combine the dust-plasma model with fluid models that depict the protoplanetary disk. I am now on the way to do this, by combining the analytic solutions (Equations (2.110), (2.112)–(2.114) with computational magnetohydrodynamic simulations. As the purpose of this thesis is concerned, it is important to focus on the minimalistic model that reproduces the lightning morphology. Therefore, I constructed a two-dimensional disk lightning model and conducted a series of simulations, on which I focus in this chapter.

Figure 4.2 illustrates the two-dimensional model of the $\phi - z$ slice of the disk. Two fluids are treated separately: one is the gas component coupled with small dust, the other is large dust. Gravity is towards the equatorial plane. Initial velocity shear is given to cause Kelvin-Helmholtz instability. Thus shear velocity is given, rather than self-maintained, for simplicity.

Here, I solve the following set of equations of resistive MHD:

$$\frac{\partial \rho_g}{\partial t} + \nabla \cdot (\rho_g \mathbf{u}_g) = 0, \quad (4.1)$$

$$\frac{\partial \rho_g \mathbf{u}_g}{\partial t} + \nabla \cdot (\rho_g \mathbf{u}_g \otimes \mathbf{u}_g - \mathbf{B} \otimes \mathbf{B}) + \nabla P = 0, \quad (4.2)$$

$$\frac{\partial \mathbf{B}}{\partial t} + c \nabla \times \mathbf{E} = 0, \quad (4.3)$$

$$\frac{\partial e}{\partial t} + \nabla \cdot ((e + P) \mathbf{u}_g + \mathbf{E} \times \mathbf{B}) = 0, \quad (4.4)$$

where the independent variables are ρ_g : density, $\rho_g \mathbf{u}_g$: momentum density, \mathbf{B} :magnetic

4.1. MULTI-DIMENSIONAL SIMULATIONS OF DISK LIGHTNING PROPAGATION

field, and e : energy density. The degree of freedom is 7 due to a constraint from Maxwell's equation

$$\nabla \cdot \mathbf{B} = 0. \quad (4.5)$$

Other variables, such as \mathbf{J} : electric current, \mathbf{E} : electric field, P : gas pressure etc. in the framework of MHD are rewritten as follows:

$$\mathbf{J} = \nabla \times \mathbf{B}, \quad (4.6)$$

$$\mathbf{E} = -\mathbf{u}_g \times \mathbf{B} + \eta \mathbf{J}, \quad (4.7)$$

$$P = (\gamma - 1)(e - \frac{1}{2}\rho_g u^2 - \frac{1}{2}B^2), \quad (4.8)$$

where γ is the ratio of specific heats and η is the magnetic resistivity. I used multidimensional mesh-based MHD code “ATHENA” (Gardiner & Stone, 2005, 2008), and modified the code for our purpose, by adding magnetic resistivity, advected dust, and discharge models.

Advecting scalar fields $S[i]$ can be easily added to this model:

$$\frac{\partial S[i]}{\partial t} + \nabla \cdot (S[i] \mathbf{u}_g) = 0. \quad (4.9)$$

I add two scalar fields: $S[0]$ is the number density of the larger dust, and $S[1]$ is the non-equilibrium ionization degree. $S[0]$ is to generate the electric field, and $S[1]$ is to calculate the magnetic resistivity η , and therefore explaining the tree-shape of the lightning. The specific equations for the scalar fields are:

$$\frac{\partial S[0]}{\partial t} + \nabla \cdot (S[0](\mathbf{u}_g + \mathbf{u}_{grav}(r))) = 0, \quad (4.10)$$

$$\frac{\partial S[1]}{\partial t} + \nabla \cdot (S[1]\mathbf{u}_g - D_1 \nabla S[1]) + \frac{S[1] - S_{eq}[1]}{\tau_1} = \delta_{discharge}. \quad (4.11)$$

Large dust advects while falling at the terminal velocity $\mathbf{u}_{grav}(r)$. The ionization field rises suddenly at lightning path given by the discharge model; then it advects, diffuses with diffusion coefficient D_1 , and rapidly decays with timescale τ_1 to equilibrium value $S_{eq}[1]$.

Finally, I describe our numerical discharge model (cf. Figure 4.1) based on the lightning model by Solomon et al. (2002). I assume that the dust plasma is in (c)charge-up phase: Electric field is dominated by ηj term. I also assume that the lightning propagation timescale is negligibly small compared to the hydrodynamic timescale. So the process described in the following is performed at each timestep of the magneto-hydrodynamic simulations, taking the magneto-hydrodynamic fields as backgrounds.

1. Introduce a pair of “lightning leader” packet ($q = \pm 1$) at every mesh when it satisfies $E' > E_{crit}$. Here q is the sign of the electric charge carried by the leader.
2. Each lightning leader random-walks to one of its Moore neighborhood. They obey electric field and prefers the highly ionized mesh. The probability $P(\mathbf{n})$ is chosen so that the direction \mathbf{n} satisfies

$$P(\mathbf{n}) \propto \exp(-qS[1]^{0.5} \frac{\mathbf{n} \cdot \mathbf{E}'}{|E'|}), \quad (4.12)$$

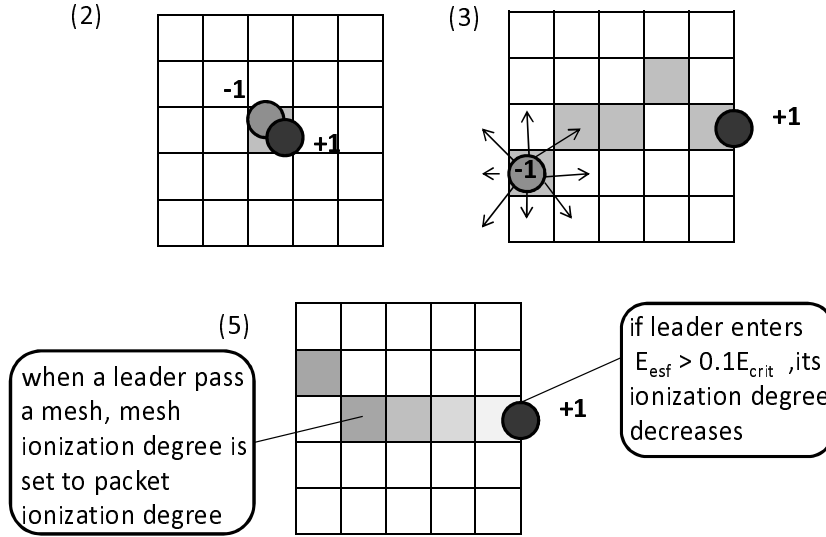


Figure 4.1. The model for lightning leader propagation.

where expone is a function such that $\text{expone}(x) = x$ for $x > 0$ and $\text{expone}(x) = \exp(x)$ otherwise.

3. Initially, leader packet has ionization degree $S[1] = 1.0$
4. At each mesh the lightning leader passes, mesh ionization degree is set to the leader ionization degree. Leader ionization is updated as

$$S[1] \leftarrow S[1] \times \min(1.0, \frac{|E'|}{0.1E_{crit}}). \quad (4.13)$$

Lightning leader packet can survive as long as $|E'| > 0.1E_{crit}$. This is a result of the avalanche discharge model; once generated, lightning leader can maintain the ionizing process even if the electric field is substantially lower than the critical value ($|E'| < E_{crit}$).

5. If the leader ionization degree is smaller than the mesh ionization degree, remove the leader packet.

The simulation takes place in the 2-dimensional plane as in Figure 4.2, supposed to be a section of a protoplanetary disk. The horizontal and vertical coordinates are labeled x and y , respectively, and are in the range $0 \leq x < 1$, $-1 \leq y \leq 1$. The boundary conditions are periodic in the x direction and outflowing in the y direction, respectively.

$$\rho_g = \begin{cases} 1 & \text{if } |y| \geq 0.25 \\ 2 & \text{if } |y| < 0.25, \end{cases} \quad (4.14)$$

$$\mathbf{u}_g = \begin{cases} (1, 0) & \text{if } |y| \geq 0.25 \\ (-1, 0) & \text{if } |y| < 0.25, \end{cases} \quad (4.15)$$

$$c_s = \sqrt{\frac{\gamma P}{\rho_g}} = 1. \quad (4.16)$$

Finally, $D_1 = 1.0$ and $\tau_1 = 0.1$ in the nondimensional unit of the simulation.

4.1.2 The Simulation Result

The time evolution for this model is depicted by frames in Figure 4.3. As time goes by; (1,2): The Kelvin-Helmholtz instability initiates and develops; (3): The first lightning takes place; (4,5,6): As the large dust sediments, its number density is increased and the lightning events become gradually dense and frequent; (7,8): At the late phase, a lot of lightning takes place in parallel; (9): At the final phase, the dust layer become thin and ionization degree is maintained high, so the lightning become few and powerless.

Although many things are left to do in this simulations to reach reality — the turbulence is initial condition driven instead of self-maintained, set of parameters are deliberately chosen values from the range plausible for protoplanetary disks — the computer program used here demonstrates the possibility of, and can actually used in, future studies of protoplanetary disk lightning, for its morphology, event rate and energy spectrum.

4.2 Implication for Observations

In chapter 2, I have assumed a uniform region in a protoplanetary disk and expressed the dust charge Q_i , and the generated electric field E' , as functions of dust number density \mathcal{N} , dust radius r_s , r_L and fractal dimension D_s , D_L . In turn, I calculated the critical number density $\mathcal{N}_{\text{crit}}$ at which lightning strikes as functions of dust parameters r_s , r_L , D_s and D_L .

In chapter 3, I have modeled the electrostatic discharge as a nonlinear Ohmic resistivity, and have shown the existence of the regions in the protoplanetary disks where the major portion of the disk accretion energy is consumed in the discharge part of the resistivity law. I have introduced the work-heat balance model to explain the upper limit for the energy budget of the lightning.

Based on these knowledge, I have put a hand to studies of the morphology of the disk lightning. We now know that both the dust-dust collisional charge separation and the resistive MRI contribute to protoplanetary disk electromagnetism by creating new phases of the dust-plasma, and that disk lightning is plausible. In the following sections I elucidate what astronomical observation features disk lightning may provide.

4.2.1 Energetics and Direct Observations

It is out of the reach of today's science to model the lightning in protoplanetary disks in detail. This is not just because of the large ambiguity left in the lightning model in the

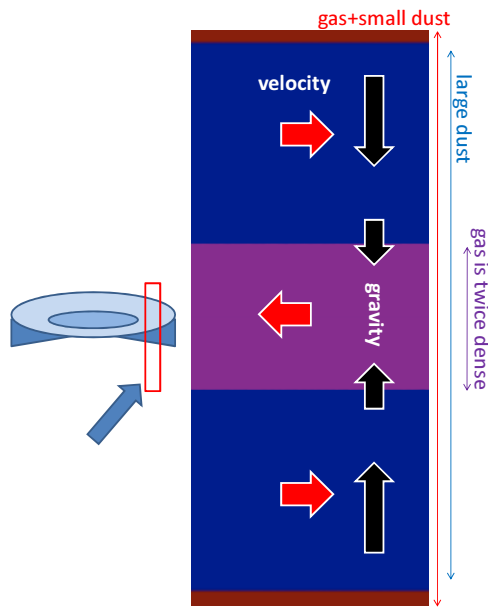


Figure 4.2. The two dimensional model of the cross section of the the protoplanetary disk.

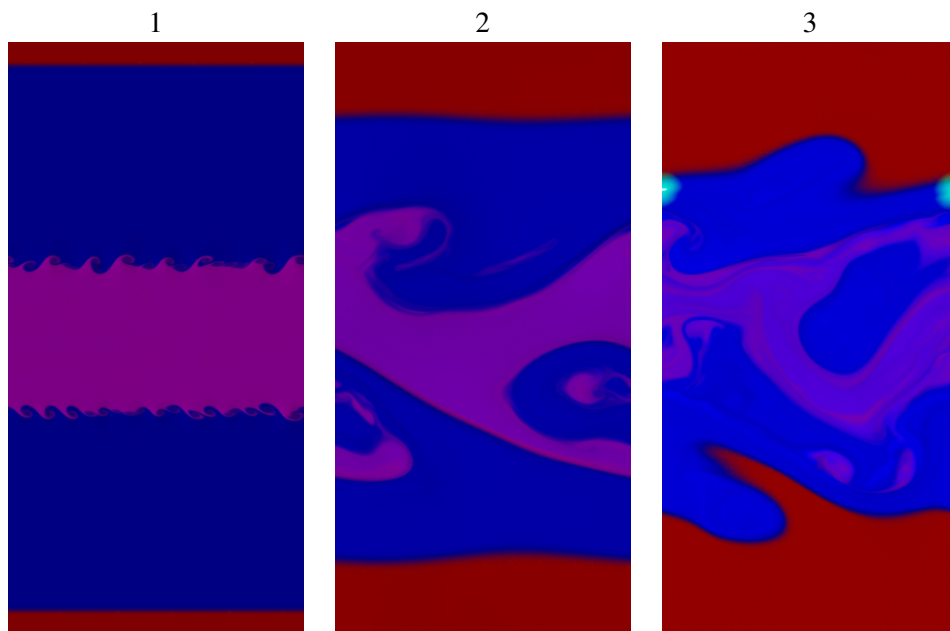
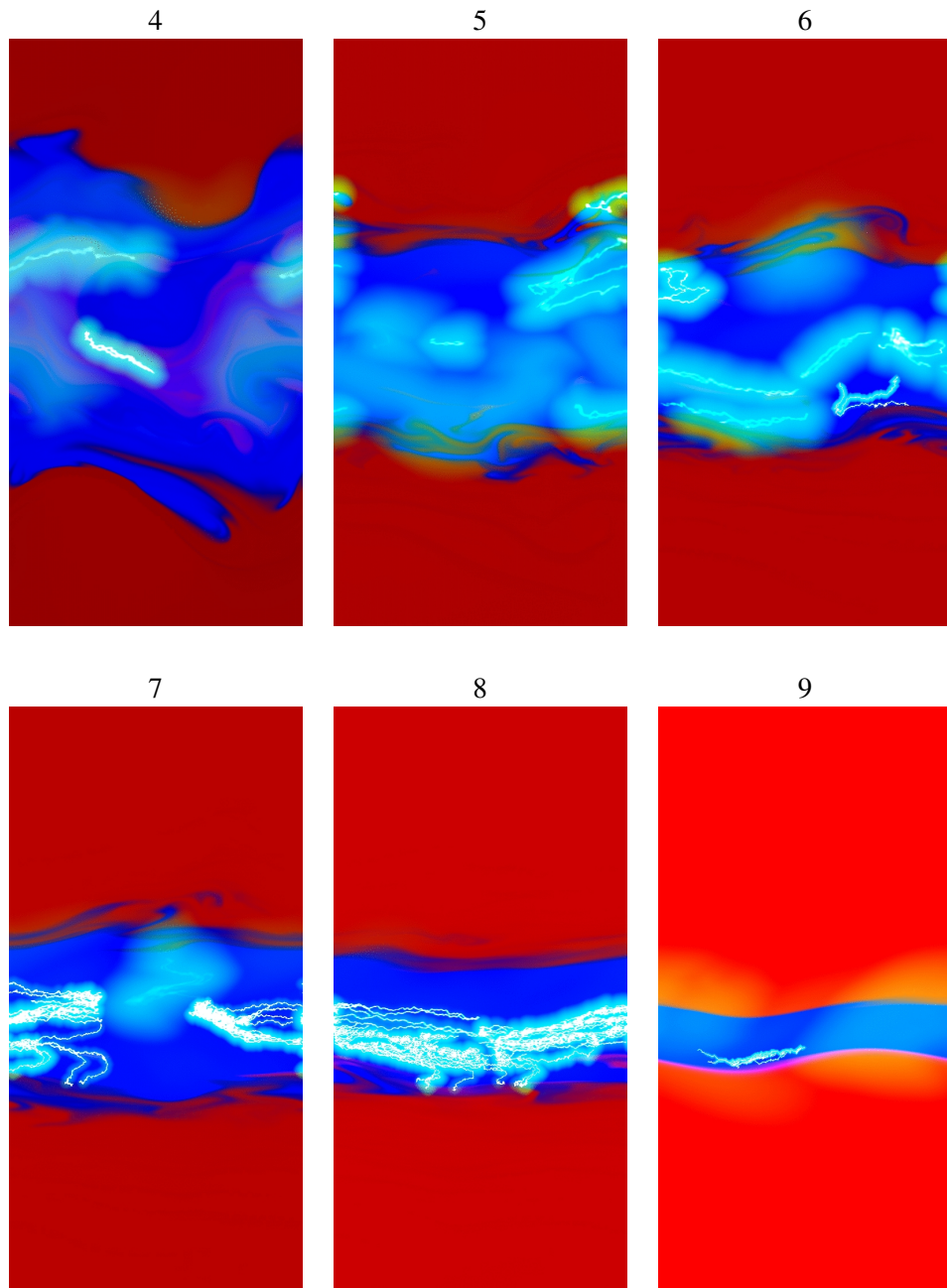


Figure 4.3. The two-dimensional simulation of the disk lightning coupled with dust sedimentation and Kelvin-Helmholtz instability. This result was first presented in Wood (2011).



protoplanetary disk, or because of the lack of numerical resolution. The diversity of lightning phenomena observed on Earth must be kept in mind. Therefore, in this section I limit myself to one lightning model in a typical setting in the protoplanetary disk and resort to the order-of-the-magnitude argument. However, we are not completely left clueless; the mean free path, electron velocity and the critical electric field can be well-estimated based on physics and the property of the disk; other quantity can be analogically inferred from the terrestrial lightning.

I estimate the total energy of a lightning event in a protoplanetary disk at $r = 2.7$ au where the snowline is located in the MMSN model. For MMSN, the number density of the gas is $4.7 \times 10^{13} \text{ cm}^{-3}$ in this region. The typical electron mean free path at this site is $l_{mfp} \simeq 1.2 \times 10^2 \text{ cm}$. By equation (2.77) the critical electric field is known to be $E_{\text{crit}} \simeq 4.3 \times 10^{-4} \text{ G}$. The sphere with radius of the disk scale-height $h \simeq 2.4 \times 10^{12} \text{ cm}$ contains the electric energy $W \equiv E_{\text{crit}}^2 / 8\pi \times 4\pi h^3 / 3 \simeq 4.3 \times 10^{29} \text{ erg}$. When the lightning strikes, the energy is concentrated into lightning bolt of radius w and length h , where w is related to l_{mfp} by $w \simeq 5000 l_{mfp} \simeq 6.0 \times 10^5 \text{ cm}$ (Pilipp et al., 1992). The duration of the event is estimated as h/v_e , which is of the order of 10^4 s . Assuming the balance between the heating and black body radiation in the lightning bolt, the temperature of the heated gas will be about 800 K. This is in agreement with the temperature and the timescale the chondrule have been processed; see e.g. Desch & Connolly Jr (2002) and references therein.

The ultimate energy source for collision-induced lightning is the gravitational energy of the accreting matter. In our model the mass accretion rate of uncondensed larger dust is $\dot{M} = 2\pi r \Sigma_L^\infty u_L \simeq 3.3 \times 10^{17} \text{ g sec}^{-1}$. The gravitational energy released within condensation region h is $L \equiv GM_\odot \dot{M} h r^{-2} \simeq 6.6 \times 10^{28} \text{ erg sec}^{-1}$. For the largest energy event $W = 4.3 \times 10^{29} \text{ erg}$ the upper limit of the event rate is $1.5 \times 10^{-1} \text{ sec}^{-1}$.

The energy budget for the MRI-induced lightning might be even larger. The luminosity due to gravitational energy released from the matter accreting from $r+h$ to $r-h$ is estimated as $L \equiv 2GM_\odot M^\infty h / r^2 t^\infty \simeq 7.7 \times 10^{29} \text{ erg sec}^{-1}$, which is an order of magnitude larger than the collision-induced lightning. Here, $M^\infty = 0.01M_\odot$ is the protoplanetary disk total mass and $t^\infty = 10^6$ year is the disk age. However, the MRI-induced lightning model also suggests that only portion of the matter at $|z/H| > 2$ take part in the sustained zone of the MRI. According to the vertical hydrostatic equilibrium, the zones involve about 9% of the total mass in the section. It is therefore reasonable to consider that the energy budget is scaled by the same ratio.

Low Frequency Radio Waves

The charge density evolution, electromagnetic pulse, and electromagnetic waves accompanying lightning in terrestrial thunderclouds are observed (e.g. Koshak & Krider, 1989; Lin et al., 1979). The typical wavelength of the electromagnetic waves is similar to the scale height of the thundercloud. These are called extremely low frequency waves. The electromagnetic waves from lightning can be basically modeled as solutions of Maxwell equations, including lightning current as a source term (e.g. Rakov & Uman, 1998). These models, applied to the protoplanetary discs, predict that the electromagnetic wave spectrum extends between the event duration and light crossing time of the system, or

$$9.6 \times 10^{-5} \sim 1.2 \times 10^{-2} \text{ Hz.}$$

This frequency range is at least two orders of magnitude lower than any frequencies with established observational methods. The term ‘Astronomically Low Frequency (ALF) waves’ is coined by Muranushi (2010) for such waves, as the successor to the list of the names ‘very low frequency (*VLF*)’, ‘ultra low frequency(*ULF*)’, ‘super low frequency (*SLF*)’, and ‘extremely low frequency (*ELF*).’ The frequency is so low that an astronomical budget is needed to build an astronomically large detector, considering its wavelength of order of an astronomical unit.

There is almost no absorption by the gas molecules as well as dust for such low frequencies, and main obstacle for the propagation of such low frequency waves is the plasma. Assuming the number density $n \sim 5 \times 10^{-3} \text{ cm}^{-3}$ and the ionization degree 50% of the nearby interstellar medium (ISM) (Cox & Reynolds, 1987), its plasma frequency is about 1.3 kHz. Electromagnetic waves with frequency less than this plasma frequency cannot propagate in the plasma. Unless there is some efficient conversion mechanism between ALF waves and magnetohydrodynamic modes, it is difficult for the ALF waves to propagate out of the proximity of the protoplanetary disk. On the other hand, much higher frequency radio waves, produced by smaller-scale lightning structure, propagates through the ISM, and are easier to observe. Terrestrial and space-bound radio wave detectors are limited at around 10 MHz (Roettgering, 2003) and 30 MHz (Jones et al., 2000), respectively, which are plasma frequencies of the Earth ionosphere and the heliopause, respectively. On the other hand *Voyager* spacecrafts have practically accomplished detection of 1 – 3 kHz radio emission outside the heliopause (Kurth et al., 1984), so direct observation above the ISM plasma frequency is at least technically viable. Below the ISM plasma frequency observers may deploy indirect measures (Lacki, 2010).

Infrared (IR) Observations

The energy of the lightning contributes to the local heating of the protoplanetary discs, which might be resolved by advanced telescopes such as Atacama Large Millimeter Array (*ALMA*). Assuming the total energy W and the event duration 10^4 s mentioned above, the distance to the disk 100 pc, and observation band of 211 – 275 GHz, the spectral flux density will be 1.7 Jy, which is well above 0.1 mJy, the proposed sensitivity of *ALMA* at this band (Baudry, 2008). If the efficiency of the lightning for converting the buget W into this band is greater than 10^{-4} , protoplanetary disk lightning will be an interesting observational candidate in *ALMA*.

The most possible observational evidence is excess of heating near the snowline or sustained MRI zone. To distinguish the cause of the heating with other heating model candidates, the variability or correlation function of the heating might be useful. This is because lightning propagates at the speed of ionized electrons, which is much faster than the speed of sound.

It is worth noting that the lightning electric field will also accelerate the ionized molecules. The mean free path, determined mainly due to the collision against neutral molecules, will approximately be the same for the electrons and the molecules. Therefore especially, monovalent ions, both cations and anions, will gain about the same energy $e E l_{\text{mfp}}$ due to the static field acceleration. This is equivalent to $4 \times 10^6 \text{ cm/s}$ or 40 km/s

for a hydrogen molecule. Such high velocity is difficult to expect from any thermal or hydrodynamic processes. Therefore, if such velocity shifts are observed by the line measurements, it will strongly suggest the existence of the nonthermal acceleration processes.

Ultraviolet (UV) Observations

The ionization electrons of the lightning excite various electron levels in gas molecules and dust. There is possibility of observing fluorescence photons from such excited molecules. Although the disk gas is generally expected to be thick for ultraviolet photons, there are categories of lightning that extends toward thin regions of the gas, known as sprites and elves (e.g. Williams, 2001). The sprites and elves are phenomena similar to lightning observed in the mesosphere of the earth, possibly caused by electric fields induced by the thunderclouds. Fluorescence lines from such regions can be observed by future ultraviolet missions like *THEIA* (Spergel et al., 2009). Also, some of the chemical reaction models constructed to explain the protostellar and protoplanetary observations are experiencing either lack or excess of estimated *UV* radiation (e.g. Nomura & Millar, 2005; Chapillon et al., 2008; Pérez et al., 2008; Herczeg & Hillenbrand, 2008). If excess of *UV* photons is required to the model, it might be from the sprite discharges and elves from the surface of the protoplanetary discs; on the other hand if the chemical composition model require more *UV* photons than is observed, lightning hidden in the disk mid-plane might be providing them.

High Energy Photons

Detection of burst-like gamma-ray is reported from terrestrial thunder clouds, by ground based (Tsuchiya et al., 2007; Enoto et al., 2008) and spacecraft (Inan et al., 2006) observations. The burst precedes a cloud-to-ground lightning, lasts for ~ 40 seconds, extends to 10 MeV. The spectrum can be interpreted as consisting of bremsstrahlung photons from relativistic electrons. These relativistic electrons are secondary electrons generated by cosmic rays, and accelerated by the electric fields through process known as avalanche amplification (Roussel-Dupré & Gurevich, 1996).

If a charged particle is accelerated by the protoplanetary thundercloud through similar process, its kinetic energy reaches $eEh \simeq 3.1 \times 10^{11}$ eV. Synchrotron radiation from such electrons assuming $B = 6$ G has characteristic frequency $\omega_c = 5.5 \times 10^{19}$ Hz, which means that the power spectrum of the synchrotron emission will peak at $\hbar\omega = 1.0 \times 10^4$ eV. This is in the bandwidth of the high energy X-ray telescopes such as INTEGRAL and Suzaku. Assuming the E^{-1} power law spectrum (Dwyer & Smith, 2005) with cutoff at 10 keV, protoplanetary disk lightning is an interesting observational target for X-ray telescopes.

4.2.2 Implication on Chondrule Formations

In §2.1.1, I introduced chondrule and its formation, and addressed four problems against explaining the chondrule formation by lightning.

This work can provide counter-argument for all of the problems. For the energetics problem, the collisional lightning model suggests that the larger dust and the gas (containing smaller dust that are coupled to the gas) are now harnessed by electric field. Outgoing

gas is not free in carrying the gravitational energy away; instead the gas converts its gravitational energy into electric field energy, fully contributing to lightning. For the neutralization problem, I have shown in this work that with reasonably high dust number density η , the dust-dust charge separation can dominate over the plasma neutralization, and the electrostatic field can grow up to critical value.

Lightning due to self-sustainment of the MRI shares the arguments above. The energy budget of the MRI-induced lightning is $0.1 \sim 10$ times that of the collision-induced lightning as is estimated in the previous section. In addition to that, MRI-induced lightning does not suffer from the neutralization problem, because the model does not involve dust as the charge separating agent.

Thus, lightning induced by collisional charging of water ice dust overcomes the energetics problem (Chapter 2), but if applied as the chondrule heating source, it would suffer from the redox environment mismatch (Section 2.1.1). However, the lightning induced by self-sustained MRI is a result of pure MHD process, and thus is redox-neutral. Therefore, it can potentially explain chondrule heating in both reducing and oxidizing environment.

For the destruction problem, I point out that in Güttler et al. (2008)'s experiment, either the electron mean free path is by many orders of magnitude shorter, or the electron kinetic energy is much larger than those in the protoplanetary-disk environment. They used air at pressures between 10 and 10^5 Pa. Air consists of 78 per cent nitrogen, 21 per cent oxygen, and 1 per cent argon. Their molecular van der Waals radii are 1.6×10^{-8} cm, 1.5×10^{-8} cm, and 1.9×10^{-8} cm, respectively (Bondi, 1964). Therefore, the electron mean free path and the electron kinetic energy, $W_e = e E l_{\text{mfp}}$, was $l_{\text{mfp}} \sim 4.8 \times 10^{-1}$ cm, $W_e = 1.6 \times 10^4$ eV for 10 Pa case, and $l_{\text{mfp}} \sim 4.8 \times 10^{-5}$ cm, $W_e = 1.6$ eV for 10^5 Pa case, respectively. On the other hand in protoplanetary discs, typical mean free path and electron kinetic energy are $l_{\text{mfp}} = 1.2 \times 10^2$ cm, and $W_e = 15.4$ eV.

It might be possible that protoplanetary-disk lightning is effective in melting dust aggregates, although experimental lightning is ineffective in heating and led to disruption of the dust, due to shorter mean free path or higher energy electron. The minimum size of the structures that electron can form is of order of its mean free path. If the electron mean free path is much shorter than the dust aggregates, as in 10^5 Pa case, the electron current may concentrate on the most conductive part of the dust aggregate, leading to partial heating and explosion of the dust. On the other hand if the electron is much more energetic, as in 10 Pa case, it may react differently on dust monomers.

To reproduce the mean free path and electron energy simultaneously, one must reproduce the electric field strength $E = 4.3 \times 10^{-4}$ G of protoplanetary discs; while the electric field used in the experiment $E = 1.1 \times 10^2$ G was much stronger. This much stronger electric field itself might be the cause of dust aggregate dissociation, due to much stronger electric force exerted on electron-absorbed dust monomers. Also the discharge time-scale in the experiment was much smaller than that in the protoplanetary discs, which might have led to the catastrophic results. The effect of lightning on dust aggregate within protoplanetary-disk environment has yet to be confirmed in future experiments and simulations.

Chapter 5

Summary and Future Prospect

5.1 Summary

I have discussed several new aspects of planet formation theory, when dust charge and electrostatic discharge are taken into account. The dust charge brought by plasma absorption may drastically alter the planet formation scenario at its beginning; the planet formation is not in-place nor homogeneous. Instead, planet seeds migrate all across the protoplanetary disk to grow up. Furthermore, charge brought in by dust-dust collision has an important effect. It has non-negligible effect on the charge state of the dust and the plasma, and at certain environments, it may cause lightning in protoplanetary disks. We are now ready to study the disk lightning quantitatively. If such astronomical lightning takes place and one day is observed, it will tell us unique information on the mysterious magnetodynamics of the protoplanetary disks.

In chapter 2 I described the dust-dust collisional charging in protoplanetary disks. I showed that in modern theories of dust density enhancement and dust fluffiness considered, dust-dust collisional charging becomes an important process in determining the charge state of dust and gas. I solved the charge equilibrium equations for various disk environments and dust number density \mathcal{N} . I presented analytic formulae to determine the dust charge state, plasma phase and necessary condition of \mathcal{N} for lightning to take place. Since they are in analytic forms, they can be easily applied to many disk models.

I showed that as dust number density \mathcal{N} is increased the dust-plasma experiences four distinct phases, at each of which different charge carrier and charge exchange process dominates. The latter two phases are the results of the dust-dust collisional charging taken into account. As a result of the rapid voltage rise in these charge-up phases, collisional charging induced lightning is possible at $\mathcal{N} < 100$, or equal mass of dust and gas per volume. Such level of dust condensation is considered to be not difficult to be achieved in protoplanetary disk environment.

In chapter 3 I studied the interaction of the magnetorotational instability (MRI) with the electric discharge caused by the electric field in the resistive MHD. I found the self-sustainment of the MRI in spite of the high resistivity. The instability gives rise to the large electric field that causes the electrical breakdown, and the breakdown maintains the high ionization degree required for the instability.

I found that the condition for this self-sustained MRI is set by the balance between the

energy supply from the shearing motion and the energy consumed by the Ohmic dissipation. I applied the condition to various disk models and located the volume of the disk occupied by this form of lightning.

In chapter 4 I simulated the morphology of the lightning in protoplanetary disk, and estimated the total energy, intensity and event rate of such discharges events. I discussed the possibility of observing lightning and sprite discharges in protoplanetary discs by low frequency radio waves, *IR* images, *UV* lines, and high energy X-rays. I also discussed the effects of lightning on chondrule heating, planetesimal growth and magnetorotational instability of the disk.

5.2 Future Prospect

In this thesis, global configuration of the protoplanetary disk and the time evolution of them are treated as pre-defined background model. In reality, the magnetorotational instability discussed in this thesis is the primal agent of angular momentum transport, and taking the back-reaction of MRI into accretion process is the next important step in this field. Simultaneous treatment of the global accretion process and the local accretion, along with dust evolution is necessary to close the circle in Figure 1.4.

Another direction of this work to be extended is to incorporate the discharge model in more detail. Physics of gas discharge has profound research history based on both theoretical and industrial interest. The current-voltage relation of the gas under electrostatic field shows much more profound features than the simple nonlinear model assumed in this paper (see Equations (3.1) and (3.2)), that includes avalanche discharge, glow discharge, ark discharge and many transitional phenomena (Druyvesteyn & Penning, 1940; Gallo, 1975).

Three-dimensional simulations of global disk with MRI resolved have been possible recently (Dzyurkevich et al., 2010; Sorathia et al., 2011; Flock et al., 2012; Gaburov et al., 2012; Romanova et al., 2012) but it will take decades of progress in computation capability to simulate the entire history of a protoplanetary disk and planet formation, with lightning resolved. In addition to such bottom-up approaches from the elementary processes, it is necessary to take a complementary, top-down approach that works without the encompassing knowledge of the internal states and initial conditions, as is practiced in the field of weather forecast. I will search for a way to construct observationally meaningful predictions within practical computer resources and time, by combining the related processes in a uniting statistic model, and by distributing the uncertainty among the processes according to their importance and our level of understanding.

It poses a great challenge on physics to consistently explain the rich hydrodynamic, magnetic, electric processes that takes place in protoplanetary disks from basic laws of physics, and to compare the predictions with observations. Lightning signal from outer space is a unique clue from the enigmatic electromagnetic hurricane, the birthplace of the planets, including the one that we live on.

Bibliography

- Alexander R. D., Clarke C. J., Pringle J. E., 2006a, Monthly Notices of the Royal Astronomical Society, 369, 216
- Alexander R. D., Clarke C. J., Pringle J. E., 2006b, Monthly Notices of the Royal Astronomical Society, 369, 229
- Balbus S. A., Hawley J. F., 1991, The Astrophysical Journal, 376, 214
- Balbus S. A., Hawley J. F., 1998, Reviews of Modern Physics, 70, 1
- Baudry A., 2008, in 2nd MCCT-SKADS Training School. Radio Astronomy: Fundamentals and the New Instruments Vol. 1, The ALMA radio telescope. p. 2
- Blum J., Wurm G., 2000, Icarus, 143, 138
- Blum J., Wurm G., 2008, Annual Review of Astronomy and Astrophysics, 46, 21
- Bondi A., 1964, J. Phys. Chem., 68, 441
- Borucki W. J., Magalhaes J. A., 1992, Icarus, 96, 1
- Brauer F., Dullemond C. P., Henning T., 2008, A&A, 480, 859
- Brauer F., Henning T., Dullemond C. P., 2008, Astronomy and Astrophysics, 487, L1
- Chapillon E., Guilloteau S., Dutrey A., Piétu V., 2008, A&A, 488, 565
- Christian H., Holmes C. R., Bullock J. W., Gaskell W., Illingworth A. J., Latham J., 1980, The Quarterly Journal of the Royal Meteorological Society, 106, 159
- Cieza L., Padgett D. L., Stapelfeldt K. R., Augereau J.-C., Harvey P., Evans N. J., Mern B., Koerner D., Sargent A., van Dishoeck E. F., Allen L., Blake G., Brooke T., Chapman N., Huard T., Lai S.-P., Mundy L., Myers P. C., Spiesman W., Wahhaj Z., 2007, The Astrophysical Journal, 667, 308
- Clayton R. N., Mayeda T. K., Gooding J. L., Keil K., Olsen E. J., 1981, in Lunar and Planetary Institute Science Conference Abstracts Vol. 12, Redox processes in chondrules and chondrites. p. 154 – 156
- Connolly H. C., Hewins R. H., Ash R. D., Zanda B., Lofgren G. E., Bourot-Denise M., 1994, , Published online: 08 September 1994; | doi:10.1038/371136a0, 371, 136

- Cox D. P., Reynolds R. J., 1987, Annual Review of Astronomy and Astrophysics, 25, 303
- Cuzzi J. N., Zahnle K. J., 2004, ApJ, 614, 490
- Dash J., Mason B., Wetzlauer J., 2001, Journal of Geophysical Research, 106, 20395
- Desch M. D., Kaiser M. L., 1990
- Desch S. J., Connolly Jr H. C., 2002, Meteoritics and Planetary Science, 37, 183 – 207
- Desch S. J., Cuzzi J. N., 2000, Icarus, 143, 87
- Druyvesteyn M. J., Penning F. M., 1940, Reviews of Modern Physics, 12, 87
- Duley W. W., Williams D. A., 1984, Interstellar chemistry
- Dwyer J. R., Smith D. M., 2005, Geophysical Research Letters, 32
- Dzyurkevich N., Flock M., Turner N. J., Klahr H., Henning T., 2010, Astronomy and Astrophysics, 515, 70
- Enoto T., Tsuchiya H., Yamada S., et al. 2008, in International Cosmic Ray Conference Vol. 1 of International Cosmic Ray Conference, Detection of gamma-rays from winter thunderclouds along the coast of Japan Sea. pp 745–748
- Fischer G., Desch M. D., Zarka P., Kaiser M. L., Gurnett D. A., Kurth W. S., Macher W., Rucker H. O., Lecacheux A., Farrell W. M., 2006, Icarus, 183, 135 – 152
- Fleming T. P., Stone J. M., Hawley J. F., 2000, The Astrophysical Journal, 530, 464
- Flock M., Dzyurkevich N., Klahr H., Turner N., Henning T., 2012, The Astrophysical Journal, 744, 144
- Fujii Y. I., Okuzumi S., Inutsuka S., 2011, The Astrophysical Journal, 743, 53
- Gaburov E., Johansen A., Levin Y., , 2012, Magnetically-levitating disks around supermassive black holes
- Gallo C. F., 1975, IEEE Transactions on Industry Applications, IA-11, 739
- Gammie C. F., 1996, The Astrophysical Journal, 457, 355
- Gardiner T. A., Stone J. M., 2005, Journal of Computational Physics, 205, 509
- Gardiner T. A., Stone J. M., 2008, Journal of Computational Physics, 227, 4123
- Gaskell W., Illingworth A., Latham J., Moore C., 1978, The Quarterly Journal of the Royal Meteorological Society, 104, 447
- Gibbard S. G., Levy E. H., Morfill G. E., 1997, Icarus, 130, 517
- Grach V., Semenov V., Trakhtengerts V., 2010, in 38th COSPAR Scientific Assembly Vol. 38, The flow of a dust particle by highly collisional drifting plasma. p. 1521

- Gurnett D. A., Kurth W. S., Hospodarsky G. B., Persoon A. M., Averkamp T. F., Cecconi B., Lecacheux A., Zarka P., Canu P., Cornilleau-Wehrlin N., 2005, Science, 307, 1255 1259
- Güttler C., Blum J., Zsom A., Ormel C. W., Dullemond C. P., 2010, Astronomy and Astrophysics, 513, 56
- Güttler C., Poppe T., Wasson J. T., Blum J., 2008, Icarus, 195, 504
- Hawley J. F., Gammie C. F., Balbus S. A., 1995, The Astrophysical Journal, 440, 742
- Hayashi C., 1981, Progress of Theoretical Physics Supplement, 70, 35
- Hayashi C., Nakazawa K., Nakagawa Y., 1985, IN: Protostars and planets II (A86-12626 03-90). Tucson, AZ, University of Arizona Press, 1985, p. 1100-1153., -1, 1100
- Helling C., 2011, Astrophysical Journal
- Helling C., Jardine M., Mokler F., 2011, Astrophysical Journal, 737
- Herczeg G. J., Hillenbrand L. A., 2008, ApJ, 681, 594
- Hernández J., Hartmann L., Calvet N., Jeffries R. D., Gutermuth R., Muzerolle J., Stauffer J., 2008, The Astrophysical Journal, 686, 1195
- Horanyi M., Morfill G., Goertz C. K., Levy E. H., 1995, Icarus, 114, 174
- Ilgner M., Nelson R. P., 2006, Astronomy and Astrophysics, 455, 731
- Inan U. S., Cohen M. B., Said R. K., Smith D. M., Lopez L. I., 2006, GEOPHYSICAL RESEARCH LETTERS, 33, L18802
- Inutsuka S., Sano T., 2005, The Astrophysical Journal Letters, 628, L155
- Johansen A., Oishi J. S., Low M.-M. M., Klahr H., Henning T., Youdin A., 2007, Nature, 448, 1022
- Jones D., Allen R., Basart J., Blume W., Dwarakanath K., Erickson W., Farrell W., Finley D., Gopalswamy N., Howard R., Kaiser M., Kassim N., Kuiper T., MacDowall R., Mahoney M., Perley R., Preston R., Reiner M., Rodriguez P., Stone R., Unwin S., Weiler K., Woan G., Woo R., 2000, Advances in Space Research, 26, 743
- Jones R. H., Danielson L. R., 1997, Meteoritics & Planetary Science, 32, 753 – 760
- Kalas P., Graham J. R., Chiang E., Fitzgerald M. P., Clampin M., Kite E. S., Stapelfeldt K., Marois C., Krist J., 2008, Science, 322, 1345
- Kato M. T., Fujimoto M., Ida S., 2010, The Astrophysical Journal, 714, 1155
- Kokubo E., Ida S., 1998, Icarus, 131, 171
- Koshak W., Krider E., 1989, Journal of Geophysical Research, 94, 1165

- Kudin K. N., Car R., 2008, Journal of the American Chemical Society, 130, 3915
- Kurth W. S., Gurnett D. A., Scarf F. L., Poynter R. L., 1984, Nature, 312, 27–31
- Lacki B. C., 2010, Monthly Notices of the Royal Astronomical Society, 406, 863
- Lagrange A., Gratadour D., Chauvin G., Fusco T., Ehrenreich D., Mouillet D., Rousset G., Rouan D., Allard F., Gendron É., Charton J., Mugnier L., Rabou P., Montri J., Lacombe F., 2009, A&A, 493, L21
- Lin Y. T., Uman M. A., Tiller J. A., Brantley R. D., Beasley W. H., Krider E. P., Weidman C. D., 1979, Journal of Geophysical Research, 84, 6307–6314
- Little B., Anger C. D., Ingersoll A. P., Vasavada A. R., Senske D. A., Breneman H. H., Borucki W. J., Team G. S., 1999, Icarus, 142, 306
- Lofgren G., 1989, Geochimica et Cosmochimica Acta, 53, 461–470
- Marois C., Macintosh B., Barman T., Zuckerman B., Song I., Patience J., Lafrenière D., Doyon R., 2008, Science, 322, 1348
- Mason B., Dash J., 2000, Journal of Geophysical Research, 105, 10185
- Miura H., Nakamoto T., Doi M., 2008, Icarus, 197, 269
- Muranushi T., 2010, Monthly Notices of the Royal Astronomical Society, 401, 2641
- Muranushi T., Okuzumi S., Inutsuka S.-i., 2012, The Astrophysical Journal, 760, 56
- Muranushi T., Tomiyasu T., 2009, in T. Usuda, M. Tamura, & M. Ishii ed., American Institute of Physics Conference Series Vol. 1158 of American Institute of Physics Conference Series, Proto-planetary Nebulae Struck by Lightning? A Charge Separation Study of Ice Dust Grains And its Effect on Dust Growth. pp 145–146
- Nomura H., Millar T. J., 2005, A&A, 438, 923
- Okuzumi S., 2009, The Astrophysical Journal, 698, 1122
- Ormel C. W., Cuzzi J. N., 2007, Astronomy and Astrophysics, 466, 413
- Pérez M. R., McCollum B., van den Ancker M. E., Joner M. D., 2008, A&A, 486, 533
- Pilipp W., Hartquist T. W., Morfill G. E., 1992, The Astrophysical Journal, 387, 364
- Rakov V. A., Uman M. A., 1998, IEEE Transactions on Electromagnetic Compatibility, 40, 403
- Roettgering H., 2003, New Astronomy Reviews, 47, 405
- Romanova M. M., Ustyugova G. V., Koldoba A. V., Lovelace R. V. E., 2012, Monthly Notices of the Royal Astronomical Society, 421, 63
- Roussel-Dupré R., Gurevich A. V., 1996, JGR, 101, 2297

- Rubin A. E., 2005, *Geochimica et cosmochimica acta*, 69, 4907–4918
- Ruf C., Renno N. O., Kok J. F., Bandelier E., Sander M. J., Gross S., Skjerve L., Cantor B., 2009, *Geophys. Res. Lett.*, 36, L13202
- Russell C. T., Zhang T. L., Delva M., Magnes W., Strangeway R. J., Wei H. Y., 2007, *Nature*, 450, 661–662
- Sano T., Inutsuka S., Miyama S. M., 1998, *The Astrophysical Journal Letters*, 506, L57
- Sano T., Miyama S. M., Umebayashi T., Nakano T., 2000, *The Astrophysical Journal*, 543, 486
- Shakura N. I., Sunyaev R. A., 1973, *Astronomy and Astrophysics*, 24, 337
- Shaw D. M., Higgins M. D., Hinton R. W., Truscott M. G., Middleton T. A., 1988, *American Mineralogist*, 73, 894
- Sirono S., 1999, *A&A*, 347, 720
- Sodha M. S., Misra S., Mishra S. K., 2009, *Physics of Plasmas*, 16, 123705
- Solomon R., Adamo C., Baker M., 2002, *Comptes Rendus Physique*, 3, 1325
- Sorathia K. A., Reynolds C. S., Stone J. M., Beckwith K., , 2011, Global Simulations of Accretion Disks I: Convergence and Comparisons with Local Models
- Spergel D. N., Kasdin J., Belikov R. e. a., 2009, in *Bulletin of the American Astronomical Society Vol. 41 of Bulletin of the American Astronomical Society, THEIA: Telescope for Habitable Exoplanets and Interstellar/Intergalactic Astronomy*. pp 362–+
- Spitzer L. J., 1941, *ApJ*, 93, 369
- Suyama T., Wada K., Tanaka H., 2008, *ApJ*, 684, 1310
- Suzuki T. K., Muto T., Inutsuka S., 2010, *The Astrophysical Journal*, 718, 1289
- Svedhem H., Titov D. V., Taylor F. W., Witasse O., 2007
- Takahashi M., 2005, *The journal of physical chemistry, B*, 109, 21858
- Takahashi T., 1978, *Journal of the Atmospheric Sciences*, 35, 1536
- Thalmann C., Carson J., Janson M., Goto M., Egner S., Feldt M., Hashimoto J., Hayano Y., Henning T., Hodapp K. W., Kandori R., Klahr H., Kudo T., Kusakabe N., Mordasini C., Morino J., Suto H., Suzuki R., Tamura M., 2009, *ApJL*, 707, L123
- Tokano T., Molina-Cuberos G. J., Lammer H., Stumptner W., 2001, *Planetary and Space Science*, 49, 539–560
- Tsuchiya H., Enoto T., Yamada S., Yuasa T., Kawaharada M., Kitaguchi T., Kokubun M., Kato H., Okano M., Nakamura S., Makishima K., 2007, *Physical Review Letters*, 99, 165002

- Umebayashi T., Nakano T., 1980, Publications of the Astronomical Society of Japan, 32, 405
- Umebayashi T., Nakano T., 2009, The Astrophysical Journal, 690, 69
- Wada K., Tanaka H., Suyama T., Kimura H., Yamamoto T., 2008, in Lunar and Planetary Institute Science Conference Abstracts Vol. 39 of Lunar and Planetary Institute Science Conference Abstracts, Numerical Simulation of Dust Aggregate Collisions: Compression and Disruption of BCCA Clusters. pp 1545–+
- Wada K., Tanaka H., Suyama T., Kimura H., Yamamoto T., 2008, The Astrophysical Journal, 677, 1296
- Wardle M., 2007, Astrophysics and Space Science, 311, 35
- Wardle M., Salmeron R., 2012, Monthly Notices of the Royal Astronomical Society, 422, 2737
- Wasilewski P., Dickinson T., 2000, Meteoritics and Planetary Science, 35, 537
- Weidenschilling S. J., 1997, in Lunar and Planetary Institute Science Conference Abstracts Vol. 28, Production of chondrules by lightning in the solar nebula? not so easy!. p. 1515
- Wettlaufer J. S., 2010, The Astrophysical Journal, 719, 540
- Williams E., 2001, Physics Today, 54, 41
- Wood M. D., 2011, Lightning: Properties, Formation and Types. Nova Science Pub Inc

Acknowledgement

I would like to thank my supervisor, Professor Shu-ichiro Inutsuka, for his great directions, fruitful discussions and endualing encouragement. I would like to do the same to Takayuki Muto, Satoshi Okuzumi and Yu-ichiro Sekiguchi as my senior researchers. I would also like to thank Tatsukya Tomiyasu for introducing me to the fascinating research field of lightning. I would also like to thank Hidekazu Tanaka, Tetsuo Yamamoto and their colleagues at Institute of Low Temperature Science, Hokkaido University for their kind invitation and discussion on the dust charge and aggregation. The authors thank Tsuyoshi Hamada, Keigo Nitadori and Evgenii Gaburov for their advice on GPGPU calculations. I would also like to thank Hitoshi Miura for the discussions on the chondrule formation. In addition to above, I would like to express my gratitude to all the efforts and attempts have been made in the field of computer science that made today's research environment possible.

I would also like to thank the members of Theoretical Astrophysics Group, lead by Professor Takashi Nakamura, at Kyoto University; the members of Yukawa Institute for Theoretical Physics; the members of Professor Masaru Shibata's group; and the members of The Hakubi Center for Advanced Research. I am grateful to all of my friends and post- and current roommates that helped me when I was in despair and beared with the noise I make. The last but not the least, I appreciate the untiring support by Yuko.